Functions of TRPM7 Chanzyme in Innate and Adaptive Immunity

Marta Ewa Stremska

M.S. Microbiology, Immunology and Cancer Biology, University of Virginia

M.S. Biotechnology, University of Warsaw

B.S. Genetics, University of Glasgow

A Dissertation presented to the Graduate Faculty of the University of Virginia in Candidacy for the

Degree of Doctor of Philosophy

Department of Microbiology, Immunology and Cancer Biology

University of Virginia

January 2022

Bimal N. Desai, Ph.D.

Sarah Ewald, Ph.D.

Kodi Ravichandran, Ph.D.

Young Hahn, Ph.D.

Irina Bochkis, Ph.D.

Abstract

Innate and adaptive immune cells orchestrate inflammatory responses in the host to protect against invading pathogens. Innate immune cells recognize pathogen-derived molecules to mount inflammation, sequester and kill microbes and present their antigens to T cells. Adaptive immune responses are precisely directed towards presented antigens and take time to develop upon the first encounter, however, the response time shortens during consecutive confrontations with the same invader. A specialized subtype of T cells, regulatory T cells (T_{regs}), suppress excessive inflammation and promote immune and tissue homeostasis. All immune cells integrate multiple signals upon ligand stimulation. Calcium (Ca^{2+}) serves important roles as a second messenger, drives cell activation and signaling pathways of pro-and anti-inflammatory programs. Recent studies have been defining electrical signaling as a key component immune cell function. TRP-superfamily of ion channels comprises a group of multifunctional proteins with many roles in sensory perception and cellular physiology. This work describes the roles of one highly conserved member, TRPM7, in innate and adaptive immunity. In macrophages, TRPM7-activated current is triggered upon recognition of a fungal particle and the chanzyme's activity is important in effective fungal phagocytosis. TPRM7-deficient T cells display a developmental block, overproduce IL-2 and display increased T_{reg}:T_{eff} ratio.

Acknowledgments

I was offered a remarkable opportunity to be a part of the University of Virginia and the Charlottesville community during my graduate career. I am very grateful to the exceptional faculty, students and staff for being a part of my experience and their participation in my career- and life- training that has shaped me into the person I am today.

I would like to thank Dr. Zygmunt Derewenda, Dr. Mark Okusa, and Dr. Rahul Sharma for admitting me into the Visiting Graduate Research Traineeship Program (VGRTP) at UVA. This program initiated my passion to pursue a career in academic research. Thank you for giving me this once-in-a-lifetime opportunity to train with you, attend multiple scientific conferences where I shared my work and learned from international scientists. Thank you, Rahul, you are the best mentor a junior trainee could have. Your patience, persistence and tireless stories about T_{regs} and the immune system sparked my interest in immunology. You, together with Dr. Okusa jumpstarted the discovery of my confidence as a young scientist. Your support and encouragement forever changed my professional life and prompted me to seek higher achievements and pursue a doctorate degree in immunology. To this day I am amazed how much I could achieve in just only two years of training with you.

I am undeniably grateful to my graduate advisor, Bimal N. Desai. I joined

your lab with little appreciation of the functions of ion channels, especially in immune cells. You opened my eyes to this fascinating field of research, encouraged me to pursue answers to complex biological phenomena and cultivated my personal development. I would like to express my appreciation for how you guided me scientifically throughout the years. Thank you, Bimal, for giving me multiple perspectives on how to deal with professional and personal challenges. I hope I can be as a well-rounded mentor for someone one day.

Thank you to my committee members, Drs. Sarah Ewald, Kodi Ravichandran, Young Hahn, and Irina Bochkis for your vast expertise in different scientific fields, pointed questions, and motivation you would supply at each meeting. You kept me sharp-minded with your critical comments and suggestions for improvement. I am beyond grateful for the time commitment you put into shaping me as a young professional.

To all the Desai lab members: your diverse scientific curiosity, laboratory skills, and ideas were formative in multiple ways. You made each day a challenge-tackling experience, and I am very proud I got to be a part of our team. Working alongside you, exchanging scientific opinions, but above all becoming good friends made hardships manageable. Thank you for your friendship, honest advice, critical comments and being great role models to our undergrads. Thank you, Mike, for your unmatchable kindness, patience, and professionalism. I look up to you every day and I strive to become as eloquent and thorough as you are. Thank you,

Catherine, for being the best lab-bay mate, for our endless elbow-to-elbow daily operations and inviting me to all your hiking adventures. You would always brighten up my days with a simple chat. Thank you, Phil, for our numerous late nights in the lab and giving me lots of helpful pointers with the candida project. Thanks for always saving a spot for me at your “Friendsgiving” and making me a part of your “boys-night-out”. Thank you, Greg, for your inspiring and honest interest in everything, you truly make the world more fascinating every time I talk to you. Thank you, Eric, for all your technical advice and daily history lessons. Thank you, Suresh, for allowing me to be a part of your study and giving me my first real electrophysiology training. I owe my first and only good electrophysiological seal to you. Thank you, Joel, for all your help with the animal work and late night conversations about our favourite authors. A big thank you to all the talented undergraduate students who I have had the pleasure to mentor: Angie, Joey, and Jess. Your incessant and persistent questions and your pursuit of understanding provided me with a sense of belonging to science. I never thought I would have to define the word “aliquot”. I am extremely proud hearing about your achievements in your current professions and I hope you will never stop doing your best to “be better”.

And to all undergraduate students, I was not directly mentoring, but had the pleasure of interacting with: Logan, Rachel, Priya, Wes, Sardul and Hansa. Thank you for contributing to the overall comradery and the atmosphere in our lab.

Charlottesville has been a wonderful place to live in during my graduate career. The sense of community is omnipresent, either at the University, or outside, in sport and other friend circles. Thank you to all my wonderful roommates and friends throughout the years who pressed me into taking much-needed study breaks, for all the get-togethers during holidays and the weekends, and for all the dinner parties without a special occasion. You made Charlottesville a home away from home and what a home it was! Thank you to my dear volleyball friends for making me a part of the multiple teams either in all women or co-rec leagues.

Last, but certainly most importantly, a big thank you to my family. “Thank you” does not do justice to how grateful I am to have had the best role models who incessantly have been molding me into a curious individual. Because of your hard work and multiple investments, I could pursue multiple academic opportunities. First, to study in Glasgow and California and then in Virginia. I now realize how hard it must have been for you to “send me away” onto my own life’s journey.

I would like to thank my maternal grandparents Krystyna and Jan, who taught me that being an A-student is important but excelling at and having a passion towards your chosen career path even more so. Thank you for your immense support in my decisions despite often having a dissimilar opinion. My paternal grandparents: Irena and Józef, whom I only got a chance to meet when I was very young, but who I remember as warm and encouraging. My dearest parents: Ewa and Jerzy: I now understand the sacrifices you made, for me to grow

into the person I still seek to become. You instilled in me life's most important values and taught me to be independent and follow my ambition. However, the time I spent doing just that was the time I spent far away from you. Nonetheless, you would always find means to express your constant support. You always were a united front when it came to my well-being, the source of wisdom and the comfort I know. A big thank you to my little brother, Marek, whose life path geographically coincided with mine. Even though I may have not expressed it, and at times even deny it, I appreciated having you as my roommate. You were my only family I had close by, which undeniably provided me with a sense of security. Thanks for being there for me and tackling small, but omnipresent daily challenges.

I have been extremely fortunate to be surrounded with such immense support throughout my development so far and I hope I can pay it forward.

"You cannot hope to build a better world without improving the individuals. To that end each of us must work for his own improvement, and at the same time share a general responsibility for all humanity, our particular duty being to aid those to whom we think we can be most useful."

Maria Skłodowska-Curie

Table of Contents

List of Figures

List of Tables

List of Abbreviations

AIH- Autoimmune hepatitis

ALT- Alanine transaminase

ATP- Adenosine triphosphate

BMDM- Bone marrow derived macrophages

BMT- Bone marrow transplantation

Ca^{2+} - Calcium

CBC- Complete blood count

CFSE- Carboxyfluorescein succinimidyl ester

CFU- Colony forming unit

CLR- C-type lectin receptors

Con A- Concanavalin A

CPA- Cyclopiazonic acid

CRAC- Ca^{2+} release- activated calcium channels

DAG- Diacylglycerol

DAMP- Danger associated molecular pattern

DC- Dendritic Cell

ELISA- enzyme- linked immunosorbent assay

ER- Endoplasmic reticulum

ETC- engulfment-triggered current

FMO- Fluorescence minus one

Foxp3- Forkhead box 3

G-CSF- Granulocyte colony- stimulating factor

GPCR- G-protein coupled receptor

H&E- Hematoxylin and eosin

IL- Interleukin

IP_3- Inositol triphosphate

IP_3R- Inositol triphosphate receptor

ITAM- Immunoreceptor tyrosine-based activation motif

KO- knockout

LDH- Lactate dehydrogenase

LOF- Loss-of-function

LPS- Lipopolysaccharide

MFI- Mean fluorescence intensity

NFAT- Nuclear factor of activated T cells

NFκB- Nuclear factor kappa-light chain enhancer of activated B cells

NK cell- Natural killer cells

NLR- NOD-like receptors

PAMP- Pathogen associated molecular pattern

PAS- Periodic acid- Schiff

PIP_2 -Phosphatidylinositol-4,5-bisphosphate

PLCγ- Phospholipase Cγ

PPCE- Perforated patch- clamp electrophysiology

PRR- Pattern recognition receptor

RLR- RIG-I-like receptors

qRT-PCR- Quantitative reverse transcriptase polymerase chain reaction

S1PR1- Sphingosine 1-phosphate receptor 1

SEM- Scanning electron microscopy

SERCA- Sarcoplasmic reticulum Ca^{2+}-ATPase

SK2- Sphingosine Kinase 2

SOCE- Store- operated calcium entry

STAT5- Signal transducer and activator of transcription 5

STIM1- Stromal interaction molecule 1

TCR- T cell receptor

TEM- Transmission electron microscopy

T_{eff}- Effector T cells

TG- Thapsigargin

TGF-β – Transforming growth factor β

TLR- Toll-like receptors

T_{reg}- Regulatory T cells

TRPM7- Transient Receptor Potential Melastatin-7

UV- Ultraviolet

WC-PCE- Whole-cell patch-clamp electrophysiology

WT- wild type

CHAPTER ONE: Ion channels in immune cells functions

Immune system synopsis

The main evolutionary function of the immune system is to protect the host from infection. To do so efficiently, the immune system developed hierarchical coordination, in which there are the immune cells at the front line, so-called “first responders” followed by a set of more specialized effectors, which mount a defense against a specific antigen. Bone marrow is where hematopoietic stem cells give rise to two immune cell lineages: myeloid and lymphoid. Myeloid cell progenitors develop into innate immune cells, like macrophages and neutrophils, amongst others, while the lymphoid lineage gives rise to the precursors of the adaptive branch of immunity, that include T cells, B cells and NK cells. Innate immunity protects the organism against pathogens (bacteria, viruses, fungi and parasites) with a set of non-variable receptors each time they invade and try to hijack the cellular resources for their own survival. Phagocytes, including macrophages, neutrophils and dendritic cells are equipped with a set of germline-encoded receptors, referred to as pattern recognition receptors (PRRs). They can recognize the danger-associated molecular patterns (DAMPs) that are endogenous cell-derived molecules released from a damaged cell or pathogen-associated molecular patterns (PAMPs) that are highly conserved, often structural

molecules characteristic of microbial biology. In vertebrates, the ability of innate cells to process and present antigens is essential to stimulate the adaptive immune response. T cells recognize the instructions provided by antigen-presenting cells and give rise to targeted and specific immune responses that are long-lasting. Immune cells regulate pro- and anti-inflammatory responses in tight-knit programs of checks and balances to most effectively target the pathogen while restricting tissue damage. A specialized subset of T cells, regulatory T cells (T_{regs}), limit excessive inflammation, promote tissue homeostasis and self-tolerance. Loss-of-function (LOF) mutations in their defining transcription factor Foxp3 lead to T_{reg}-deficiency and results in devastating autoimmune disease called immune dysregulation, polyendocrinopathy, enteropathy, X-linked (IPEX) syndrome in humans (*scurfy* in mice), for which the most effective treatment remains transplantation of the hematopoietic stem cells (HSCs)[1]. In addition to immune cells, epithelial and endothelial cells can recognize DAMPs and PAMPs, and therefore contribute to local, inflammatory responses[2–4]. Although their role in inflammation is appreciated, this dissertation focuses on the roles of professional phagocytes as the main orchestrators of inflammatory responses.

All hematopoietic cells express a number of ion channels, which regulate their membrane potential and a variety of cellular functions, ranging from differentiation and activation to gene expression and even cell death. Here, I will review the most important roles of ion channels in immunity, led by

pharmacological and genetic evidence.

Introduction to ion channels

Ions cannot freely pass through the amphipathic lipid membranes. As a result, the movement of ions across the plasma membrane is regulated by ion channels, ion exchangers, and pumps. Cells tightly control ionic flux and devote an enormous amount of cellular energy to regulate the activity of ion pumps. The directionality of ion flux through an ion channel is determined by the pump's electrochemical gradients and the cell's membrane potential (V_m). Conversely, pumps and exchangers can move ions against their electrochemical gradients by using energy from the counter-conducting ions or ATP hydrolysis[5]. Cells harvest the ionic gradients as a resource in many cellular signaling events, for example, activation of signaling cascades, cell-volume regulation, pH balance, motility, and protein secretion. The schematic summary of ion channels expressed in macrophages and T cells is depicted in Figure 1. Ion channels establishing the V_m are predominantly those that regulate monovalent fluxes of K^+, Cl^- and Na^+. Under physiological conditions, the relative concentrations of ions across the biological membrane favor K^+ efflux and the influx of Na^+ and Cl^-. Divalent cations, like Ca^{2+}, Mg^{2+} or Zn^{2+} mostly exist in protein-bound states inside the cell and are actively pumped out. Hence the "free" concentrations of divalent cations are in nM scale,

which generates a steep concentration gradient of about 20,000 to 45,000-fold difference[6], depending on the ion. Divalent cations are often involved in signaling cascades resulting in effector protein activation, therefore they are often referred to as second messengers.

Two main properties of ion channels: ion selectivity and gating, distinguish them from simple aqueous pores. Selectivity, which can be astonishingly precise, differentiates between ions of similar size or charge. This is achieved through the differences in the stereochemistry of the channel pore, its *selectivity filter*, and lining the "ion passageway" with atomic binding sites that favor the interaction of one ion versus another. Most ions in the aqueous solution are hydrated and dehydration is energetically costly. Selectivity arises when a dehydrated ion is coordinated with the charged residues in the channel pore to overcome the energetic cost of dehydration[5]. Orai1 is an example of a highly selective, low conductance Ca^{2+} channel, permeating Ca^{2+} ions a 1,000-fold better than Na^{+} [7]. On the contrary, TRPM7 channel is cation conducting but non-selective; it is permeable to Ca^{2+}, Mg^{2+} and Zn^{2+}, Na^{+} and K^{+}. The fractional component of the overall TRPM7 currents depends on the ionic environment but in physiological conditions, it should favor the conductance of Ca^{2+}, Na^{+} and Zn^{2+} over other cations with comparatively modest concentration gradients. Cellular membrane composition of ion channels in physiological conditions, creates a sophisticated interplay between their activities. For example, opening of a Ca^{2+} conducting

channel locally depolarizes the membrane and in turn activates the K^+ efflux from K_v and K_{Ca} channels, which promotes the restoration of membrane potential[8].

Ion channel opening or “gating” is often regulated by a specific stimulus. There are several recognized gating mechanisms; these include changes in voltage (voltage- gated), mechanical stress (mechanically gated), increase in other ion concentration (ion- gated), nucleotides (nucleotide-gated), or neurotransmitters (transmitter- gated). Moreover, the gating thresholds of ion channels can also be modulated by post-translational modifications[9,10].

General routes for signaling in immune cells

Immune cells express several calcium-conducting ion channels that regulate their effector functions. There are two ways through which lymphocytes can increase their Ca^{2+} concentrations: (1) release of Ca^{2+} from intracellular Ca^{2+} stores, mainly the ER, and (2) opening of Ca^{2+}-conducting ion channels on the plasma membrane. Crosslinking of antigen receptors, activation of G_q-protein coupled receptors (G_qPCRs) or signaling through immunoreceptor tyrosine-based activation motifs (ITAMs), that recruit spleen tyrosine kinases (Syk), result in activation of phospholipase C (PLC). Activated PLCs hydrolyze phosphatidylinositol 4,5-bispohosphate (PIP_2), a phospholipid residing in the plasma membrane, releasing inositol triphosphate (IP_3) and diacylglycerol (DAG).

Dissociated IP_3 binds to its cognate large-conductance receptor (IP_3R) and releases Ca^{2+} from the ER to the cytoplasm. IP_3Rs, encoded by *Iptr1-3*, are large, tetrameric ligand-gated, non-selective channels, residing in the ER membrane and at least one of the isoforms is expressed in each cell type. Ryanodine receptors (*RyR*) also conduct Ca^{2+} out of the ER and are activated by high cytoplasmic Ca^{2+} concentrations (in μm scale), hence often act as signal amplifiers[11]. The function of RyR in immune cells is poorly defined so far, but their expression was reported in lymphocytes, mainly $CD19^+$ and $CD3^+$ cells[12,13] (B and T cells, respectively). Mutations in genes coding ion channels have been linked to immunodeficiencies and susceptibility to infection, collectively termed “channelopathies”, comprehensively reviewed here[14]. A number of immune cellular processes are contingent on IP_3-dependent Ca^{2+} release. Activation of antigen receptors, as mentioned earlier, happens similarly in T cell, B cells or mast cells and results in phosphorylation of the immunoreceptor tyrosine ITAMs that recruit Syk kinases[15]. The rapid cytosolic Ca^{2+} increase is crucial for membrane and cytoskeletal rearrangements, cellular motility, immunological synapse formation and activation of Ca^{2+}-dependent transcription factors[15,16]. The ER-resident stromal molecule 1 and 2 (STIM1 and STIM2), equipped with Ca^{2+}-binding EF-hand motifs detect the Ca^{2+} decrease and oligomerize. This conformational change allows STIM oligomers to bind to and open the highly Ca^{2+}-selective Orai channels on the plasma membrane, resulting in store-operated Ca^{2+} entry (SOCE). Purinergic

receptors also contribute to cellular Ca^{2+} signaling and are divided into P1 (adenosine) and P2 (nucleotide) receptors. Further, P2 comprise of two subgroups: P2Y (GPCRs) and P2X (ionotropic) receptors and subgroups have reported expression in immune cells[14,17]. Elevations in cytosolic Ca^{2+} levels are then rapidly sequestered into organelles, mainly into ER through SERCA pumps and into mitochondria via mitochondrial Ca^{2+} uniporter (MCU) channels. TRPML (1-3), also known as mucolipins, are lysosome-resident non-selective channels, belonging to the TRP family of proteins. They conduct Ca^{2+} and monovalent cations from the lysosomal lumen into the cytoplasm and are key in modulation of secretory lysosomes and granzyme B secretion. TRPML1 loss of function causes a rare lysosomal storage disorder, mucolipidosis IV, characterized by severe neurodegeneration and premature death[18]. The activity of TRPML1 is also appreciated in autophagy, wherein localized TRPML1-dependent Ca^{2+} signals from the lysosome activate TFEB transcription factor to increase transcription of genes involved in lysosomal biogenesis and autophagy[19]. Lastly, Zn^{2+} transporters (ZnTs) and Zrt/Irt-like proteins (ZIP1-14) are a ubiquitous family of proteins that regulate the influx of Zn^{2+}. Deficiency of Zn^{2+} presents in patients as susceptibility to variety of pathogens and it is a known co-factor for the functioning of many enzymes in signaling pathways[20].

Recent advances in generating gene-targeted mice and performing whole-genome sequencing in patients underscored the importance of several ion channels in lymphocyte development and immune responses.

TRP Channels and TRPM7

Transient Receptor Potential channels are a large family of highly conserved channels with diverse activation mechanisms. They owe their family name to the TRP channel in *Drosophila melanogaster* eye. The TRP channel in the fly eye exhibits phototransductory properties. Electro-retinogram studies showed that inactivating mutations of *Trp* result in a transient voltage response to continuous light exposure, instead of the sustained voltage response of the wild type eye[21,22].

There are seven TRP subfamilies: TRPC (canonical), TRPV (vallinoid), TRPM (melastin), TRPN (no-mechano-potential C; NOMPC-like), TRPA (ankyrin), TRPP (polycystic), TRPML (mucolipin), however, TRPN channels have only been found in invertebrates and zebrafish[22]. All members encode a monomer with six membrane-spanning helices (S1-6), in which both termini are located in the cytoplasm. The functional channel pore requires an assembly of four subunits with pore forming loop between S5 and S6. Intriguingly, generation of functional heteroterameric TRP channels have been reported[23–25] using concatenated

constructs, raising fascinating prospects about the number of possible discrete channel outcomes. The ligands activating TRP channels are only partially known. G- protein coupled receptors ($G_{q/11}$) or tyrosine kinase receptors both converge on PLC signaling that can potentiate the activity of TRP channels. Moreover, PIP_2 signaling and intracellular Ca^{2+} modulate the activity of TRP channels. TRP channels, except TRPM4 and TRPM5, are permeable to Ca^{2+} [26]. A few TRP channels contain C'-terminal domains with enzymatic activities. TRPM2 expresses a Nudix hydrolase 9 (NUDT9) homology domain with a presumed ADP-ribose pyrophosphatase activity. The domain shares ~45% sequence similarity to the mitochondrial pyrophosphatase, which catalyzes the hydrolysis of adenosine 5'-diphosphoribose (ADPR) to adenosine monophosphate (AMP) and ribose-5-phosphate (R5P). However, TRPM2's true catalytic activity has been recently challenged in the *in vitro* ADPRase assays, and the "broken enzymatic activity" was proposed to be a mechanism for increased ligand binding at low ADPR concentrations[27]. Both, TRPM6 and its closest homolog TRPM7, contain a functional atypical α-kinase domain[22]. When expressed ectopically, both channels exhibit similar properties, however, they are not redundant[28]. Both have been implicated in Mg^{2+} homeostasis, given that mutations in *trpm6* loci in humans are linked to an autosomal recessive form of familial hypomagnesemia with secondary hypocalemia[29,30]. TRPM6 is predominantly expressed in the kidney and gastrointestinal tract, while TRPM7 shows ubiquitous but variable levels of

expression.

TRPM (melastatin) subfamily was named after TRPM1, the first identified representative, which in 1998 was shown to be significantly downregulated in murine melanoma cell line[31]. Since then, seven other members, sharing structural features were recognized (TRPM1-8). Immune cells however show appreciable expression of only TRPM2, TRPM4 and TRPM7. TRPM4 is a cation monovalent channel, which due to its Na^+ permeability depolarizes the plasma membrane. It is activated by Ca^{2+}, following receptor stimulation and rapid increase in cytosolic Ca^{2+}, and limits the magnitude of Ca^{2+} influx by depolarizing the membrane, contributing to the characteristic oscillatory patterns of Ca^{2+} transients[6].

TRPM7 (Fig. 2) expression is the most ubiquitous amongst the TRP channel family[32]. TRPM7 global knockout (KO) mice do not survive past day 7 of embryogenesis indicating that the channel is critical for early embryonic development [33]. The channel was identified in 2001 by three, independent groups using diverse approaches [34–36]. Clapham group used the C2-domain of PLC-β_1 as a bait and identified C'-terminal TRPM7 kinase as its interaction partner[34]. The Ryazanov lab[36] performed a homologue screen for eukaryotic elongation factor (eEF-2) kinase 2. The Fleig group's study involved bioinformatic approaches aiming to identify ion channels expressed in immune cells[35]. TRPM7 currents are described as characteristic outwardly rectifying current that is non-selective and permeant to Ca^{2+}, Zn^{2+}, Mg^{2+}, and Na^+.

Early reports suggested that the kinase domain also modulates the channel conductance[34,35], but this idea was later contested in a series of electrophysiological recordings with the kinase activity-dead mutants[37,38]. However, TRPM7 currents are increased when the kinase domain is freed from the channel by proteolytic cleavage at D1510[39]. The serine-threonine kinase domain of TRPM7 belongs to an atypical α-kinase family, whose catalytic subunit displays no sequence homology with any known conventional protein kinase[40]. TRPM7 kinase has been shown to interact *in vitro* with PLCγ2 and phosphorylate annexin A1 (ANXA1)[41], myosin IIA[42], transcription factors, chromatin remodelers (RYBP, YY1, Ino80, Ezh2, and RNF2), and histones[43]. It crystallizes as a dimer and it can undergo auto-phosphorylation, predominantly on serine (Ser) residues[40,44]. Recent studies have suggested that the kinase binds to nuclear factors in a Zn^{2+}-dependent manner (coincidentally, TRPM7 channel demonstrates highest selectivity for Zn^{2+} ions).

TRPM7 channel, whose single channel conductance is ~40 pS, was reported to be activated by low pH[45], regulated by changes in the membrane PIP_2 levels[46] and inhibited by intracellular Mg^{2+} and Mg^{2+}-ATP[35]. Its electrical activity in immune cells was shown to be crucial in the process of proper thymopoiesis[33] and effective innate immune responses[47–49]. Modulation of calcium signals appears to be at the forefront of defects exhibited by the TRPM7-deficient cells.

In thymocytes, biphasic rise in cytosolic Ca^{2+} differentially modulates the activities of NFκB and NFAT transcription factors[50], which play a vital role in pre-TCR T lymphocytes development. Activation, differentiation, and T cell motility all require Ca^{2+} SOCE responses. In innate immunity, Ca^{2+} dynamics orchestrates motility, effective phagocytosis, endocytosis and proper activation of signaling molecules[47]. Considering the panoply of Ca^{2+}-conducting proteins and the constant interplay of Ca^{2+}-signals received by the cell, the overall role of Ca^{2+} in cell signaling is very complex. But ion channels have a way of imposing selectivity on signal transduction pathways because Ca^{2+} signals can be spatially localized and temporally synchronized with other processes. Deciphering the underlying Ca^{2+}-code can help us unravel the complex switchboard of electrical signals that regulate immune functions and pinpoint key ion channels as drug targets for highly specific immunomodulation. Toward that goal, we aimed to understand the immunological phenotypes resulting from genetic and pharmacological targeting of TRPM7.

In this dissertation, first I will describe the contributions of TRPM7 channel in the phagocytosis of yeast species by macrophages. A process in which the contributions of SOCE Ca^{2+} responses have been widely acknowledged and the contributions of other Ca^{2+}-conducting channels overlooked. I show that mice with a conditional *Trpm7* deletion in their myeloid cells (*Trpm7*$^{fl/fl}$ *LysM-Cre*) display increased susceptibility to lethal candidiasis including lower survival, higher

pathogen burden especially in the kidneys and slightly higher inflammation. *In vitro* challenge with yeast reveals a striking engulfment defect, stemming from a reduction of sustained Ca^{2+} flux and aberrant cytoskeletal architecture.

In the second part of my thesis, I focus on the TRPM7 function in adaptive immunity. Elaborating on the striking observation that targeting *Trpm7* in murine T cells leads to their protection in a T-cell driven immune hepatitis model. Inhibiting of TRPM7 activity, either through genetic deletion or pharmacologically, leads to over-production of IL-2 in T cells and promotes the thymic output of regulatory T cells (Tregs). Finally, in the last chapter I discuss the outstanding questions that arise from these studies and offer ideas and approaches to address them in the future.

CHAPTER ONE FIGURES

Figure 1

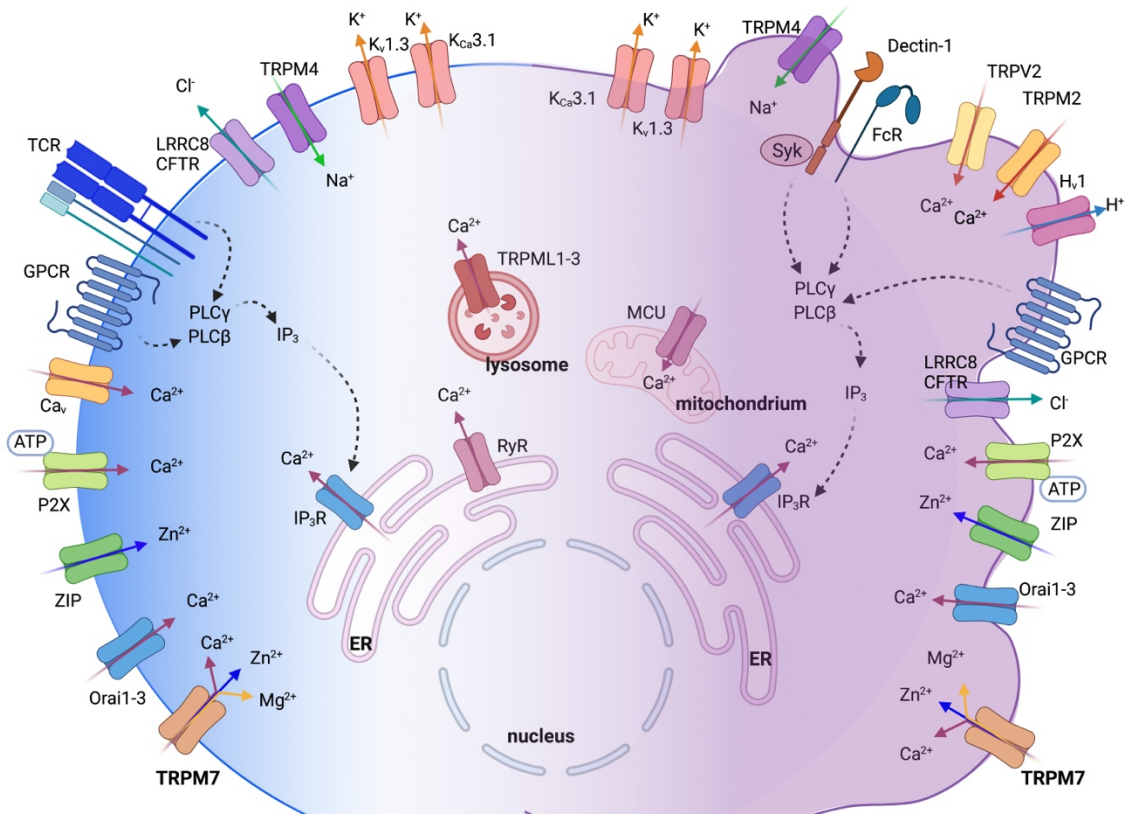

T cell

Macrophage

Figure 1. Comparison of main ion channels expressed in T cells and macrophages

Immune cells (*right:* T cells, *left*: macrophages) express a variety of ion channels on their plasma membrane, as well as intracellularly. Note that not all channels expressed by T cells and macrophages are presented here. Ion channels important in controlling the membrane potential, important for SOCE are mainly: K^+ conducting channels: K_V, K_{Ca}, Cl^- channels: LRRC8, CFTR and Na^+ channels, exemplified here by TRPM4. The main route of SOCE activation in T cells is through crosslinking of the antigen receptors (TCR) or ligand binding to its cognate G_q-coupled GPCR. In macrophages, analogously, GPCR activation, as well as stimulation of receptors with ITAM-like domains (Dectin-1 or FcRs) lead to SOCE. Several Zn^{2+} transporters (ZIPs) mediate Zn^{2+} influx, which is important in activation several transcription factors (such as TFs containing zinc finger domain), and reportedly regulate Zn^{2+} influx upon TLR stimulation in macrophages. Nucleotides (ATP) are ligands for purinergic channels (P2X), which lead to Ca^{2+} influx. H_v1 channel associates with NADPH complex (not shown) and is important in reactive oxygen species (ROS) generation. TRPV2, TRPM2 and TRPM7 conduct Ca^{2+} and the latter was also shown to be important in Mg^{2+} and Zn^{2+} fluxes.

Figure 2

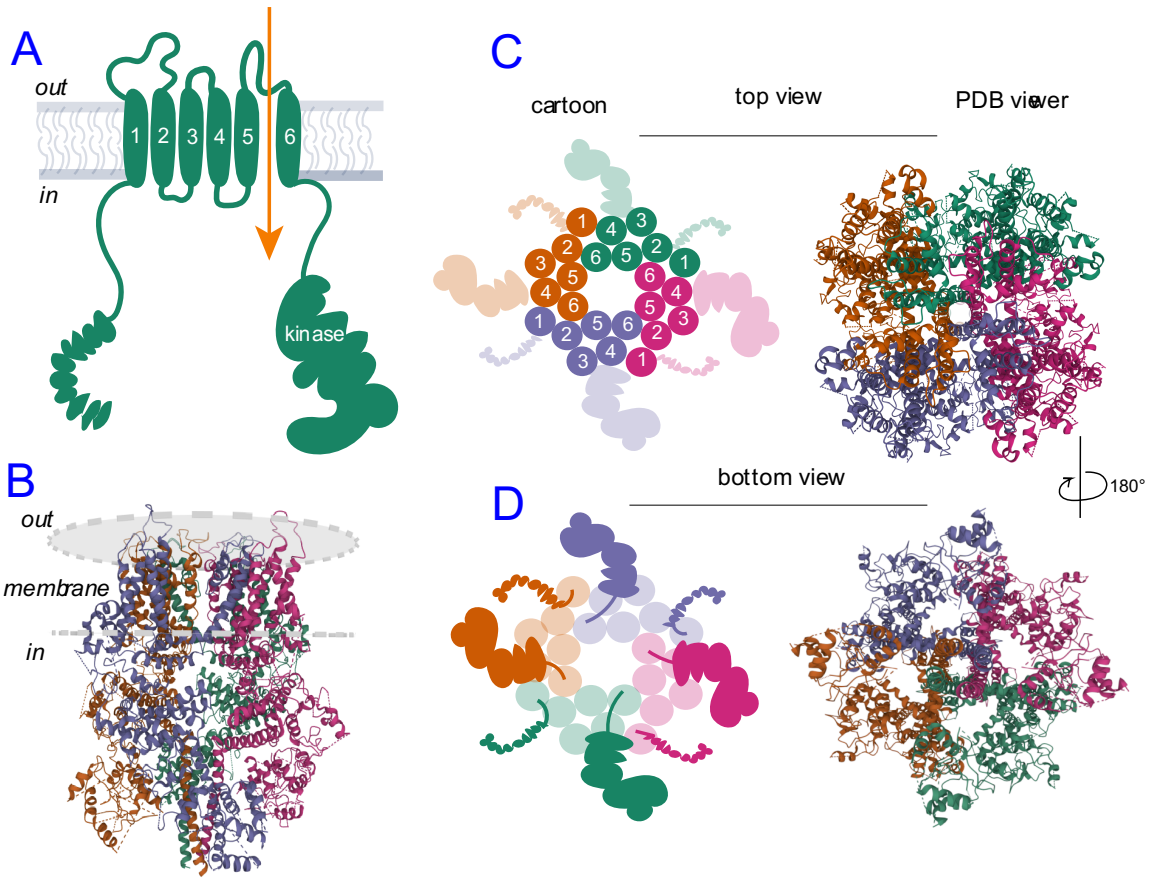
A
out
1
2
3
4
5
6
in
kinase
B
out
membrane
in
C
cartoon
top view
PDB viewer
D
bottom view
180°

Figure 2. TRPM7 cartoon and 3D structure

A) Cartoon of a TRPM7 monomer with transmembrane domains numbered and visualized intracellular termini: N'- and C'- terminal kinase domain.

B) 3D-view of a membrane embedded TRPM7 tetramer, adapted PDB: 6BWF. 4.1Å of Mg^{2+} -unbound mouse TRPM7 channel.

C) Top view of the cartoon and a 3D structure of TRPM7 mouse channel (PDB: 6BWF). Transmembrane domains are outlined in the cartoon.

D) Bottom view of the cartoon and a 3D PDB structure of mouse TRPM7 (PDB: 6BWF). Note that the bottom view is a 180° rotation of the top view from Figure 2C.

CHAPTER TWO: TRPM7-dependent electrical signals drive phagocytic clearance for effective anti-fungal defense

Disclaimer: The contents of Chapter Two appear as submitted for publication: Stremska, M. E., Stipes, E. J., Jang, J. J., Busey, G., W., Iobst, W., H., Seegren, P., V., Kennedy, J., Desai, B. N., TRPM7- dependent electrical signals drive phagocytic clearance for effective anti- fungal defense

Abstract

The rise of drug-resistant fungal strains has renewed the interest in deciphering the signaling pathways driving pathogen clearance to identify new molecular targets for immunomodulation. Macrophages are the sentinel phagocytes critical for the efficient clearance of fungal pathogens. Although we have a good understanding of the cell surface receptors used for detecting fungi, the molecular machinery that controls their phagocytosis remains undefined. Here, we show that the ion channel TRPM7 is essential for effective host defense against *C. albicans*. When *Trpm7* is deleted selectively in myeloid cells, the mice are highly susceptible to lethal candidiasis and *Trpm7-/-* macrophages display significant deficiencies in the engulfment of *C. albicans*. Through perforated patch clamp recordings of phagocytes engulfing zymosan particles, we show that a TRPM7-dependent outwardly rectifying current is activated during the initial stages of internalization. Deletion of TRPM7 also affects the Ca^{2+} signals and cytoskeletal changes that occur during phagocytosis. Consequently, *Trpm7-/-* macrophages display a lag in the formation and sealing of the phagocytic cup. These findings herald the first glimpses of a novel electrical signaling machinery initiated when macrophages detect fungal pathogens and raise the prospects of targeting TRPM7 for anti-fungal immunomodulation.

Introduction

Candida albicans (*C. albicans*) is a commensal microbe, which lines the epithelial mucosal surfaces. Under certain pathophysiological conditions, and in immunocompromised patients, *C. albicans* can become invasive, disseminate into the bloodstream, colonize vital organs and result in ~50% mortality rate[51]. Moreover, evolution of drug-resistant strains[52] demands the development of new pharmacological strategies that target the microbe or immunomodulate an effective host defense. Molecular understanding of the signaling pathways during anti-fungal response can yield novel pharmacologically tractable targets for such immunomodulation. Myeloid phagocytes like macrophages and neutrophils drive the anti-fungal immunity but the molecular machinery controlling fungal clearance is not fully defined[53,54]. Identifying new druggable components in this machinery has the potential to advance the next generation of anti-fungal immunomodulatory drugs.

Clustering of the phagocytic receptors recognizing certain chemical motifs of the fungal cell wall initiates fungal phagocytosis[55,56]. Engagement of Dectin-1, a receptor for β-glucan, recruits tyrosine kinases Src and Syk, that in turn activate phospholipase Cγ (PLCγ)[16,57,58]. PLCγ hydrolyses phosphatidylinositol 4,5-bisphosphate (PIP_2) to generate inositol triphosphate (IP_3) and diacylglycerol

(DAG). IP_3 binds to the ER-resident, large-conductance cation channel IP_3 receptor (IP_3R) and evokes potent calcium (Ca^{2+}) release from the intracellular stores. During engulfment, Ca^{2+} signals play a crucial role in mediating the rapid membrane and cytoskeletal rearrangements necessary for the extension and fusion of engulfing pseudopods[17,59]. The prevailing signaling framework is centered on the role of internal Ca^{2+}-stores in phagocytosis but the ion channel mechanisms that orchestrate the local spatiotemporal electrical signals at the phagocytic cup are not well-defined. Understanding these specialized molecular components and mechanisms may lead to novel immunomodulatory strategies for tissue-selective or systemic anti-fungal immune responses. Here, we reveal the critical role of the ion channel TRPM7 in the host defense against *C. albicans*.

TRPM7, a member of the Transient Receptor Potential (TRP) channel superfamily, is a cation selective ion channel that also possesses a serine-threonine kinase domain that is known to regulate actomyosin contractility[42,60]. It is expressed at high levels in immune cells and has emerged as a major regulator of the innate and adaptive immune functions[61–65]. Previously TRPM7 activity was shown to be regulated by inflammatory signals: caspase activation[66], low extracellular pH[45] or phospholipase C- coupled receptors[46].

Here, we show that when TRPM7 is deleted in myeloid cells, the mice are highly susceptible to lethal candidemia – they fail to effectively clear the pathogen from their kidneys and display heightened systemic inflammation. The bone-marrow derived macrophages (BMDM) acquired from these mice exhibit defective phagocytosis. Using perforated patch clamp recordings of macrophages engulfing *C. albicans* in real time, we show that TRPM7 activates an outwardly rectifying current at early stages of engulfment. The deletion of *Trpm7* disrupts the cytoskeletal dynamics that guide the timely formation and sealing of the phagocytic cup.

Results

Deletion of Trpm7 in myeloid cells increases the lethality of candida infection in mice

To model systemic candidiasis, we intravenously (i.v.) injected 1 x10^6 *C. albicans* into mice and monitored survival and disease severity over 96h at regular intervals[67,68]. Kaplan-Meier survival curve analysis showed that mice lacking TRPM7 in myeloid cells (*TRPM7*$^{fl/fl}$ *LysM-Cre* [KO]) displayed significantly increased susceptibility to systemic *C. albicans* infection when compared to TRPM7$^{fl/fl}$ (wild type [WT]) counterparts (n=10, p=0.0081) with a median survival time of 73h (Fig. 3A). Since the KO mice succumbed to the disease outcomes

much earlier, we performed a shorter *in vivo* candidiasis experiment, recorded each animal's weight throughout and at 48h, collected the kidneys, livers and sera. Starting at 24h post-infection, the KO mice displayed considerably higher weight loss (Fig. 3B, n=5) which, at 48h, averaged to ~15% loss of the initial body weight, compared to ~8% in the WT mice. To assess the colonization of *C. albicans* we used periodic acid-Schiff (PAS) staining method on the kidney and liver sections. PAS detects and binds fungal polysaccharides, which appear distinctively magenta stained (Fig. 3C, yellow arrows). We observed larger yeast colonies forming throughout the renal cortex and outer medullary regions, especially within or in the vicinity of the glomeruli, with small proportion colonizing the regions of the inner medulla. The quantification of *C. albicans* affected areas within the kidneys revealed increased *C. albicans* burden in the KO mice (Fig. 3C, 3D), while some of the WT mice kidney sections harbored only a few detectable *C. albicans* colonies. The other kidney and a part of liver from each animal was used to obtain crude tissue homogenates, which were then serially diluted and plated on YPD-agar containing petri dishes. We retrieved *C. albicans* colony forming units (CFUs) counts per gram of tissue. While not statistically significant, KO animals showed a trend toward a higher pathogen load in the kidneys (Fig. 4A) but the livers were affected to the same degree in both genotypes (Fig. 4B). To closely reexamine the higher colonization of *C. albicans* in the kidneys of KO mice, we performed immunohistochemical staining for CD45 and Ly-6G cell markers and quantified the

number of infiltrating hematopoietic cells and neutrophils, respectively. Chromogenically stained kidney sections (Fig. 3E and 4C) clearly outlined immune cells, which were mostly found within the renal cortex. Although, slightly elevated in the KO mice, overall, there was no significant difference in the number of $CD45^+$ infiltrates (Fig. 4D), which also indicated that KO animals are not defective in the recruitment of immune cells. Conversely, we found there were significantly more Ly-$6G^+$ cells, representing a higher number of infiltrating neutrophils in the kidneys of KO animals (Fig. 3F). To account for higher neutrophilic infiltration into the kidneys, we performed Luminex assay on the serum cytokines. We detected higher systemic inflammation in the KO mice with the difference especially pronounced for some inflammatory mediators (G-CSF, IL-6 and CXCL1). Other cytokines showed an insignificant difference (Fig. 3G). G-CSF (granulocyte colony stimulating factor) is a glycoprotein that stimulates the production of granulocytes in the bone marrow and both IL-6 and CXCL1 are known to regulate neutrophil trafficking; this may explain the higher neutrophil infiltration in KO animals (Fig. 3F). Despite higher neutrophil recruitment to the kidneys of KO mice, they remained susceptible to increased *C. albicans* colonization, indicating a problem with fungal clearance. To control for any baseline differences in cellular composition of blood, we sampled the mice and ran a CBC blood panel. Figure 4E shows that both genotypes display similar blood composition, as assessed by cell counts or measurements of: white blood cells, neutrophils, lymphocytes,

eosinophils, basophils, red blood cells, hemoglobin, hematocrit and platelets with nominal, albeit significantly lower monocyte counts in the KO mice. Taken together, the *in vivo* candidiasis model, clearly demonstrates that the *TRPM7*$^{fl/fl}$ *LysM-Cre* mice are highly susceptible to candida colonization and show higher systemic inflammation, which contributes to their drastically increased mortality. The findings establish a critical role for TRPM7 function in the innate immune response to fungal infections.

Trpm7-deficient macrophages are defective in the phagocytosis of yeast

Macrophages isolated from femurs and tibiae of *TRPM7*$^{fl/fl}$ *LysM-Cre* mice differentiate normally without developmental and immunotypic deficits[64], and on average express ~80% less *Trpm7* transcript (Fig. 6A). Since we observed increased mortality and a higher *C. albicans* burden in the kidneys of KO animals, we isolated and differentiated primary bone-marrow derived macrophages (BMDMs) and tested their killing efficiency in an *in vitro* killing assay. There was no significant defect in the killing efficiency of either *S. cerevisiae* or *C. albicans* yeast particles that were engulfed by the macrophages (Fig.5A-5B). The killing efficiency is normalized to the average amount of fungal pathogens engulfed by the phagocytes in T0 (explained in Methods). We plotted the engulfment efficiency and noticed a striking, nearly 50% decrease in the fungal uptake by KO

macrophages. Next, we used transmission electron microscopy (TEM) to visualize the yeast-containing phagosomes (Fig. 5C) and quantified the engulfed yeast in primary macrophages. Consistently, the number of internalized fungi was significantly lower in the KO BMDMs, as compared to WT at both incubation time points (Fig. 5D). Since TRPM7 has been implicated in cellular migration[69,70], adhesion and actomyosin contractility[60], we evaluated the migratory motility of KO macrophages. To test this, we performed a transwell (Boyden chamber) migration assay (outlined in Fig.S6B)[71]. The macrophages were freshly seeded onto well-inserts containing a porous (8 μm), polycarbonate membrane and their migration towards *C. albicans* in the lower chamber, was quantified at 6h. Non-migrated phagocytes were delicately scraped-off with a clean cotton swab and transmigrated cells were stained for counting. As summarized in Figure 6C, we observed a two-fold increase in the transmigration of both macrophage genotypes towards yeast containing media, as compared to the media-only control, and TRPM7 deficiency did not compromise migration. To test whether fungi decrease the viability of TRPM7 KO macrophages, we performed an LDH-release assay. We incubated macrophages with *S. cerevisiae* and *C. albicans* for 6 and 12h. The macrophage viability was affected to the same degree in each yeast strain, regardless of TRPM7 status (Fig. 6D). Phagocytes sensing fungal pathogens engage a number of pattern-recognition receptors for efficient engulfment of pathogens and for inflammatory signaling. These include Toll-like receptors

(TLRs)[72,73], C- type lectin receptors (CLRs)[74,75], NOD- like receptors (NLRs)[76] and RIG-I-like receptors (RLRs)[77]. Changes in the expression of these receptors can have a profound effect on phagocytosis and inflammation. Proteolytic cleavage of TRPM7 can release the kinase domain to phosphorylate histones in the nucleus and thus modify transcription[43]. We measured the mRNA expression of receptors implicated in anti-fungal response via RT-qPCR but found no transcriptional differences in the KO macrophages relative to their WT counterparts (Fig. 6E). In summary, we show that TRPM7 activity plays a significant role in fungal internalization, but this defect does not stem from disparities in migration, viability, or reduced expression of fungi-directed pattern-recognition receptors.

Pharmacological inhibition of Trpm7 channel activity mimics the engulfment defect observed in Trpm7-deficient macrophages

TRPM7 is a bifunctional protein encompassing a cation-conducting ion channel as well as a kinase. Although there are no specific inhibitors of the TRPM7 kinase activity, the TRPM7 channel activity can be effectively blocked by FTY720[62,78]. FTY720- treated (5 μM) primary WT macrophages showed significantly reduced yeast engulfment, recapitulating the engulfment defect seen in KO phagocytes. FTY720 is phosphorylated in vivo by sphingosine kinase 2 (SK2) and phospho-FTY720 (FTY720p) serves as an agonist for sphingosine-1 receptors (S1PRs)[78].

However, FTY720p does not inhibit TRPM7 current[62]. Both WT or KO phagocytes treated with FTY720p (5 μM) engulfed *S. cerevisiae* normally (Fig. 5E) and, the engulfment was largely abolished by the potent PLC inhibitor, U73122 (5 μM), which suggests that TRPM7 activation is downstream of PLC signaling. As shown for primary macrophages, the macrophage cell line RAW264.7 also showed significantly decreased engulfment when treated with FTY720. Predictably, ER27319 (Syk inhibitor) and U73122 also abolished engulfment in RAW cells (Fig. 5F). To further strengthen these results, we used an azacyclic FTY720 derivative AAL149[79], which inhibits TRPM7 without affecting S1PRs (Busey et al, *manuscript in preparation*). As a negative control, we used VPC01091.2p analog[80], a phospho-mimic derivative of FTY720, which cannot inhibit TRPM7. Both, FTY720 and AAL149 potently inhibited the engulfment of *S. cerevisiae* in RAW cells while VPC01091.2 did not show a defect. These data indicate that the TRPM7 ion channel activity plays a major role in yeast phagocytosis, but the results do not rule out the role of the TRPM7 kinase activity, which in principle, can act in coordination with the channel activity. In addition to regulating phagocytosis, TRPM7 could also regulate the anti-fungal inflammatory responses in macrophages. We stimulated primary macrophages with zymosan, a potent activator of TLR-2 and Dectin-1 signaling[81,82]. Both WT and KO macrophages showed similar mRNA expression of the inflammatory mediators: IL-6, IL-1β or TNFα (Fig. 6F). Conversely NOS2, CXCL1 and CCL4 showed differential

expression in the KO cells. We tested the nuclear translocation of major transcription factors downstream of TLR-2 and Dectin-1 signaling. Nuclear and cytosolic fractions were isolated and probed for NFκB, IRF3, IRF5 and STAT1. After normalizing to a resident nuclear protein (LSD1) and controlling for cytosolic fraction (GAPDH), we found no significant differences between WT and KO cells (Fig. 6G). Even though we see a clear reduction in expression of NOS2, CXCL1 and CCL4 *in vitro* with zymosan stimulation, the reverse is observed *in vivo*. This is likely a result of the involvement of other cell types in the inflammatory cascade. Overall, these results suggest that the striking susceptibility to lethal candidiasis is predominantly caused by the inability of the TRPM7-deficient macrophages to engulf and clear the pathogen, rather than cell-intrinsic defects in inflammatory gene expression downstream of the pattern-recognition receptors.

Engulfment of yeast activates TRPM7 current (I_{TRPM7}) in macrophages

Using Whole-cell Patch-clamp electrophysiology (WC-PCE), we measured TRPM7 current (ITRPM7) in macrophages that had already engulfed *C. albicans* (30 mins post engulfment). In Mg^{2+}- free solutions, the maximal I_{TRPM7} revealed spontaneously upon break-in was comparable to the I_{TRPM7} in unfed primary macrophages (Fig. 8A-8B). Recordings in RAW264.7 cells also yielded similar results (Fig 8D-8E). The WC-PCE conditions used for these recordings are

illustrated (Fig.8C). WC-PCE enables direct measurement of I_{TRPM7}, but the inherent limitation of WC-PCE is that it dialyzes the intracellular environment, disrupts the cytoskeleton and impedes phagocytosis. Since WC-PPE was unsuitable for the real time I_{TRPM7} measurement in macrophages engulfing fungal particles, we applied Perforated Patch-Clamp Electrophysiology (PPCE) wherein electrical access is gained through Nystatin-mediated pores in the plasma membrane rather than a full break-in that dialyzes the cytosol with the pipette solution (Fig.8F). In this configuration, we show that WT macrophages (Fig.7A) and RAW264.7 cells (Fig. 7C-7E) engaging zymosan particles develop an outwardly rectifying current that is inhibited by the TRPM7 blocker FTY720. The representative I-V signatures are shown in Figure 3A for WT macrophages and temporal development of this engulfment-triggered current (ETC) is shown in Figure S3G. The ETC fails to develop in macrophages that were treated with soluble fungal particles (Fig. 8H), signifying that physical contact of the insoluble particle is required for the current activation. Comparison of WT and KO macrophages showed that ETC also does not develop in Trpm7-/- macrophages (Fig.7B), indicating TRPM7-dependance on the activation of this outwardly rectifying current. The current densities are shown in Figure 7C. Overall, these data indicate that the ETC is at least dependent on TRPM7 if not mediated by TRPM7.

Trpm7 does not regulate zymosan-triggered Store-operated Ca^{2+} entry (SOCE)

Macrophage stimulated with yeast particles show robust elevations in intracellular Ca^{2+} through the store-operated Ca^{2+} entry (SOCE)[83,84]. Previously it was reported that TRPM7 kinase domain can modify the SOCE[61,85,86] through an undefined mechanism. To test whether the deletion of TRPM7 affects SOCE in macrophages, we tested Thapsigargin (TG, 1 μM) induced SOCE in Fura-2-AM-loaded BMDMs. TG is a potent inhibitor of ER-resident SERCA pumps and by stopping the re-uptake of Ca^{2+}, it empties the Ca^{2+} in the ER, with concomitant elevations in cytosolic Ca^{2+}. In essence, TG simulates the IP_3-mediated release of Ca^{2+} from the ER; depletion of ER-Ca^{2+} concentration then triggers a sustained entry of extracellular Ca^{2+} through the Orai channels in the plasma membrane. By adding TG to Fura-2AM-loaded BMDMs in Ca^{2+}-free conditions, we first isolated the Ca^{2+}-elevations resulting from the release of stored ER- Ca^{2+}. Depletion of ER-Ca^{2+} also activates the Orai channels but this influx of extracellular Ca^{2+} is only revealed later in the recording, upon the addition of 2 mM Ca^{2+} to the bath (Fig. 10A). These analyses show that there is no significant difference between WT and KO BMDMs in any aspect of SOCE. Ca^{2+} elevations resulting from the release of ER-Ca^{2+} (quantified at 150s time point; Fig.10B) were comparable and so was the ultimate entry of extracellular Ca^{2+} (quantified at 460 s time point; Fig.10C). Cyclopiazonic acid (CPA, 20 μM) [87], a reversible SERCA inhibitor, results in similar Ca^{2+} traces (Fig.10D-10F). Next, we tested SOCE in Fura-2- AM loaded WT and

KO BMDMs in response to zymosan. Cumulative Ca^{2+} traces, for each responding macrophage, were indistinguishable between the WT and KO cells (Fig.9A and Fig.9C) and the Ca^{2+} influx was entirely dependent on PLC activity, as PLC-inhibitor U73122 (2 μM) completely abolished Ca^{2+} traces in both macrophage populations (Fig.9B). The maximal cytosolic Ca^{2+} responses (Fig.9C) were also comparable. These results show that TRPM7 does not regulate SOCE triggered by the recognition of zymosan.

TRPM7-dependent Ca^{2+} signals are revealed when SOCE is artificially suppressed

At 100 mV, the single channel conductance of TRPM7 is ~40 pS but at macrophage resting potential (~-50 mV), the inward conductance is miniscule. This property may enable TRPM7 to mediate highly localized cationic currents comprising of Ca^{2+}, Zn^{2+} and Mg^{2+}. To unmask the Ca^{2+}- elevations mediated by TRPM7 from the larger whole cell Ca^{2+}-elevations mediated by SOCE, we treated the macrophages with CPA (20 μM) to deplete the ER-stored Ca^{2+} prior to zymosan treatment. After reducing the robust SOCE responses during zymosan treatment, we assessed Ca^{2+} elevations in Fura-2-AM-loaded WT and KO cells. The Ca^{2+} elevations in individual cells (Fig. 10G) revealed the diminution of both the frequency and amplitude of Ca^{2+} transients in the KO macrophages, when

compared to WT macrophages. In accord with these data, significantly reduced Ca^{2+}-signals are evident from the average of time-resolved individual traces and peak Ca^{2+} elevations (Fig. 10H). Encouraged by these results we performed longer, 38 min long Ca^{2+} recordings in response to *S. cerevisiae*. Since prolonged application of UV light is detrimental to cell viability, we loaded the cells with CalBryte520-AM Ca^{2+} dye instead. To our surprise, on average, the KO macrophages showed a clear reduction in Ca^{2+} elevations (Fig. 9D-9F). Comparison of Ca^{2+} traces for each cell in both populations shows that a subset of WT macrophages responds especially strongly but this subset is clearly absent in the KO population (Fig. 9F, representative image inserts). These data underscore the importance of TRPM7 dependent Ca^{2+}-signaling in response to yeast. Zymosan particle size on average is ~3 μm[88], while most live yeast cells are 5-10 μm[89]. This observation prompted us to investigate the influence of particle size on TRPM7-dependent phagocytosis.

TRPM7 regulates the formation and sealing of the phagosome.

During the measurements of Ca^{2+}-elevations, we observed that the macrophages register a Ca^{2+}- spike when they first encounter the yeast particles. These results suggested that during phagocytosis of fungi, TRPM7 functions in the in the efficient formation of phagosome rather than its maturation post-internalization. To test this

hypothesis, we took an experimental approach wherein the biotinylated *S. cerevisiae* are stained with two different fluorophores before and after the initiation of phagocytosis. As illustrated (Fig. 11A), the biotinylated yeast are first stained with Streptavidin-Alexa568 (S-568) without saturating the biotinylation sites. The S-568 labeled yeast are then offered to macrophages for phagocytosis and the phagocytosis is halted with formaldehyde fixation at 15 and 30 mins. The fixed cells were then stained (without permeabilization) with Streptavidin-Alexa488 (S-488) to reveal the yeast surfaces that were still accessible to the streptavidin conjugate. This method allowed us to evaluate both the formation of the nascent phagosome and its sealing. Fully sealed phagosomes would be fluorescently stained with S-568 but not S-488. Conversely, partially sealed phagosomes would be fluorescent in both channels (Alexa568 and Alexa-488) marking the still exposed, biotinylated cell wall of partially engulfed yeast. Manual counting of fully and partially internalized yeast particles revealed that at 15 mins the progression of phagocytosis was equivalent in both WT and KO macrophages (Fig. 12A). There were no differences in the percentage of fully engulfed and partially engulfed yeast particles. However, at 30 mins, the KO macrophages display a clear decrease in the number of completely engulfed yeast (Fig. 11C). Quantifying across confocal images also revealed a significantly higher percentage of partially engulfed yeast in KO macrophages (Fig. 11D). These results indicate that TRPM7 regulates phagocytic flux and is especially important for phagosomal sealing when multiple

particles are engulfed by the macrophage. To test whether the role of TRPM7 in phagosome sealing was dependent on the size of the cargo, we evaluated the phagocytosis of 3 μm and 6 μm beads that were conjugated with β-glucan to mimic fungal particles[90]. These beads were then biotinylated and subjected to the method described above to assess the phagocytosis efficiency. Our experiments show that the number of phagocytosed 3 μm beads decreased in KO macrophages, however both WT and KO phagocytes display comparable efficiency of phagosomal sealing (Fig. 11E). Consistent with our observations, the KO macrophages significantly reduced the number of fully internalized 6 μm beads (Fig. 11F). Additionally, Trpm7- deficient phagocytes display significantly reduced sealing of phagosomes containing 6 μm beads (Fig. 11F). These results indicate that TRPM7 plays an important role in phagocytosis of larger cargo, and this is consistent with our observation that *Trpm7-/-* macrophages are not deficient in the phagocytosis of bacterial pathogens (Fig.12B).

Trpm7-/- macrophages also display abnormal actin morphology, shallower phagocytic cups, and fewer podosome-like structures during phagocytosis.

TRPM7 function regulates actomyosin contractility and phosphorylates myosin-IIA[42,60]. We therefore assessed the structural architecture of myosin-IIA filaments in the KO macrophages and observed a non-uniform distribution throughout the

cell (Fig.13A) despite normal protein levels of myosin-IIA and Myosin heavy chain 9, even after exposure to *C. albicans* (Fig. 13B). Recently, it was shown that F-actin nucleation through Arp2/3 exerts constricting forces around the phagosome and myosin-II is crucial during phagocytic cup closure[91]. To define actomyosin structural abnormalities, we stained F-actin during the early stages of *C. albicans* internalization (5 min). Using confocal AiryScan microscopy (Fig. 13C) and 3D-rendered Imaris projections of z-stacks through the phagocytic cups (Fig. 13D) we show that both, WT and KO macrophages displayed a dense F-actin staining around the yeast-containing phagosomes (Fig. 13C). However, there were fewer phagocytic cups in the KO cells and a great proportion had decreased depth when compared to those seen in the WT macrophages (Fig. 13D). We also detected a striking difference in the number of dense actin-rich podsome-like structures between WT and KO cells (Fig. 13C), which were previously suggested to serve as a site for actin polymerization and aid in phagocytosis[92,93]. Overall, our results establish TRPM7 as a critical regulator of anti-fungal host defense. This emerges from a fundamental role of TRPM7 in phagocytosis of fungal pathogens. We have shown that a TRPM7-dependent current is activated during phagocytosis and TRPM7 regulates cytoskeletal rearrangements salient to the formation and sealing of nascent phagosomes.

Discussion

Our study identifies TRPM7 as a crucial regulator of the innate immune response against fungal pathogens. As an ion channel, TRPM7 activity can be both activated and inhibited through pharmacology [94,95]. In the specific case of anti-fungal host defense, our findings suggest that modulation of TRPM7 activity could influence the phagocytic anti-fungal innate immune responses, more efficiently sequester the invasive yeast in phagosomes and be beneficial even against drug-resistant strains. Currently, specific activators of TRPM7 are not available to test whether such drugs can accentuate anti-fungal defenses, but we hope that this study encourages the development of such modulators. Our study focused on *C. albicans*, and at this point, the functional significance of TRPM7 in broad anti-fungal immunity is a reasonable conjecture that future studies will address more concretely. Beyond the overarching significance of TRPM7 in anti-fungal host defense, and at a more mechanistic level, our findings show that TRPM7 function in macrophages is crucial for the efficient phagocytic clearance of *C. albicans* and it translates to other yeast species. TRPM7 is known to regulate cytoskeletal rearrangements through the regulation of actomyosin contractility[42,60,96] and in a related aspect, it has also been implicated in the formation of actin-dense protrusions called podosomes[42,70]. In cue with these findings, we discovered that TRPM7 regulates the formation and sealing of phagocytic cups. In accord with

previous studies, this is most likely through the regulation of myosin IIA contractile rings formation around the phagocytic cup. We also observed that deletion of TRPM7 greatly abrogates the formation of actin-dense podosome-like structures during phagocytosis. In line with a recent study[91], podosomes are a site of actin nucleation serving to exert constricting forces on the phagocytosed target. *In vivo*, podosomes have been shown to play an important role in the proteolytic degradation of the extracellular matrix, by binding collagen and initiating its phagocytosis[97–100]. This could be a salient factor for the phagocytic clearance of fungi in the 3D tissue environment where the invading fungi are lodged in the interstitial space. Our analyses of phagocytosis were carried out in conventional cell culture and it is likely that this underestimates the functional salience of TRPM7 in phagocytic processes that occur in the context of tissue architecture and physiology. Consistent with this possibility, we found a striking increase in the *C. albicans* burden in the histological sections of kidneys of *Trpm7*- targeted mice. The molecular mechanisms through which TRPM7 regulates cytoskeletal rearrangements reinforcing phagosome dynamics and podosome formation are outside the scope of this study but there is a hypothetical framework based on previous findings. The phosphorylation of non-muscle myosin heavy chain by TRPM7[42] is a likely regulatory component. We also found that blocking the channel activity of TRPM7 with FTY720 recapitulated the phagocytosis phenotype seen in *Trpm7*-deficient macrophages. The salient role of TRPM7 channel activity is also

supported by the important finding that TRPM7 channel is activated during the early stages of phagocytosis. In the specific case of TRPM7, we propose that the activation of TRPM7 during the early stages of phagocytosis mediates electrical signals necessary for actomyosin contractility and associated cytoskeletal rearrangements. These include local Ca^{2+}-signals but it should be noted that TRPM7 also conducts other cations, such as Na^{+}, Zn^{2+} and Mg^{2+}. In addition to mediating signals through these cationic second messengers, TRPM7 activity at the phagocytic cup will also result in the depolarization of the phagosomal membrane potential and this biophysical feature may be an important regulator of signaling in that microenvironment. In vertebrates, bifunctional configuration of TRPM7 is highly conserved and this supports the conjecture that TRPM7 coordinates the channel and kinase activities for cell signaling. But the nature of such bifunctional coordination has not been defined because we lack the molecular tools necessary to observe the real-time activity of the kinase and we also lack selective inhibitors of TRPM7 kinase activity. Previous studies using site-directed mutagenesis were carried out in generic cell lines that are easy to transfect[101–103] and lacked tissue specific context to capture definite conclusions about the kinase activity *in vivo*. Studying the specific process of engulfment may offer an attractive platform for elaborate mechanistic studies on how TRPM7 mediates cell signaling. In addition to the functional characterization of TRPM7, we have made an important technical advance by employing perforated patch clamp

electrophysiology in actively phagocytosing primary macrophages. Previous efforts to measure the electrical signals accompanying phagocytosis were carried out in whole cell configuration [104] but this impedes the phagocytic process. Thus, our technical approach opens a more refined path toward understanding the electrical signals mediated during phagocytosis. The TRPM7-dependent engulfment-triggered current (ETC) we have discovered is likely a composite of multiple channels that are activated during phagocytosis of yeast. For instance, the cytoskeletal rearrangements initiated by TRPM7 may then activate downstream channels that are highly sensitive to membrane cortical tension. The definitive dissection of the components of ETC and their activation mechanisms will be a topic for our future studies.

Previously, we reported that the loss of TRPM7 blunts LPS-induced inflammatory signaling[64]. Together, these studies offer a conceptually coherent framework of TRPM7 function in innate immunity. TRPM7 function in macrophages is dependent on the cellular context dictated by the primary signals emanating from the specific pattern-recognition receptors. In the context of TLR4 activation, TRPM7 regulates the internalization of TLR4 and the formation of such signaling endosomes drives robust inflammatory gene expression. In the case of Dectin-1 signaling (anti-fungal response), TRPM7 promotes phagocytosis of the fungi. In both cases, the essence of TRPM7's cell biological function appears to be the orchestration of membrane

and cytoskeletal and membrane dynamics necessary for endocytic processes.

CHAPTER TWO FIGURES

Figure 3

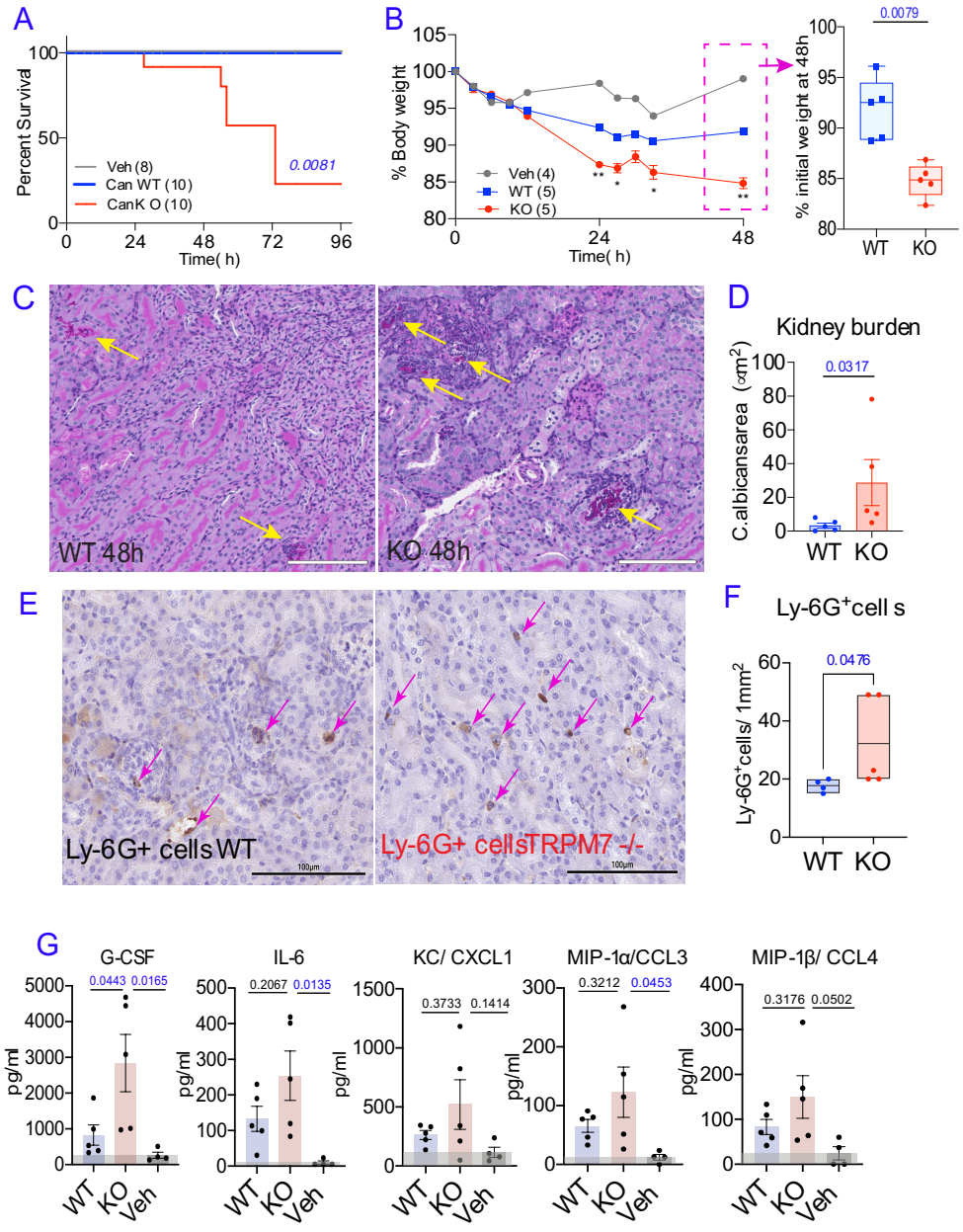

Figure 3. *TRPM7*$^{fl/fl}$ *LysM-Cre* display defect in *C. albicans* clearance

(A) Kaplan- Meier survival analysis of *TRPM7*$^{fl/fl}$ (WT; blue, n= 10) and *TRPM7*$^{fl/fl}$ *LysM-Cre* (KO; red, n=10) mice injected intravenously with 100µl 1x10^6 *C. albicans* and assessed over 96 hours. Control mice were injected with 0.9% saline solution (Veh) and were both WT (n=4) and KO (n=4) outlined in grey line. Curve comparison was performed using a log-rank (Mantel- Cox) test with a p= 0.0081.

(B) Body weight loss overtime, presented as a % of initial weight for WT (n=5, blue), KO (n=5, red) and vehicle injected control mice (WT, n=2; KO, n=2). Statistics performed with a 2way AVOVA with multiple comparisons *p=<0.05, ** p=<0.005. Right panel: box and whisker plot (min to max) showing cumulative % initial body weight at 48 h. Statistics performed with a two- tailed t test (Mann-Whitney).

(C) Periodic-acid Schiff (PAS) stained kidney sections collected at 48 h from WT and KO mice (n=5 each; WT blue, KO- red) injected with *C. albicans*. Yellow arrows indicate *C. albicans* colonies.

(D) Quantification of PAS staining by outlining and counting the affected areas (in µm^2) colonized by *C. albicans* in each kidney section. Statistics performed with a two- tailed t test (Mann-Whitney). Error bars represent SEM for individual samples.

(E) Representative kidney sections stained with anti- Ly-6G antibody harvested

from WT (left panel) and KO (right panel) mice at 48h. Magenta arrows indicate positively stained cells (brown color). Scale bar is 100 μm.

(F) Quantification of anti-Ly-6G stained kidney sections per 1 mm^2 area, 48 h post *C. albicans* injections in WT(blue, n=5) and KO (red, n= 5) mice. Data were plotted as floating bars and statistics were performed using two-tailed t test (Mann-Whitney).

(G) Measurement of serum cytokines at 48h post-*C. albicans* injections via Luminex Multiplex assay. The data were plotted for WT (n= 5, blue bars), KO (n=5, red bars) and PBS controls (grey bars, n=4). Statistics performed with an ordinary one-way ANOVA, error bars represent SEM.

Figure 4

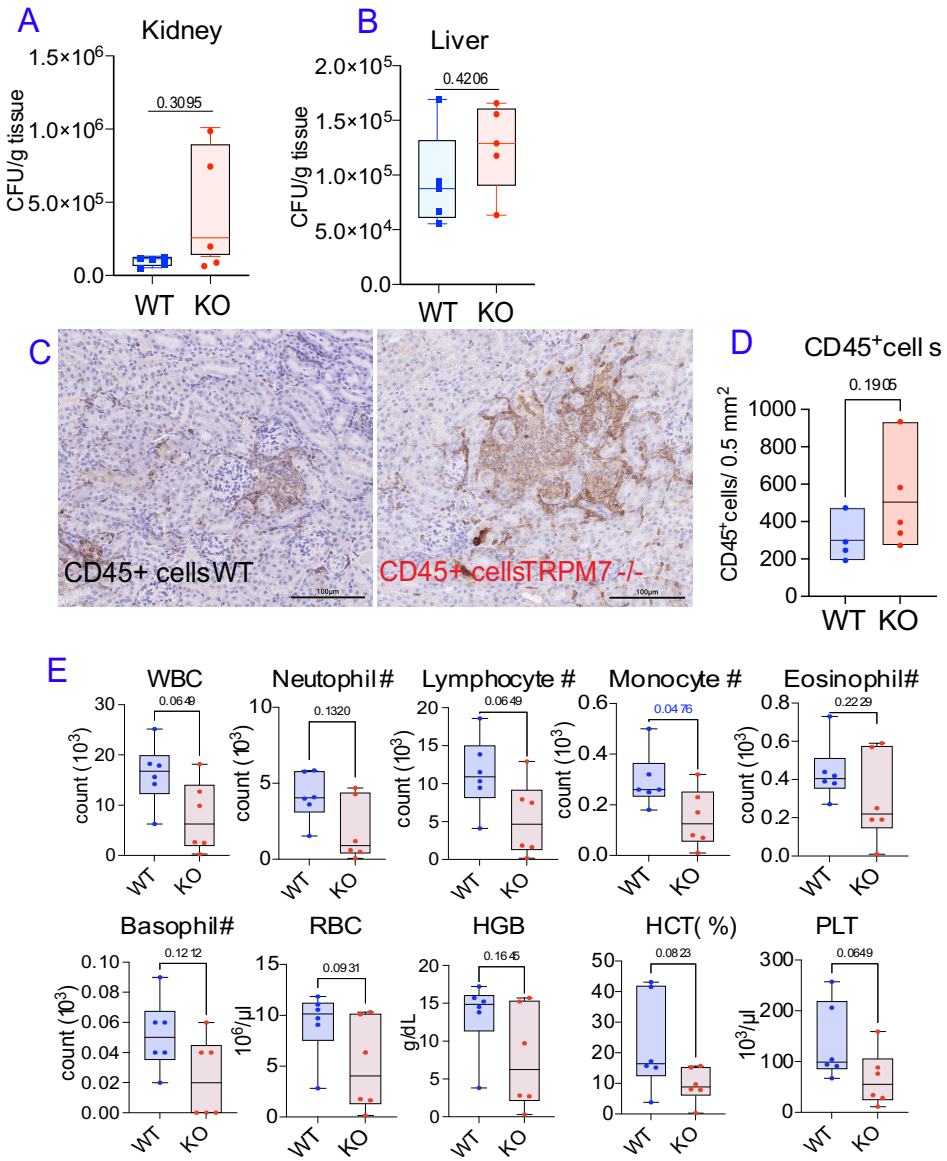
A
Kidney
CFU/g tissue
0.3095
WT KO
B
Liver
CFU/g tissue
0.4206
WT KO
C
CD45+ cells WT
CD45+ cells TRPM7 -/-
D
CD45+cell s
CD45+cells/ 0.5 mm2
0.1905
WT KO
E
WBC
0.0649
Neutophil#
0.1320
Lymphocyte #
0.0649
Monocyte #
0.0476
Eosinophil#
0.2229
Basophil#
0.1212
RBC
0.0931
HGB
0.1645
HCT(%)
0.0823
PLT
0.0649
count (10^3)
10^6/µl
g/dL
10^3/µl
WT KO

Figure 4. *TRPM7*$^{fl/fl}$ *LysM-Cre* show similar infiltration of CD45^{+} cells and cell numbers in the CBC panel

(A) Colony forming units (CFUs)/g tissue of *C. albicans* retrieved from kidneys at 48 h (n= 5 mice each, WT blue, KO- red). Vehicle control mice had no CFUs. Graphs are represented by a box and whisker plot. Statistics show two-tailed t test (Mann-Whitney).

(B) Colony forming units (CFUs)/ g tissue of *C. albicans* retrieved from livers at 48h (n= 5 mice each, WT- blue, KO- red). Vehicle control mice had no CFUs. Graphs are represented by a box and whisker plot. Statistics show two-tailed t test (Mann-Whitney).

(C) Representative kidney sections stained with anti-CD45 antibody for WT (left panel) and KO (right panel). Scale bar is 100 μm.

(D) Quantification of anti-CD45 stained kidney sections/0.5 mm^2 area at 48h post *C. albicans* injections in WT (blue, n=5) and KO (red, n= 5) mice. Data was plotted as floating bars and statistics were performed using two-tailed t test (Mann-Whitney).

(E) Complete blood count (CBC) panel for WT (n=6, blue) and KO (n=6, red) mice. Data represents box and whiskers. Statistics performed with a two-tailed t test (Mann-Whitney).

Figure 5

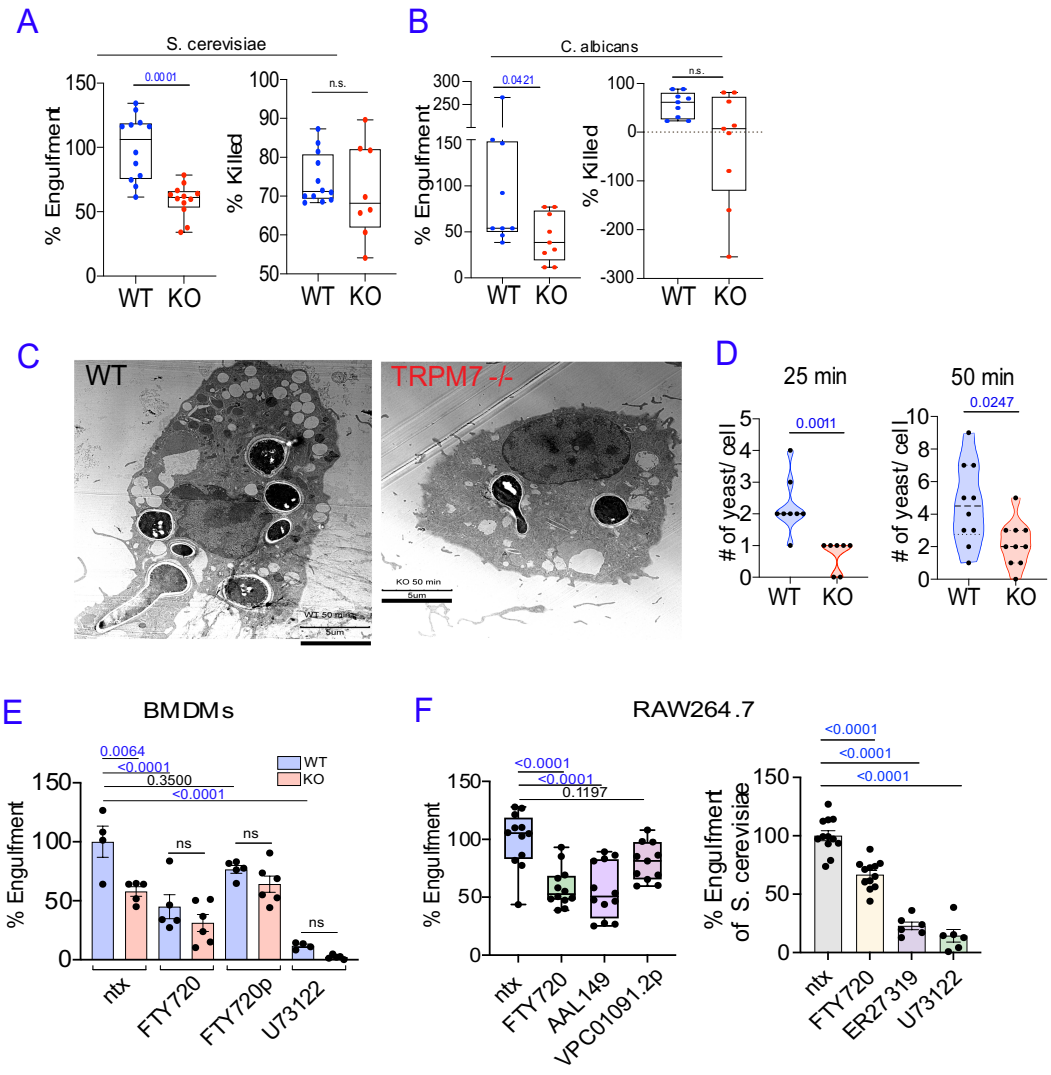
A
S. cerevisiae
% Engulfment
% Killed
0.0001
n.s.
WT KO
B
C. albicans
0.0421
n.s.
C
WT
TRPM7 -/-
D
25 min
50 min
# of yeast/ cell
0.0011
0.0247
E
BMDMs
0.0064
<0.0001
0.3500
<0.0001
WT
KO
ns
ntx
FTY720
FTY720p
U73122
F
RAW264.7
<0.0001
0.1197
AAL149
VPC01091.2p
% Engulfment of S. cerevisiae
ER27319

Figure 5. Macrophages deficient in TRPM7 activity are defective in the phagocytosis of yeast

(A) *S. cerevisiae* engulfment (left panel) and killing (right panel) assays quantified for WT (n= 12, blue dots) and KO (n= 12, red dots) BMDMs. Statistics performed with a two-tailed t test (Mann-Whitney).

(B) *C. albicans* engulfment (left panel) and killing (right panel) assays quantified for WT (n= 9, blue dots) and KO (n= 9, red dots) BMDMs. Statistics performed with a two-tailed t test (Mann-Whitney).

(C) Representative transmission electron microscope (TEM) micrographs for WT (left) and KO (*TRPM7-/-*, right) macrophages at 50 min post *C. albicans* engulfment. Scale bar= 5 μm.

(D) Quantification of engulfment of *C. albicans* per cell, derived from TEM micrographs at two tested time points: 25 min (left) and 50 min (right) for WT (blue shaded violin plot, 25 min n=8; 50 min n=10) and KO (red shaded violin plot, 25 min n=7; 50 min n=10). Statistics performed with a two- tailed t test (Mann-Whitney).

(E) Engulfment assay using *S. cerevisiae* in WT (blue) and KO (red) primary macrophages, denoted as % engulfment (n=4-5, as shown by individual dots). Macrophages were treated with inhibitors, as outlined in the figure: FTY720 (5μM), phosphorylated FTY720 (FTY720p; 5μM) and a PLC inhibitor U73122 (5μM). Statistics were performed with ordinary one-way

ANVOA.

(F) Engulfment assay of *S. cerevisiae* by RAW 264.7 cells treated with inhibitors, as outlined in the figure: FTY720 (5 μM), Syk inhibitor ER27319 (10μM), PLC inhibitor U73122 (5 μM), FTY720 derivative AAL149 (5 μM) and phosphorylated FTY720 derivative VPC1091.2p (5 μM). Engulfment efficiency is expressed as % engulfment. Statistics were performed with one-way ordinary ANOVA. Data in the left panel are represented by box and whiskers plots and the error bars for data in the right panel are SEM.

Figure 6

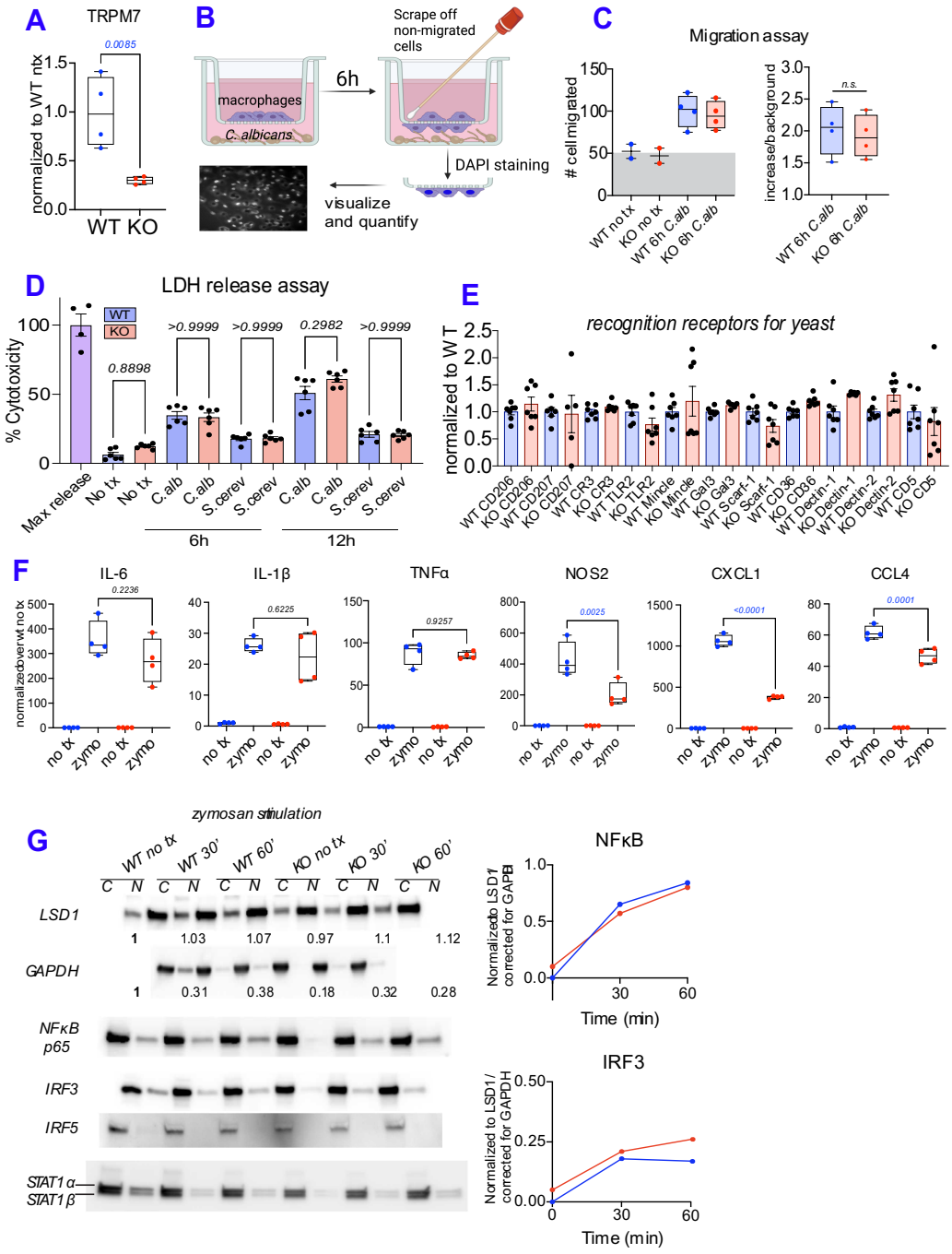
A
TRPM7
0.0085
normalized to WT ntx
WT KO
B
Scrape off non-migrated cells
6h
macrophages
C. albicans
DAPI staining
visualize and quantify
C
Migration assay
cell migrated
WT no tx
KO no tx
WT 6h C.alb
KO 6h C.alb
increase/background
n.s.
D
LDH release assay
% Cytotoxicity
WT
KO
0.8898
>0.9999
>0.9999
0.2982
>0.9999
Max release
No tx
C.alb
S.cerev
6h
12h
E
recognition receptors for yeast
normalized to WT
F
IL-6
IL-1β
TNFα
NOS2
CXCL1
CCL4
normalized over wt no tx
0.2236
0.6225
0.9257
0.0025
<0.0001
0.0001
no tx
zymo
G
zymosan stimulation
WT no tx
WT 30'
WT 60'
KO no tx
KO 30'
KO 60'
C
N
LSD1
GAPDH
1
1.03
1.07
0.97
1.1
1.12
0.31
0.38
0.18
0.32
0.28
NFκB p65
IRF3
IRF5
STAT1α
STAT1β
NFκB
Normalized to LSD1/ corrected for GAPDH
Time (min)
IRF3

Figure 6. TRPM7- deficient macrophages display normal characteristics *in vitro*

(A) *Trpm7* gene expression analysis (qPCR) in primary macrophages, isolated from *TRPM7*$^{fl/fl}$ (WT, blue dots) and *TRPM7*$^{fl/fl}$ *LysM-Cre* (KO, red dots), normalized to WT macrophage expression. Data were graphed as box and whiskers plot. Statistics performed with a two- tailed t test (Mann-Whitney).

(B) Graphical outline of transwell migration assay performed with primary macrophages.

(C) Quantification of transwell migration assay. Left panel: the number of migrated WT (blue) and KO (red) macrophages at baseline (no tx, media only control) and 6h post-incubation with *C. albicans*. Each dot represents an average of 10 different ROIs. Right panel: data expressed as increased over baseline migration for WT (blue) and KO (red) macrophages incubated with *C. albicans* for 6h. Statistics performed with a two-tailed t test (Mann-Whitney).

(D) Lactate dehydrogenase (LDH) release assay assessing macrophage viability during incubation with yeast species: *C. albicans* (*C. alb*) or *S. cerevisiae* (*S. cerev*) for 6h and 12h. WT macrophages (n=6) are denoted in blue, whilst KO macrophages (n=6), positive control (n=4), denotes the maximal LDH release (purple). Statistics show ordinary one-way ANOVA with multiple comparisons.

(E) Gene expression analysis (qPCR) of selected receptors at baseline in WT

(blue) and TRPM7 KO (red) primary macrophages. Data are represented as fold change over WT (n=4-7, as indicated in the figure).

(F) Gene expression analysis (qPCR) for selected inflammatory cytokines for WT (blue) and KO (red) cells that were untreated (no tx) or treated with zymosan (zymo) for 3h. Statistics were performed with ordinary one-way ANOVA.

(G) Western blot analysis of fractionation experiment for WT and KO macrophages treated with zymosan for indicated times (30 or 60 min). C-cytoplasmic fraction; N-nuclear fraction, no tx-untreated. The representative graphs on the right show the densitometric quantification of the band intensities for NFκB and IRF3, normalized to LSD1 and corrected for GAPDH “contamination” in the nuclear fraction.

Figure 7

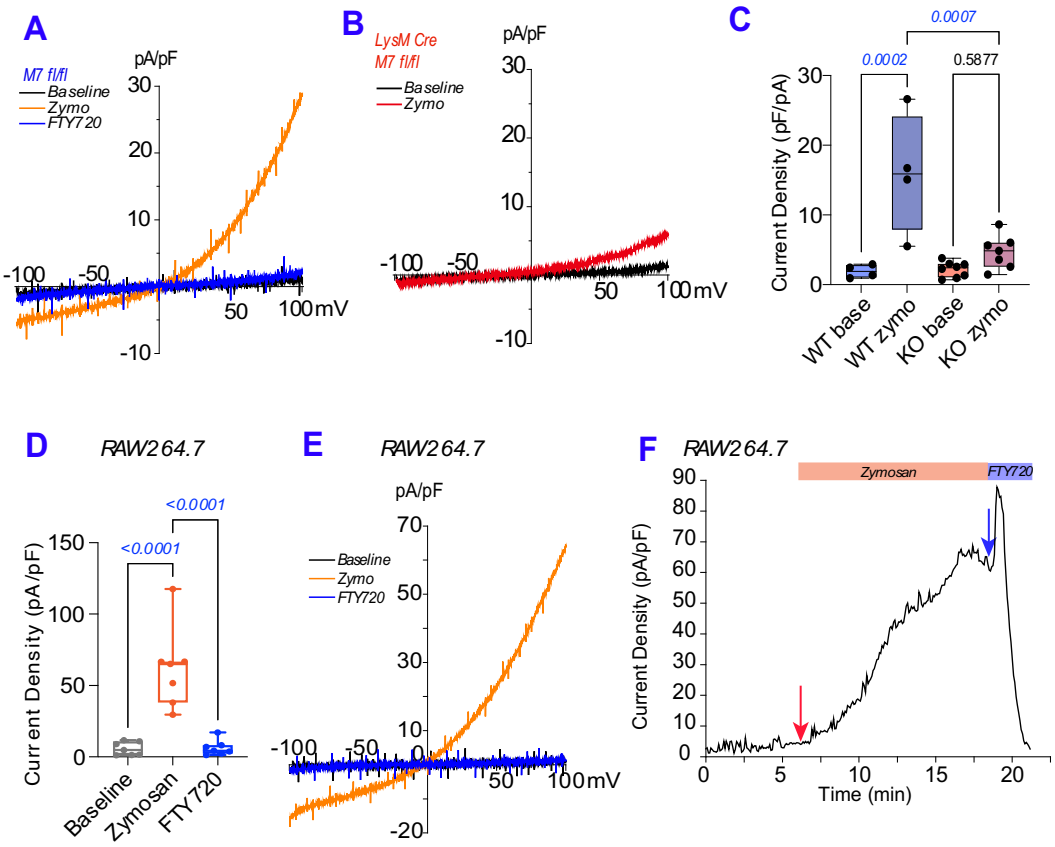
A
M7 fl/fl
Baseline
Zymo
FTY720
pA/pF
30
20
10
-10
-100
-50
50
100mV
B
LysM Cre
M7 fl/fl
Baseline
Zymo
pA/pF
30
20
10
-10
-100
-50
50
100mV
C
0.0007
0.0002
0.5877
Current Density (pF/pA)
30
20
10
0
WT base
WT zymo
KO base
KO zymo
D
RAW264.7
<0.0001
<0.0001
Current Density (pA/pF)
150
100
50
0
Baseline
Zymosan
FTY720
E
RAW264.7
pA/pF
Baseline
Zymo
FTY720
70
50
30
10
-20
-100
-50
50
100mV
F
RAW264.7
Zymosan
FTY720
Current Density (pA/pF)
90
80
70
60
50
40
30
20
10
0
0
5
10
15
20
Time (min)

Figure 7. Engulfment triggered current (ETC) is absent in TRPM7-deficient cells

(A) I-V relationship of ETC in WT BMDMs recorded in PPCE configuration; showing baseline trace (black), zymosan-activated current (orange) and FTY720 (5 μM)-inhibited current (blue).

(B) I-V relationship of ETC in KO BMDMs recorded in PPCE configuration; showing baseline trace (black), zymosan-activated current (red)

(C) Current densities of ETC obtained in WT and KO BMDMs using PPCE; showing baseline for each macrophage genotype (WT base, KO base) and zymosan-activated currents (WT zymo, KO zymo). All currents were quantified at 100 mV. Statistics were performed with ordinary one-way ANVOA with multiple comparisons.

(D) Current densities of ETC obtained in RAW264.7 cells using PPCE; showing baseline (gray, no currents), zymosan-activated currents (orange) and FTY720 (5 μM) inhibited currents (blue). All currents were quantified at 100 mV. Statistics were performed with ordinary one-way ANVOA.

(E) Representative I-V relationship of ETC in RAW264.7 cells, showing baseline trace (black), zymosan activated current (orange) and FTY720 (5 μM) inhibited current (blue). Note that the black and blue traces are overlapping.

(F) Current density over time in RAW264.7 cells, after addition of zymosan (orange arrow) in a PPCE configuration. Current increased overtime and

stabilized at ~10 min. FTY720 (5 μM) inhibited the current. Total recording time was 23 min.

Figure 8

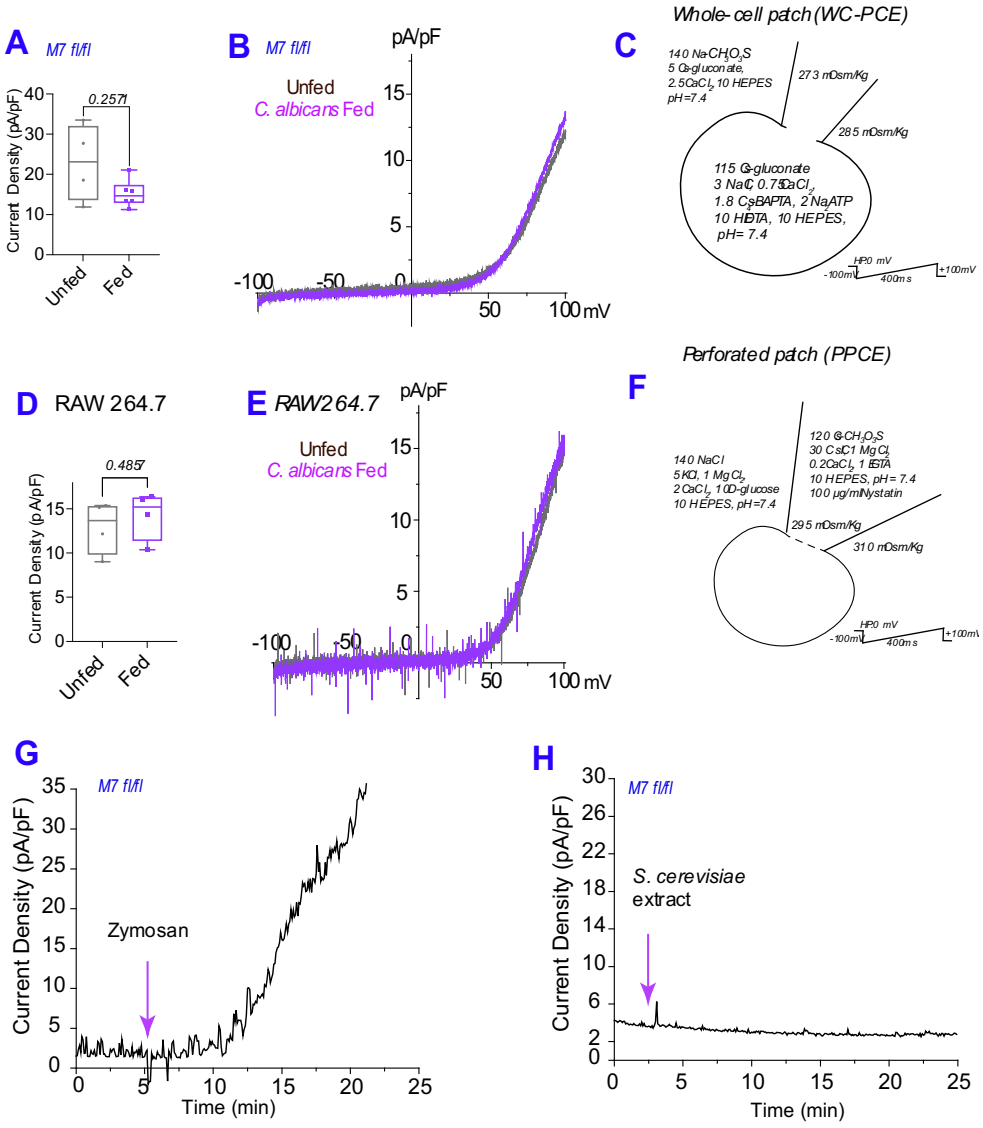
A
M7 fl/fl
Current Density (pA/pF)
0.257
Unfed
Fed
B
M7 fl/fl
pA/pF
Unfed
C. albicans Fed
-100
-50
50
100 mV
C
Whole-cell patch (WC-PCE)
140 Na-CH3O3S
5 Cs-gluconate,
2.5 CaCl2, 10 HEPES
pH=7.4
273 mOsm/Kg
285 mOsm/Kg
115 Cs-gluconate
3 NaCl, 0.75 CaCl2
1.8 CsBAPTA, 2 Na2ATP
10 HEDTA, 10 HEPES,
pH= 7.4
HP0 mV
-100mV
400ms
+100mV
D
RAW 264.7
Current Density (pA/pF)
0.485
Unfed
Fed
E
RAW264.7
pA/pF
Unfed
C. albicans Fed
-100
-50
50
100 mV
F
Perforated patch (PPCE)
140 NaCl
5 KCl, 1 MgCl2
2 CaCl2, 10 D-glucose
10 HEPES, pH=7.4
120 Cs-CH3O3S
30 CsCl, 1 MgCl2
0.2 CaCl2, 1 EGTA
10 HEPES, pH= 7.4
100 µg/ml Nystatin
295 mOsm/Kg
310 mOsm/Kg
HP0 mV
-100mV
400ms
+100mV
G
M7 fl/fl
Current Density (pA/pF)
Zymosan
Time (min)
H
M7 fl/fl
Current Density (pA/pF)
S. cerevisiae
extract
Time (min)

Figure 8. Whole-cell I_{TRPM7} is insensitive to engulfment of yeast

(A) TRPM7 current densities obtained using WC-PCE configuration in WT BMDMs before (gray) and 30 min post-incubation with *C. albicans* (purple, "fed"). Currents were quantified 5 min after break-in at 100 mV. Data shown as box and whiskers plot. Statistics performed with a two-tailed t test (Mann-Whitney).

(B) Representative current-voltage (I-V) relationship of ITRPM7 in untreated WT BMDMs (black trace) and *C. albicans* treated BMDMs (30 min, purple trace).

(C) Illustration of WC-PCE conditions used to isolate and measure ITRPM7. Composition of internal (pipet) and external (bath) solutions are shown. The voltage ramp parameters used to derive the I-V relationship ofITRPM7 are shown together with the filtering and sampling parameters used for signal processing.

(D) TRPM7 current densities in RAW cells in WC-PCE configuration, before and 30 min post-incubation with *C. albicans* (Fed). Currents were quantified 5 min after break-in at 100 mV. Statistics performed with a two-tailed t test (Mann-Whitney).

(E) Representative current-voltage (I-V) relationship of ITRPM7 in untreated (black trace) and *C. albicans* treated RAW cells (30 min, purple trace) obtained in WC-PCE configuration.

(F) Cartoon of the conditions used to measure ETC using the PPCE configuration. Composition of internal (pipet) and external (bath) solutions are outlined but the internal solution does not dialyze the cell through the perforated patch. The voltage ramp is shown together with the filtering and sampling parameters used for signal processing.

(G) Representative ETC current density trace over time in WT BMDMs after addition of zymosan obtained using PPCE configuration (purple arrow). Current activation is observed ~5 min after adding zymosan (purple arrow). Total recording time was 20 min.

(H) Current density over time (PPCE configuration) with the addition of soluble *S. cerevisiae* extract suspended in bath solution. No current activation was recorded over 25 min despite achieving electrical access in the perforated patch (Access resistance was <30 MΩ).

Figure 9

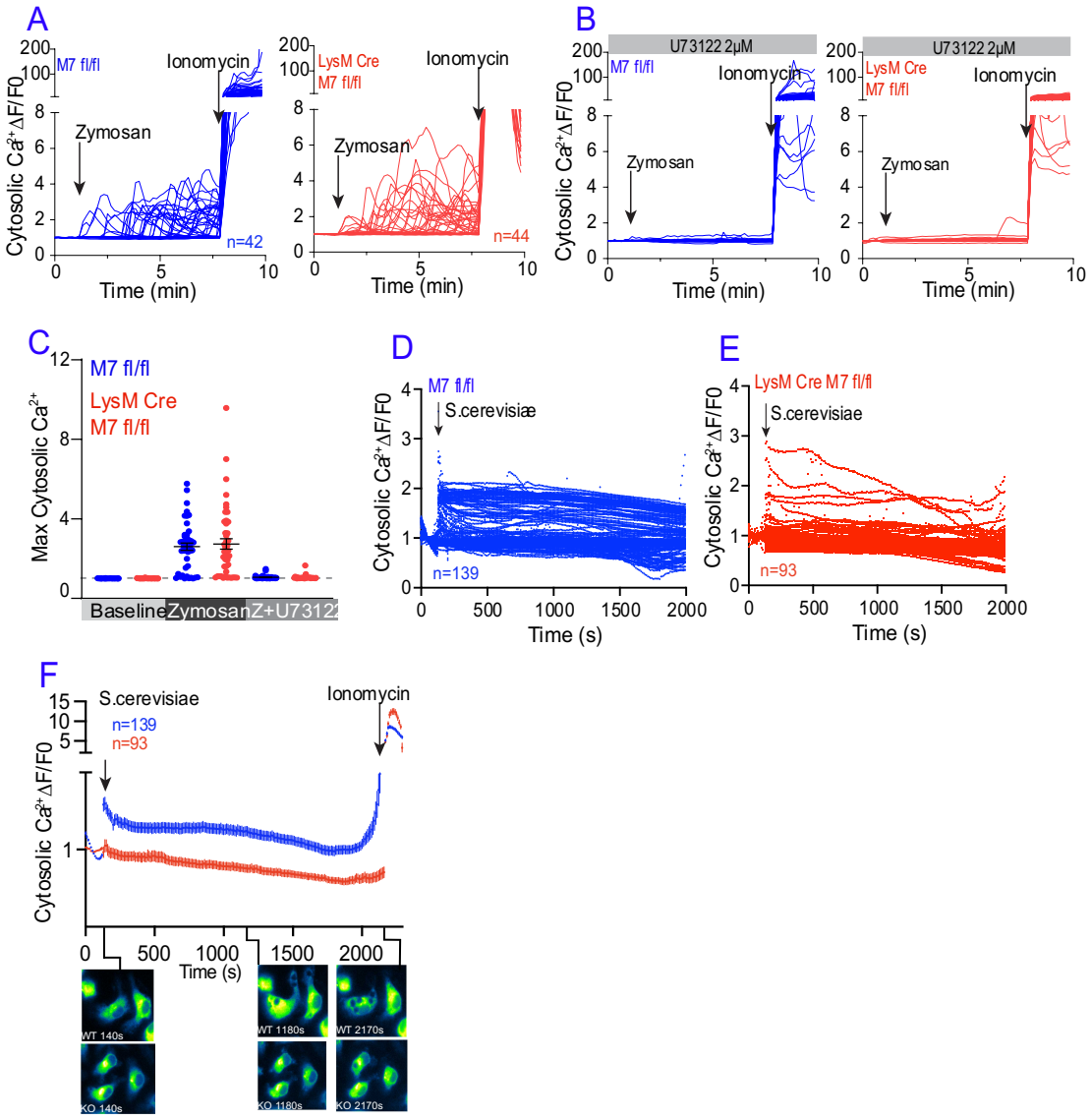
A
M7 fl/fl
Ionomycin
Zymosan
n=42
Time (min)
LysM Cre
M7 fl/fl
Ionomycin
Zymosan
n=44
Time (min)
Cytosolic Ca2+ ΔF/F0
B
U73122 2μM
M7 fl/fl
Ionomycin
Zymosan
Time (min)
U73122 2μM
LysM Cre
M7 fl/fl
Ionomycin
Zymosan
Time (min)
C
M7 fl/fl
LysM Cre
M7 fl/fl
Max Cytosolic Ca2+
Baseline
Zymosan
Z+U7312
D
M7 fl/fl
S.cerevisiæ
n=139
Time (s)
E
LysM Cre M7 fl/fl
S.cerevisiae
n=93
Time (s)
F
S.cerevisiae
n=139
n=93
Ionomycin
Cytosolic Ca2+ ΔF/F0
Time (s)
WT 140s
WT 1180s
WT 2170s
KO 140s
KO 1180s
KO 2170s

Figure 9. TRPM7-dependent Ca^{2+} signals are revealed during yeast, but not zymosan engulfment

(A) Individual cytosolic Ca2+ traces in Fura-2-AM loaded *TRPM7*$^{fl/fl}$ (WT, blue, n=42) and *TRPM7*$^{fl/fl}$ *LysM-Cre* (KO red, n=44) BMDMs were stimulated with zymosan. Ionomycin (1 μM) added at the end of the recording controlled for dye responsiveness in the cells. The values were calculated as a change in fluorescence/initial fluorescence (ΔF/F0).

(B) Ca^{2+} traces in Fura-2-AM loaded WT (blue, n=42) and KO (red, n=44) BMDMs stimulated with zymosan in the presence of U73122 (2 μM), a potent PLC inhibitor. The values were calculated as a change in fluorescence/initial fluorescence (ΔF/F0).

(C) Summary data from panels 4A and 4B. Average peak cytosolic Ca^{2+} in WT (blue, n=42) and KO (red, n=44) macrophages quantified from Fig. 4A and Fig. 4B. PLC inhibitor U73122 (2 μM) abrogated the Ca^{2+} elevations. Error bars represent SEM.

(D) Individual cytosolic Ca^{2+} traces in CalBryte^{TM}520-loaded WT (n=139) BMDMs stimulated with *S. cerevisiae*.

(E) Individual cytosolic Ca^{2+} traces in CalBryte^{TM}520- loaded KO (n=93) BMDMs stimulated with *S. cerevisiae*.

(F) Average cytosolic Ca^{2+} traces in CalBryte^{TM}520-loaded WT (blue trace) and KO (red trace) BMDMs in response to *S. cerevisiae*. Representative

snapshots of WT (upper panel) and KO (lower panel) macrophages responding to *S. cerevisiae* at indicated times are shown.

Figure 10

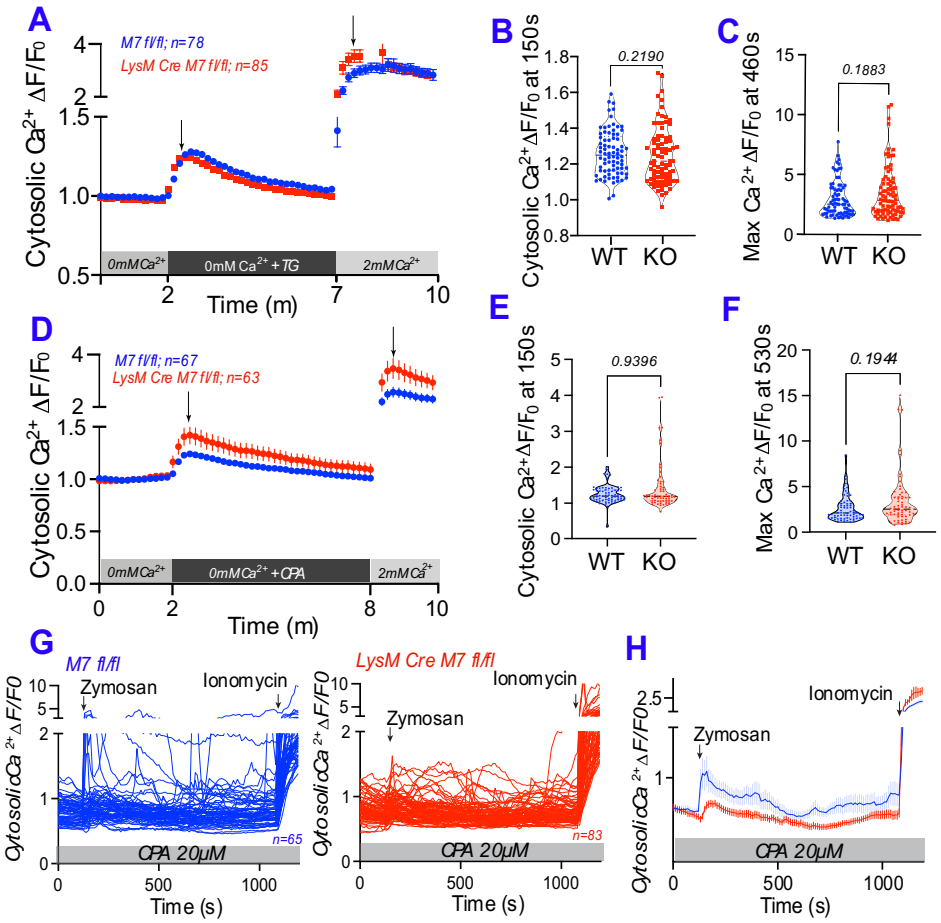
A
M7 fl/fl; n=78
LysM Cre M7 fl/fl; n=85
Cytosolic Ca2+ ΔF/F0
0mMCa2+
0mM Ca2+ + TG
2mMCa2+
Time (m)
B
0.2190
Cytosolic Ca2+ ΔF/F0 at 150s
WT KO
C
0.1883
Max Ca2+ ΔF/F0 at 460s
WT KO
D
M7 fl/fl; n=67
LysM Cre M7 fl/fl; n=63
Cytosolic Ca2+ ΔF/F0
0mMCa2+
0mMCa2+ + CPA
2mMCa2+
Time (m)
E
0.9396
Cytosolic Ca2+ ΔF/F0 at 150s
WT KO
F
0.1944
Max Ca2+ ΔF/F0 at 530s
WT KO
G
M7 fl/fl
LysM Cre M7 fl/fl
Zymosan
Ionomycin
Cytosolic Ca2+ ΔF/F0
CPA 20μM
n=65
n=83
Time (s)
H
Ionomycin
Zymosan
Cytosolic Ca2+ ΔF/F0
CPA 20μM
Time (s)

Figure 10. TRPM7 does not regulate SOCE in macrophages

(A) Average cytosolic Ca^{2+} in Fura-2-AM loaded *TRPM7fl/fl* (WT, blue, n=78) and *TRPM7$^{fl/fl}$ LysM-Cre* (KO red, n=85) BMDMs in a classical SOCE protocol. Recording was performed in Ringer's solution without Ca^{2+}. Thapsigargin (TG; 5 μM) was added at 2 min of recording (indicated by a dark box at x-axis). 2 mM Ca^{2+}-containing Ringer was added at the indicated time to measure the influx of extracellular Ca^{2+} upon store depletion.

(B) Peak cytosolic Ca^{2+} levels in response to 5 μM TG at 150 s from data shown in panel S4A (indicated by a first arrow in Fig S4A), in WT (blue, n=78) and KO (red, n=85) macrophages. Data represented as a violin plot with means outlined in black dashed line. P value derived from a two-tailed t test (Mann-Whitney).

(C) Peak cytosolic Ca^{2+} in response to 2 mM Ca^{2+} at 460 s (second arrow in Fig. S4A) in WT (blue, n=78) and KO (red, n=85). Data shown as described in panel S4B.

(D) Average cytosolic Ca^{2+} traces in CalBryte^{TM} 520-loaded WT (blue, n=67) and KO (red, n=63) BMDMs in response to CPA (20 μM). The SOCE protocol as described in panel S4A.

(E) Peak cytosolic Ca^{2+} levels in response to 20 μM CPA at 150 s (indicated by a first arrow in Fig. S4D) in WT (blue, n=67) and KO (red, n=63) macrophages. Data shown as described in panel S4B.

(F) Peak cytosolic Ca^{2+} responses to 2 mM Ca^{2+} at 530 s (indicated by a second arrow in Fig. S4D) in WT (blue, n=67) and KO (red, n=63) macrophages. Data shown as described in panel S4B.

(G) Individual cytosolic Ca^{2+} traces in Fura-2-AM loaded *TRPM7$^{fl/fl}$* (WT, blue, n=65) and *TRPM7$^{fl/fl}$ LysM-Cre* (KO red, n=83) BMDMs (pretreated with CPA, 20 μM) stimulated with zymosan.

(H) Average Ca^{2+} traces in Fura-2-AM loaded BMDMs from Fig. S4G for WT (blue, n=65) and KO (red, n=83) BMDMs.

Figure 11

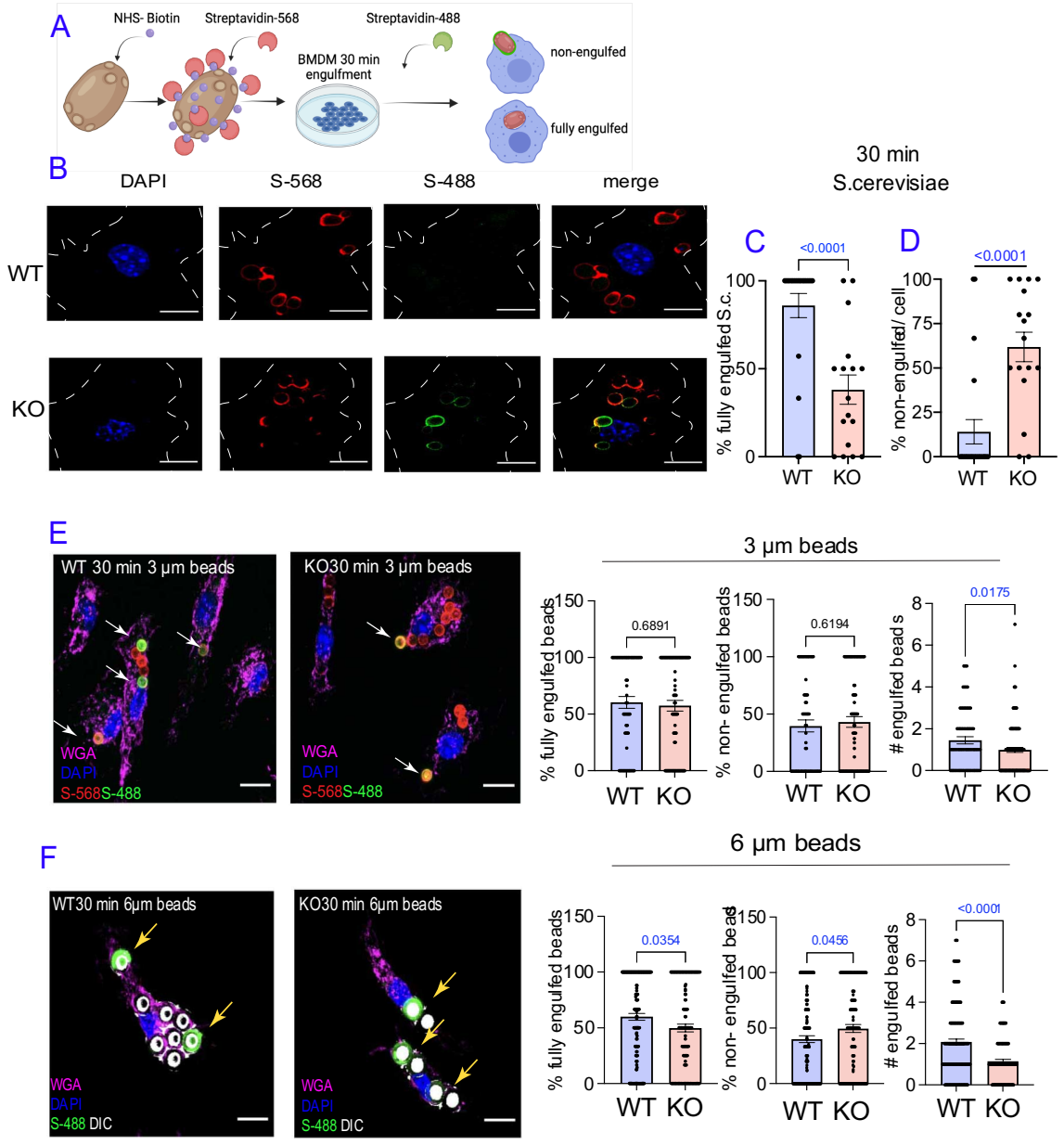
A
NHS- Biotin
Streptavidin-568
Streptavidin-488
BMDM 30 min engulfment
non-engulfed
fully engulfed
B
DAPI
S-568
S-488
merge
WT
KO
30 min S.cerevisiae
C
<0.0001
% fully engulfed S.c.
WT
KO
D
<0.0001
% non-engulfed/ cell
WT
KO
E
WT 30 min 3 µm beads
KO30 min 3 µm beads
WGA
DAPI
S-568S-488
3 µm beads
% fully engulfed beads
0.6891
% non- engulfed beads
0.6194
engulfed beads
0.0175
F
WT30 min 6µm beads
KO30 min 6µm beads
WGA
DAPI
S-488 DIC
6 µm beads
% fully engulfed beads
0.0354
% non- engulfed beads
0.0456
engulfed beads
<0.0001

Figure 11. TRPM7 regulates the formation and sealing of the phagosome

(A) A cartoon showing the experimental design to evaluate the completion of engulfment.

(B) Representative confocal images of *S. cerevisiae* engulfment at 30 min, for WT (upper panel) and KO (lower panel) macrophages. Single channels and the merged images are shown. Scale bar=10 μm.

(C) Quantification of the percentage of fully engulfed *S. cerevisiae* per cell at 30 min engulfment. Statistics performed with a two-tailed t test (Mann-Whitney). Error bars show SEM.

(D) Quantification of the percentage of partially engulfed (unsealed phagosomes) *S. cerevisiae* per cell at 30 min engulfment. Statistics performed with a two- tailed t test (Mann-Whitney). Error bars show SEM.

(E) Left panel: confocal images of primary WT (left) and KO (right) macrophages engulfing β-glucan conjugated 3 μm beads at 30 min. Right panel: quantification of the % fully-engulfed, % partially-engulfed and number (#) of engulfed beads are shown. Statistics performed with a two-tailed t test (Mann-Whitney). Error bars show SEM. WGA (wheat germ agglutinin) labels the cell membrane, DAPI (nuclear stain), streptavidin-568 labels all beads, streptavidin-488 (S-488) labels partially engulfed beads. Scale bar is 10 μm.

(F) Left panel: confocal images of primary WT (left) and KO (right)

macrophages engulfing β-glucan conjugated 6 μm beads at 30 min. Right panel: quantification of the % fully-engulfed, % partially-engulfed and number (#) of engulfed beads are shown. Data and statistics shown as in panel 5E.

Figure 12

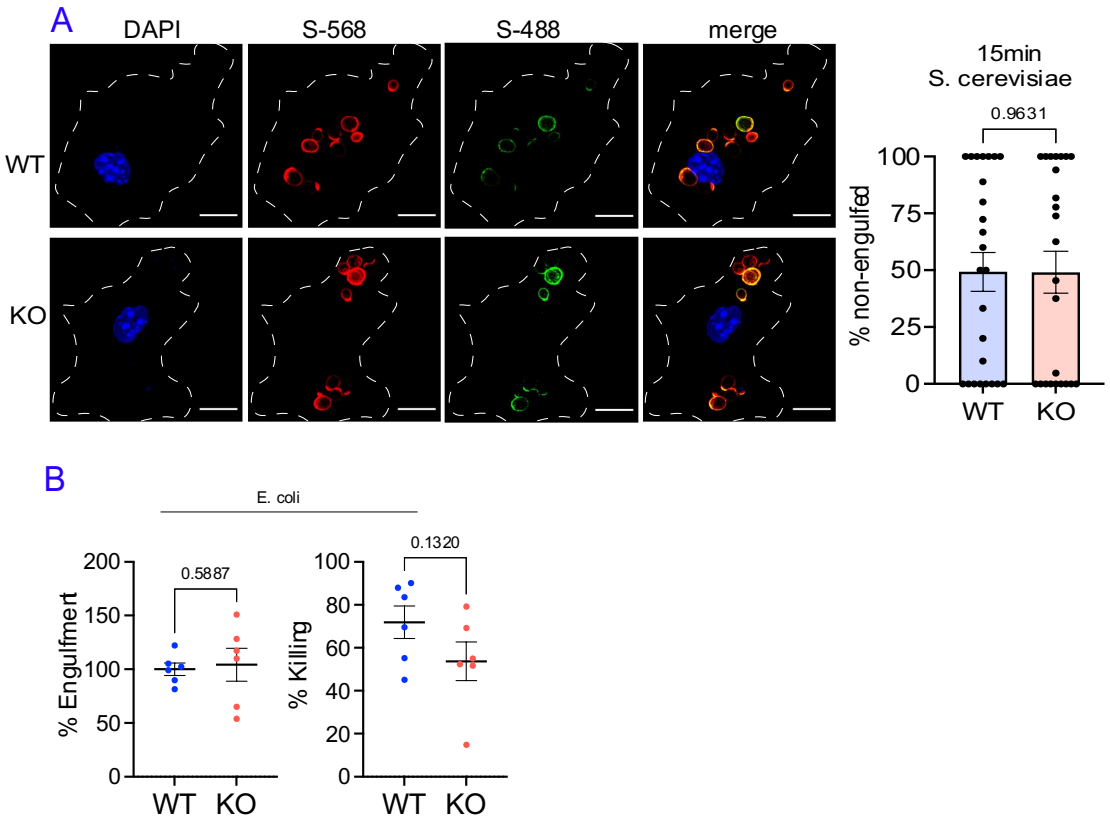
A
DAPI
S-568
S-488
merge
WT
KO
15min
S. cerevisiae
0.9631
% non-engulfed
100
75
50
25
0
WT
KO
B
E. coli
0.5887
% Engulfmert
200
150
100
50
0
WT
KO
0.1320
% Killing
100
80
60
40
20
0
WT
KO

Figure 12. Engulfment of E. coli is TRPM7-independent

(A) Left panel: representative confocal images show single channels and a merged image for WT (upper panel) and KO (lower panel) macrophages. Right panel: Quantification of the partially engulfed *S. cerevisiae* at 15 min for WT (blue) and KO (red) BMDMs. Error bars represent SEM. Statistics were performed with a two-tailed t test (Mann-Whitney). Scale bar=10 μm.

(B) Quantification of the *E. coli* engulfment and killing assay for WT (blue dots) and KO (red dots) BMDMs. Statistics performed with a two-tailed t test (Mann-Whitney).

Figure 13

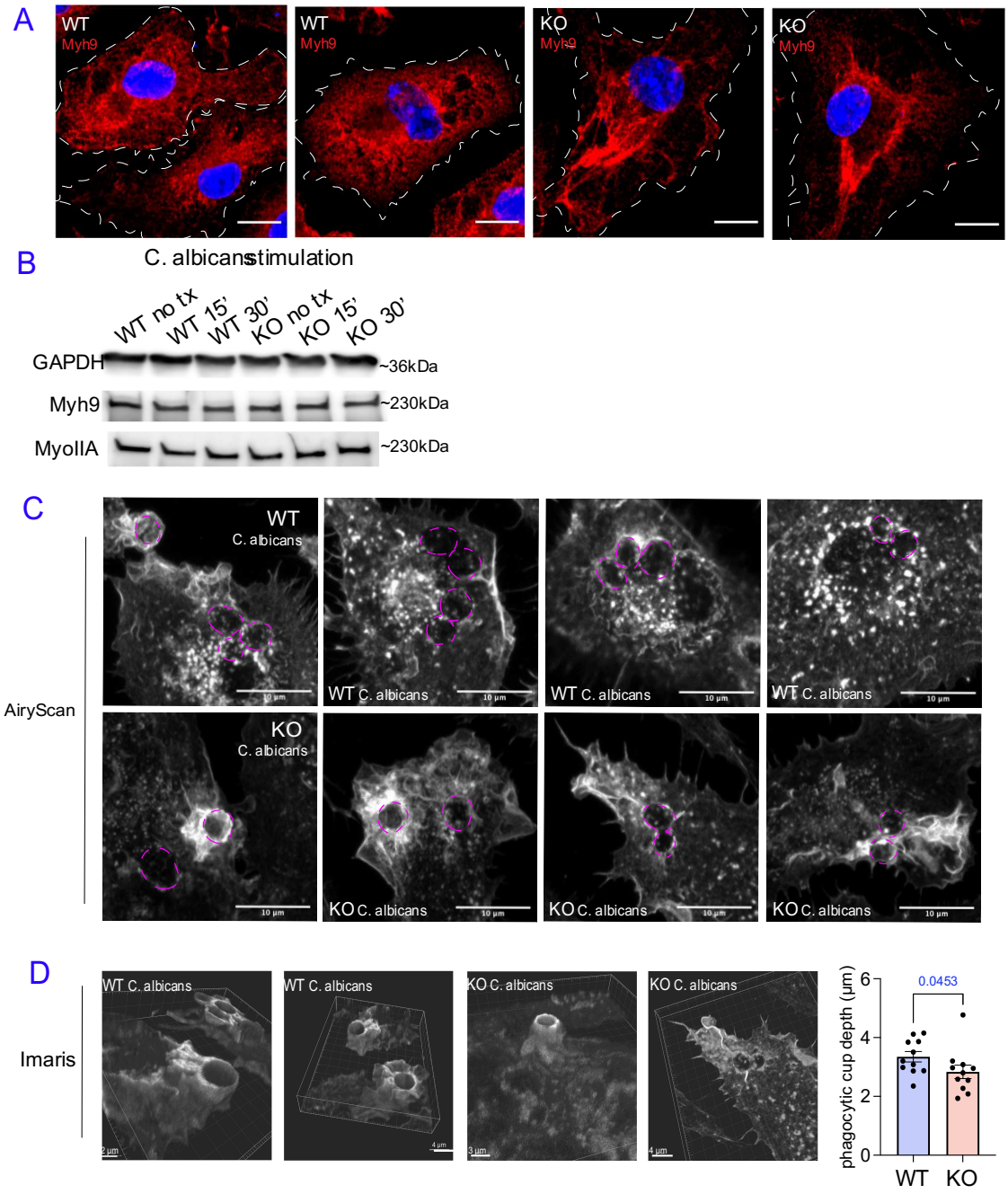
A
WT
Myh9
WT
Myh9
KO
Myh9
KO
Myh9
B
C. albicans stimulation
WT no tx
WT 15'
WT 30'
KO no tx
KO 15'
KO 30'
GAPDH
~36kDa
Myh9
~230kDa
MyoIIA
~230kDa
C
AiryScan
WT
C. albicans
WT C. albicans
WT C. albicans
WT C. albicans
KO
C. albicans
KO C. albicans
KO C. albicans
KO C. albicans
D
Imaris
WT C. albicans
WT C. albicans
KO C. albicans
KO C. albicans
phagocytic cup depth (µm)
0.0453
WT
KO

Figure 13. TRPM7-deficient macrophages display aberrant myosin IIA morphology, shallower phagocytic cups upon yeast engulfment and fewer podosome-like structures

(A) Representative maximal z-stack projection images of myosin IIA (Myh9, red) staining in WT and KO macrophages. DAPI stain in blue shows macrophage nuclei. Scale bar is 10 μm.

(B) Western blot of lysates from WT and KO macrophages stimulated with *C. albicans* for indicated times. GAPDH is a loading control. The blot probed for Myosin IIA (Myh9) expression with two different antibodies.

(C) Maximal z-stack projections of F-actin staining in WT (upper panels) and KO (lower panels) macrophages at 5 min incubation with *C. albicans* (outlined in purple-dashed circles). Scale bar=10 μm.

(D) Left: Imaris 3D rendition of z-stacks acquired from AiryScan confocal microscopy, showing phagocytic cup formation in WT (two left-most panels) and KO (two right-most panels) macrophages after 5 min incubation with *C. albicans*. Scale bars are outlined in each image. Right: quantification of the phagocytic cup depth in WT (blue) and KO (red) BMDMs. Statistics show a two-tailed t test (Mann-Whitney).

Methods

Mouse Strains

Trpm7$^{fl/fl}$ and *Trpm7*$^{fl/fl}$ (*LysM Cre*) mice were generated as described previously [64] and crossed to B6 background. Male and female mice 8-12 weeks of age were used for all experiments. Deletion of Trpm7 was confirmed via quantitative real-time PCR analysis and patch-clamp electrophysiology. All animals were bred and housed in line with the policies of the University of Virginia Institutional Animal Care and Use Committee (IACUC).

Mouse genotyping

Mice were tail clipped upon weaning and the tail samples were dissolved in DirectPCR Lysis Reagent (Viagen Biotech; #102-T), as outlined in the manufacturer's protocol. 1-2 µl of the crude lysate was used as the PCR template, performed with GoTaq Green (Promega; #M7122).

In vivo disseminated Candidiasis mouse model

Age-matched male and female mice were injected i.v. (tail vein) with $1x10^6$ previously washed (3x in 1xHBSS) and counted *C. albicans*, suspended in 0.9% saline solution. Mice were randomly assigned to experimental cages and allocated the appropriate injection by another experimenter. Mice were weighted before and

at regular time points post injection, as outlined in the figure panels and assessed for signs of distress (conjunctivitis, dull fur, hunching, nose bulge etc.). After general anesthesia with i.p.-administered Avertin (2, 2, 2- tribromoethanol, Sigma-Aldrich #T48402) the blood was collected with heparinized capillaries (Fisher ScientificTM #22-260950) and mice were euthanized.

Cell lines and cell culture

RAW267.4 (ATCC® TIB-71™) cell line were grown and maintained according to the ATCC guidelines, in a humified incubator at 37°C and 5% CO_2. Bone marrow-derived macrophages (BMDMs) were isolated and cultured as previously described[68]. In brief, bone marrow was extracted from murine femur and tibia via centrifugation. Red blood cells (RBCs) were lysed in ACK Lysis buffer and plated on petri dishes at 2-4x 10^6 cells/ plate in BMDM Media (RPMI 1640 + 10% FBS + 20% L929-conditioned media). Cells were differentiated for 7 days and the media was refreshed afterwards every 3 days. For experiments, BMDMs were used between day 7 to 14 after harvest.

Preparation of yeast cultures

Saccharomyces cerevisiae (strain sy1022 fy5) was provided to us as a gift from Jeff Smith Lab, UVA and *Candida albicans* was purchased from ThermoFisher

Scientific #R4601503. Yeast strains were streaked on YPD agar plates. When preparing cultures, a single colony was inoculated into previously-autoclaved 5ml YPD broth in a glass tube and grown overnight. The cultures were washed 3x in sterile 1xHBSS and counted based on their OD600, where OD600 of 1 equals $3x10^7$ yeast/ml. The yeast cultures were freshly grown for experiments and kept in the fridge.

Yeast killing/ engulfment assays

Killing assays were performed as described previously[68]. Briefly, primary macrophages or RAW264.7 cells were incubated with yeast strains *C. albicans* or *S. cerevisiae* for 30 min at 37°C (5% CO2). Cells were then washed 3x with HBSS to remove non-engulfed yeast and resuspended in BMDM media. One well/ sample was harvested and lysed at 30 min time point (T0) in sterile, distilled water for 30 min with shaking. Each well was serially diluted and plated on YPD agar plates. The T2 time point wells were harvested at indicated time, usually at 6h and lysed as before. The % yeast killing was calculated by the formula 100%-(T2/T0)x100. For engulfment assays only T0 samples were used with appropriate treatments. For biotinylation of *S. cerevisiae* two protocols were adapted[90,105]. Briefly, *S. cerevisiae* was subjected to biotinylation in 1 mg/ml EZ-LinkTM Sulfo-NHS-SS-Biotin (Thermo Scientific #21331) for 1h at RT with rotation. Streptavidin

conjugated to either AlexaFluor™-488 (ThemoFisher #S32354) or -568 (ThermoFisher #S11226) was added to triple washed biotinylated yeast and again incubated for 1h at RT in dark with rotation.

Bacterial killing/ gentamycin protection assay

WT and KO BMDMs were seeded in an antibiotic-free media (RPMI1640 +10% FBS) and infected with freshly grown overnight bacterial culture at a MOI1. To assess engulfment (T0), bacteria were added to BMDMs and incubated for 30 min (37°C, 5% CO_2). Bacteria-containing wells were washed off and gentamycin (100 µg/ml)-containing media was added for 30 min to T0 wells (at 37°C, 5% CO_2), then cells were lysed and plated on LB-agar plates. The killing was assessed at 1h, after which time the media was replaced with gentamycin-containing media, as before, followed by cell lysis and plating lysates on LB agar in serial dilutions.

Transwell migration assay

The transwell polycarbonate membrane cell culture inserts (#CLS3422; Cornig) were used. *C. albicans* were prepared from a fresh overnight culture, as outlined above, and placed in the lower chamber compartment suspended in BMDM media. BMDMS were freshly seeded on the membrane, allowed to adhere for 30 min and then incubated for 6h. Control samples for basal migration assessment had no *C.*

albicans present in the lower chamber. At the end of experiment, the non-migrated cells, remaining on the top of the membrane were gently scraped off with a clean cotton swab, the membranes were rinsed with PBS and fixed (4% PFA in PBS), stained and mounted on glass slides using ProLongTM Gold antifade reagent with DAPI (#P36935; Invitrogen). Migration was quantified using light microscope at 40x magnification. The 10 ROIs were chosen randomly and averaged for each sample.

Phagosomal sealing experiments

For bead biotinylation a previously published protocol was adapted[90]. Briefly, 3 µm (#19118-2; Polysciences) or 6 µm (#17145-4; Polysciences) amine-conjugated beads were washed in anhydrous DMSO (#276855; Sigma-Aldrich) using 0.45 µm PTFE membrane columns (#UFC30LH25; Millipore). Amine groups were activated by 0.5 M CDI (#115533; Sigma-Aldrich) in DMSO and the beads were incubated with shaking for 1h at RT. 10 mM β-glucan (#346210; EMD Millipore) was dissolved in DMSO and added to the beads for 1h incubation at RT. Beads were washed using the PTFE filters and resuspended in 1x PBS or further biotinylated with 6 mg/ml EZ-linkTM Sulfo-NHS-SS-biotin (#21331; ThermoFisher). Streptavidin conjugated to either AlexaFluor-488 or -568 was then added for 1h RT incubation, as before. Phenol-sulfuric acid assay was performed to validate the

conjugation of β-glucan and measure the carbohydrate content. Further validation via RT-qPCR measurement of IL-1β transcript levels was performed on RAW267.4 cells incubated with 1:1 ratio of 3 μm- β-glucan conjugated beads for 3h.

Patch Clamp Electrophysiology

All electrophysiology experiments were conducted at RT with an Axopatch 200B amplifier (Molecular Devices, Sunnyvale, CA). To measure TRPM7 currents (I_{TRPM7}) in BMDMs or RAW264.7 cells (WC-PCE configuration), macrophages were freshly seeded onto the glass coverslips and allowed to adhere. The composition of the WC-PCE extracellular bath solution was (in mM): 140 Na-CH_3O_3S, 5 Cs-gluconate, 2.5 $CaCl_2$, 10 HEPES, (adjusted to pH 7.4 with osmolality 285 mOsm/kg). The pipette solution contained (in mM): 115 Cs-gluconate, 3 NaCl, 0.75 $CaCl_2$, 1.8 Cs_4-BAPTA, 2 Na_2ATP, 10 HEDTA, 10 HEPES (adjusted to pH 7.4 with osmolality 273 mOsm/kg). Inhibition of ITRPM7 was achieved by using FTY720 (5 μM). For perforated- patch (PPCE) configuration 100 μg/ml of freshly prepared Nystatin was added in the pipette. Extracellular bath contained (in mM): 140 NaCl, 5 KCl, 1 $MgCl_2$, 2 $CaCl_2$, 10 D-glucose, 10 HEPES (adjusted to pH 7.4 with osmolality 310 mOsm/kg). The PPCE pipette solution contained (in mM): 120 Cs-methanesulfonate (Cs-CH_3O_3S), 30 CsCl, 1 $MgCl_2$, 0.2 $CaCl_2$, 1 EGTA, 10 HEPES, 100 μg/ml Nystatin (pH=7.4). Recordings were

obtained with holding potential of 0 mV, employing a voltage ramp from -100 mV to +100 mV for 400 ms; filtering the signaling at 5 kHz and sampling at 10 kHz. Zymosan particles and *S. cerevisiae* extract were prepared in PPCE bath solution.

Immunocytochemistry

Cells were seeded on glass coverslips prior to experiments. Coverslips were washed in 1 x PBS prior to fixing with 4% PFA (in PBS) for 20 min at RT. Coverslips were washed 3x in 1 x PBS prior to blocking at RT for 1h in blocking buffer (5% donkey serum, 1% BSA, 0.1% fish gelatin, 0.1% Triton X-100, and 0.05% Tween-20 in PBS) or BlockAid™ Blocking Solution (#B10710). Incubation with primary antibodies was performed overnight at 4°C, and they were diluted in blocking solution at concentrations indicated by the manufacturer. Post- incubation, samples were washed 3X in 1xPBS and incubated with a secondary antibody, conjugated to a fluorophore, for 90 min at RT (in the dark), followed by 3x wash in 1xPBS. For F-actin staining, cells were prepared with CellMask™ Actin (Invitrogen; #A57243 or #A57245), as recommended by the manufacturer. Coverslips were then mounted on glass slides using ProLong™ Gold Antifade #P36930, allowed to cure overnight, and usually imaged within 48 hours. Confocal microscopy imaging was performed with Zeiss LSM880 with AiryScan and analyzed using Fiji [106].

Western blot and cellular fractionation experiments

Whole-cell lysates were prepared by harvesting and incubating cells for 30 min on ice, in a desired volume of Lysis Buffer (300mM NaCl, 1% NP-4, 50mM Tris-HCl, 0.5% sodium deoxycholate, 0.1% SDS, pH= 7.4). Soluble proteins were harvested by centrifugation at 20,000 xg for 15 min in a tabletop centrifuge (4°C). Total protein concentration was assessed by a BCA Assay (ThermoFisher; #23225). Supernatants were mixed with 5X Laemmli Buffer (0.3M Tris-H-Cl, 10% SDS, 50% glycerol, 25% β-mercaptoethanol, 0.05% bromophenol- blue) and boiled at 95°C for 10 min. Samples were loaded onto 4–20% Mini-PROTEAN® TGX™ Precast Protein Gels (BioRad; #4561096) and separated by electrophoresis (150V, 90 min in SDS-PAGE buffer). Cellular fractionation was performed as before (Schappe et al., 2018). Briefly, at least 2 x 10^6 macrophages were seeded in equal numbers the day before fractionation experiments. Cells were carefully collected on ice after treatments in ice- cold PBS, pelleted and resuspended in cytoplasmic fraction buffer (CFB; 60 mM KCl, 10 mM HEPES, 1 mM EDTA, 0.075% NP-40), followed by 5 min incubation on ice. Cells were then pelleted for 5min at 1,200 xg at 4°C. Supernatant was collected in a new tube and labeled as cytoplasmic fraction. Pellet was profusely washed in a wash buffer (CFB without NP-40) and lysed in a nuclear fraction buffer (NFB; 420mM NaCl, 20 mM Tris-HCl, 1.5 mM $MgCl_2$, 0.2 mM EDTA) on ice for 1 min with regular vortexing. Nuclear fraction was then centrifuged at 20,000 xg for 15 min and supernatants were collected and labeled

as nuclear fractions. Both fractions received 5x Laemmli buffer to a final 1x concentration and were run on protein gel, as escribed above. Protein transfer onto a PVDF membrane was performed with a Trans-Blot Turbo Transfer system (BioRad).

qRT-PCR gene expression

Macrophages were seeded onto a 12-well plate at a density of 0.5x 10^6 and cultured overnight. Next day they underwent stimulation as outlined in the figure panels. When using pharmacological treatment, the appropriate drug was added 10 min prior stimulation with fungal particles in complete media and then together with the fungal particles. RNA isolation was performed using RNeasy Plus Kit (Qiagen#74134) and cDNA synthesis was performed using GoScriptTM Reverse Transcriptase Kit (Promega #A5001). qRT-PCR reactions were performed using SensiFast SYBR no-rox kit (BIO-98020).

Ca^{2+} Imaging

BMDMs were plated on glass coverslips and loaded with Fura-2-AM or Calbryte™ 520-AM for 45 min at RT with gentle rocking. Imaging was performed in Ringer Solution ([in mM] 155 NaCl, 4.5 KCl, 2 $CaCl_2$, 1 $MgCl_2$, 5 HEPES, 10 D-glucose, pH 7.4) or in Ca^{2+}-free Ringer Solution (155 NaCl, 4.5 KCl, 1 $MgCl_2$, 5 HEPES, 10

D-glucose, pH 7.4) at RT. Zymosan/ fungal particles (at 1:1 ratio) and ionomycin (2 μM) were added directly to the imaging chamber. Fura-2-AM measurements were performed as described previously[64] with stimulations as indicated in the figure legend. Image acquisition was performed using Zeiss Axio Observer microscope with a DG4 Illuminator (Sutter Instruments, Canada) and ORCA-Flash 4.0 V2 CMOS camera (Hammamatsu). Software for image acquisition was SlideBook 6 software (3i).

Tissue processing and immunohistochemistry

Mouse tissues processing, H&E and PAS staining were performed at the University of Virginia Research Histology Core (Sheri VanHoose, MLT [NCA]). The Immunocytochemistry with CD45 (#550539, BD Biosciences) and Ly-6G (#12762, Biolegend) antibodies, together with slide scanning were performed at the University of Virginia Biorepository and Tissue Research Facility (BTRF; Pat Pramoonjago, PhD).

Statistics

The data analysis was performed with Excel (Microsoft), GraphPad Prism 9.0 (GraphPad Software) and Origin Pro 9.1.0 (Origin Lab), plotted with GraphPad and Origin Pro. Data was preferably presented as individual data points for each

independent sample and plotted with means and error bars, as described in figure legends. The sample size and p values are indicated in figure legends, p values less than 0.05 were considered statistically significant.

Author Contributions

Conception and research design: MES, BND; Experimental execution: MES performed the majority of the experiments with the help from JJJ and PVS, Electrophysiological recordings were performed by EJS, WHI, GWB; Data analysis: MES, EJS, JJJ, GWB, WHI, PVS; Technical assistance: EJS, JK; Manuscript writing: MES, BND with input from PVS, GWB and Catherine Doyle; Project Administration and funding: BND (GM108989). Conceptual advice and comments received throughout the study from all lab members.

CHAPTER TWO TABLES

Table 1. Reagents used in the study

Reagent or resource	Source	Identifier
Cell Lines		
RAW267.4	ATCC®	TIB-71™
Yeast Strains		
Candida albicans	ThermoFisher Scientific	R4601503
Saccharomyces Cerevisiae (sy1022 fy5)	Smith Lab, UVA	N/A
Antibodies/Dyes		
Anti-mouse CD45 (30-F11)	BD Biosciences	550539
Anti-mouse Ly-6G (1A8) Rt Ab	BioLegend	12762
Anti-mouse LSD1 (C69G12) Rb mAb	Cell Signaling	2184
Anti-mouse GAPDH (D16H11) Rb mAb	Cell Signaling	5174
Anti-mouse NFκB (D14E12) Rb mAb	Cell Signaling	8242
Anti-mouse IRF3 (D83B9) Rb mAb	Cell Signaling	4302
Anti-mouse IRF5 (10T1) Ms mAb	Abcam	ab33478
Anti-mouse STAT1 polyclonal Rb Ab	Cell Signaling	9172
Anti-mouse Myosin IIA polyclonal Rb Ab	Cell Signaling	3403
Anti-mouse Myh9 polyclonal Rb Ab	Proteintech	11128-1-AP
Phalloidin-AlexaFlour647	Invitrogen	A22287

Wheat Germ Agglutinin-AlexaFluor633	Invitrogen	W21404
CellMask™ Actin	Invitrogen	A57243 or A57245
CalBryte™520	AAT Bioquest	20650
Fura-2-AM	Invitrogen	F1221
ProLong™Gold Antifade	Invitrogen	P36930
Streptavidin-AlexaFlour-488	Invitrogen	S32354
Streptavidin-AlexaFlour-568	Invitrogen	S11226

Reagents		
Polybead® Amino Microspheres 3.00µm	Polysciences	17145-5
Polybead® Amino Microspheres 6.00µm	Polysciences	19118-2
β-Glucan, Saccharomyces cerevisiae	Milipore Sigma	346210-25MG
EZ-Link™ Sulfo-NHS-SS-Biotin	Thermo Scientific	21331
CyQuant™ LDH Cytotoxicity Assay	Invitrogen	C20300
BlockAid™ blocking solution	Invotrogen	B10710
Fingolimod (FTY720)	Cayman Chemical	10006292
FTY720 Phosphate (FTY720p)	Cayman Chemical	10008639
AAL149	Lynch Lab, UVA	N/A
VPC01091.2p	Lynch Lab, UVA	N/A
ER 27319 maleate	Tocris	2471
U 73122	Tocris	1268

Thapsigargin	Invitrogen	T7458
Cyclopiazonic acid	Cayman Chemical	11326
Ionomycin	Thermo Fisher	I24222
Nystatin	Fisher Scientific	BP2949
2,2,2- tribromoethanol	Sigma-Aldrich	T48402
Consumables		
Fisherbrand™ Color-Coded Capillary Tubes (Heparinized)	Fisher Scientific	22-260950
Transwell® polycarbonate membrane cell culture inserts	Corning®	CLS3422
Ultrafree-MC Centrifugal Filter	Millipore Sigma	UFC30LH25
RNeasy Plus Mini Kit	Qiagen	74134
GoScript™ Reverse Transcriptase	Promega	A5004
SensiFast SYBR no-rox kit	Bioline	BIO-98020
Genotyping primers		
LysM-Cre: WT: 5'-TTACAGTCGGCCAGGCTGAC-3'	IDT	N/A
Common: 5'-CTTGGGCTGCCAGAATTTCTC-3'	IDT	N/A
Mutant: 5'-CCCAGAAATGCCAGATTACG-3'	IDT	N/A
$TRPM7^{fl/fl}$: F: 5'-GAACTACAAAGCCATCTCTCCTCTG-3'	IDT	N/A

R: 5'-TTCAGCCGTCCCATCCACATATC-3'	IDT	N/A
RT-qPCR primers		
β2M-F 5'-GGCCTGTATGCTATCCAGAA-3' *β2M*-R 5'-GAAAGACCAGTCCTTGCTGA-3'	IDT	N/A
Trpm7-F 5'-AGCAGTATTCCAATGATTTTGGC-3' *Trpm7*-R 5'-TCATAGCCATCGTTTCATCCTGT-3'	IDT	N/A
Il-6-F 5'-TAGTCCTTCCTACCCCAATTTCC-3' *Il-6*-R 5'-TTGGTCCTTAGCCACTCCTTC-3'	IDT	N/A
Il1- β-F 5'-GCAACTGTTCCTGAACTCAACT-3' *Il1- β*-R 5'-ATCTTTTGGGGTCCGTCAACT-3'	IDT	N/A
Tnf-α-F 5'-CCCTCACACTCAGATCATCTTCT-3' *Tnf-α*-R 5'-GCTACGACGTGGGCTACAG-3'	IDT	N/A
Nos2-F 5'-GTTCTCAGCCCAACAATACAAGA-3' *Nos2*-R 5'-GTGGACGGGTCGATGTCAC-3'	IDT	N/A
Cxcl1-F 5'-CCAAACCGAAGTCATAGCCAC-3' *Cxcl1*-R 5'-TTCTCCGTTACTTGGGGACAC-3'	IDT	N/A
Ccl4-F 5'-TCTGTGCAAACCTAACCCCG-3' *Ccl4*-R 5'-GGGTCAGAGCCCATTGGTG-3'	IDT	N/A

CHAPTER THREE: Targeting the ion channel TRPM7 promotes the thymic development of regulatory T cells by promoting IL-2 signaling

Disclaimer: The contents of Chapter Two appear as published in *Science Signaling*: *Mendu, S. K., *Stremska, M. E., Schappe, M. S., Moser, E. K., Krupa, J. K., Rogers J. S., Stipes, E. J., Parker, C. A., Braciale, T. J., Perry, J. S. A., Desai, B. N., Targeting the ion channel TRPM7 promotes the thymic development of regulatory T cells by promoting IL-2 signaling. *Sci Signal* **13**, eabb0619 (2020). **These authors contributed equally to this work.* Minor alterations may have been applied for clarity and formatting requirements.

Abstract

The thymic development of regulatory T (Treg) cells, crucial suppressors of the responses of effector T (Teff) cells, is governed by the transcription factor FOXP3. Despite the clinical importance of Treg cells, there is a dearth of drug-gable molecular targets capable of increasing their numbers in vivo. We found that inhibiting the function of the TRPM7 chanzyme (ion channel and enzyme) potentiated the thymic development of Treg cells in mice and led to a substantially higher frequency of functional Treg cells in the periphery. In addition, TRPM7-deficient mice were resistant to T cell–driven hepatitis. Deletion of Trpm7 and inhibition of TRPM7 channel activity by the FDA-approved drug FTY720 increased the sensitivity of T cells to the cytokine interleukin-2 (IL-2) through a positive feed-forward loop involving increased expression of the IL-2 receptor α-subunit and activation of the transcriptional regulator STAT5. Enhanced IL-2 signaling increased the expression of Foxp3 in thymocytes and promoted thymic Treg (tTreg) cell development. Thus, these data indicate that inhibiting TRPM7 activity increases Treg cell numbers, suggesting that it may be a therapeutic target to promote immune tolerance.

Graphical Abstract

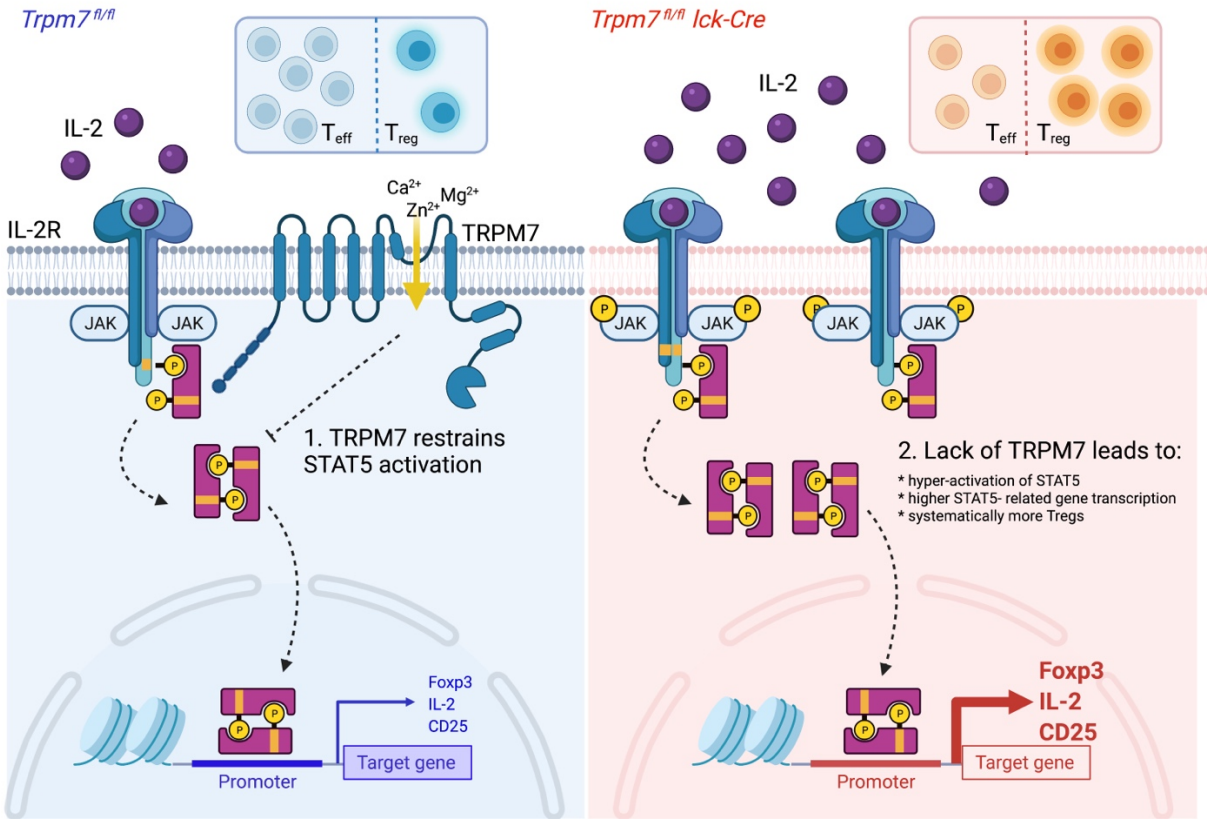

Introduction

The immune system has the ability to control the intensity, duration, and scope of inflammatory processes through an elaborate array of checks and balances[107]. Regulatory T (T_{reg}) cells play a salient immunosuppressive role to balance the destructive potential of effector T (T_{eff}) cells[108]. Although Treg cells develop from the same thymocyte precursors as do the Teff cells, the distinct Treg cell lineage is specified through the expression and maintenance of the forkhead box protein P3 (FOXP3) transcription factor[109,110]. Consequently, the genetic loss of FOXP3 in humans and mice prevents the development of Treg cells and breaks self-tolerance[110–114]. Interleukin-2 (IL-2) signaling plays a decisive role in immune tolerance by regulating the development, maintenance, and function of Treg cells[115–119]. The key transcription factor responsible for Foxp3 expression, downstream of IL-2 signaling, is STAT5 (signal transducer and activator of transcription 5)[120,121]. Accordingly, ectopic expression of a constitutively active STAT5 variant is sufficient to divert the fate of developing thymocytes toward the Treg cell lineage[118]. The thymic development of Treg cells is thought to occur through a twostep process[119,122]. First, T cell receptor (TCR) signaling increases the abundance of the IL-2 receptor α-subunit (IL-2Rα; also known as CD25) and other components of the IL-2 signaling pathway, increasing the sensitivity of the cells to IL-2. Second, IL-2–mediated signals increase Foxp3 transcription in a

STAT5-dependent manner to finalize the commitment of these $CD25^+$ progenitors to the T_{reg} cell lineage. However, a study indicated an additional developmental program involving $Foxp3^{lo}$ T_{reg} progenitor cells[119]. Identifying previously uncharacterized "druggable" components in this pathway may enable the pharmacological manipulation of Foxp3 expression and T_{reg} cell numbers *in vivo*. The National Center for Advancing Translational Sciences (NCATS) has identified a druggable genome of ~3000 human genes encoding predominantly three key protein families that are ideal for drug development: nonolfactory GPCRs (G protein–coupled receptors), ion channels, and protein kinases[123–125]. The transient receptor potential (TRP) channels, a 28-member superfamily of ion channels that constitute an exciting class of drug targets, are included in the ion channel family[126]. Cation-selective TRP channels mediate context-specific electrical signaling in all organ systems, but the functions of the specific TRP channels prevalent in the immune system remain largely mysterious and thus unexploited for immuno-modulation. Three members of the TRP superfamily—TRPM2, TRPM6, and TRPM7—have ion channel activity and an additional enzyme activity. TRPM7, an ion channel permeable to cations such as Ca^{2+}, Na+, Zn^{2+}, and Mg^{2+}, contains a C-terminal serine-threonine kinase domain[127–129] and is highly expressed in T cells[33]. Hematopoietic cells exhibit robust TRPM7 currents (I_{TRPM7} or simply I_{M7}), and TRPM7 is an important regulator of both innate and adaptive immunity[33,39,47,130]. Previously, we generated *Trpm7$^{fl/fl}$(Lck Cre)* mice to delete

Trpm7 selectively in the T cell lineage[33]. In these mice, thymocyte development is impaired, resulting in a substantial accumulation of $CD4^{-}CD8^{-}$ [double-negative 3 (DN3); $CD44^{-}CD25^{+}$] thymocytes and reduced thymic cellularity[33]. The developmental block is partial, and the residual egress of mature $CD4^{+}$ and $CD8^{+}$ T cells populates the peripheral lymphoid organs normally. Because $Trpm7^{-/-}$ T cells are also resistant to apoptosis[39], we expected to see a lymphoproliferative phenotype and autoimmunity[131]. Unexpectedly, the $Trpm7^{fl/fl}$*(Lck Cre)* mice (hereafter referred to as "KO" mice) exhibit T cell lymphopenia[33] and autoimmunity is greatly delayed and mild in its manifestation[39]. These observations suggest that deletion of TRPM7 in T cells promotes immunosuppression through an undefined mechanism. Here, we studied a mouse model of autoimmune hepatitis (AIH), a T cell–driven inflammatory disease that often leads to liver cirrhosis, cancer, and death[132]. In mice, AIH can be modeled by intravenous injection of concanavalin A (Con A), which results in an acute, dose-dependent liver inflammation that is driven by the activity of $CD4^{+}$ T cells[133]. We showed that when *Trpm7* was deleted in T cells, the mice were resistant to Con A–induced hepatitis. $Trpm7^{-/-}$ T cells were activated normally and showed only modest differences in their cytokine outputs, but we found that deletion of *Trpm7* in the developing thymocytes potentiated the thymic development of T_{reg} cells, leading to a substantially higher frequency of functional Treg cells in the periphery. The deletion of *Trpm7* or pharmacological inhibition of TRPM7 increased FOXP3 protein abundance in developing

thymocytes, steering a larger percentage toward the T_{reg} cell lineage. Bone marrow (BM) transplant experiments indicated that the underlying mechanism was non–cell autonomous and, in part, depended on increased IL-2 production by the *Trpm7*$^{-/-}$ thymocytes. Thus, we have found that blocking TRPM7 channel activity increased IL-2–dependent thymic T_{reg} (tT_{reg}) development. Through these studies, TRPM7 has emerged as a pharmacological target to potentially increase Treg cell numbers in vivo and promote immunological tolerance.

Results

Deletion of Trpm7 in T cells protects mice from Con A-induced experimental lethal hepatitis

AIH[132], which is modeled by injecting mice intravenously with Con A, results in acute T cell–dependent liver inflammation and lethality[133]. We administered Con A and assessed the development of hepatitis over the course of 24 hours (Fig. 14A). Kaplan-Meier survival analysis of *Trpm7*$^{fl/fl}$ [wild type (WT)] and KO mice showed that 50% of the WT mice succumbed within 24 hours (Fig. 14B), whereas the KO mice were resistant to Con A–induced death. To assess liver damage, we measured the concentration of the liver enzyme alanine transaminase (ALT) in the serum 24 hours after Con A injection. The mean serum ALT activity in the WT mice was increased modestly in the surviving mice (Fig. 14C), which is likely an

underestimate because it was not possible to measure the ALT concentration in the dead mice. Through histological analysis of liver sections, perivascular inflammation was readily evident in Con A–treated WT mice but not in Con A–treated KO mice (Fig. 14D). We also measured the relative changes in the expression of genes encoding inflammatory cytokines in homogenized liver tissue of the surviving mice 24 hours after Con A injections. In the WT mice, the relative abundance of mRNAs for inflammatory cytokines increased substantially in the Con A–injected mice when compared to saline- injected controls (Fig. 14E). The expression of *Il2*, *Il1b*, and *Il6* was also increased but to a lesser extent. In contrast to WT mice, the increase in inflammatory cytokine gene expression was significantly blunted even in the surviving Con A–injected KO mice. The trend was reversed in the case of *Tgfb1*, which encodes the anti-inflammatory cytokine transforming growth factor–β (TGF-β), relative to the saline- treated controls. Together, these results suggest that the TRPM7 in T cells is important for the onset of acute liver inflammation induced by Con A. Because the deletion of *Trpm7* in T cells was considerably protective in Con A–induced hepatitis, we tested the hypothesis that TRPM7 was essential for T cell activation. The idea that TRPM7 regulates T cell activation has been suggested previously from experiments with T cell lines, albeit without the benefit of gene- targeted mice[134].

KO T_{eff} cells exhibit normal activation and proliferation but have defects in cytokine production

T cell activation is initiated after the stimulation of the TCR complex in conjunction with a costimulatory signal[135]. To evaluate T cell activation, we stimulated freshly isolated splenic $CD4^+CD25^-$ T cells, referred to as Teff cells, with either Con A or a mixture of anti-CD3 and anti-CD28 antibodies. The cells were analyzed for the cell surface appearance of activation markers by flow cytometry and for cytokine secretion by enzyme- linked immunosorbent assay (ELISA) (Fig. 15A). After 48 hours of stimulation, both WT and *Trpm7*$^{-/-}$ (KO) Teff cells showed similar increases in CD69 abundance (Fig. 15B). The increase in the cell surface abundance of CD25 was considerably higher in cells from the KO mice than in those from the WT mice (Fig. 15C). T cell activation results in increased cell size, which is conveniently measured by the forward scatter (FSC) parameter in flow cytometry. We found that both WT and KO T_{eff} cells increased in size comparably (Fig. 15D). After 72 hours of activation, we measured T cell proliferation using the carboxyfluorescein diacetate succinimidyl ester (CFSE)–labeling method, which measures the progressive dilution of CFSE during cell divisions. Both WT and KO T_{eff} cells proliferated comparably in response to stimulation by the anti-CD3 and anti-CD28 antibody cocktail (Fig. 15E). Next, on the basis of another study, we considered the possibility that TRPM7 regulates Orai-mediated Ca^{2+} influx after TCR stimulation[136]. We performed live- cell imaging of thymocytes stained with

Fura-2 AM upon TCR activation with an anti-CD3e antibody (Fig. 15F). We observed that the deletion of TRPM7 changed the kinetics, but not the amplitude, of store-operated Ca^{2+} entry (SOCE), as determined by peak $[Ca^{2+}]i$ and the area under the curve. We then wondered whether T cell migration was affected by the absence of TRPM7. We compared the transwell migration of WT and KO T cells in response to chemotactic factors produced by activated macrophages. The KO T cells migrated normally through the membrane (Fig. 16A). Because a major function of activated $CD4^+$ T cells is the secretion of cytokines that orchestrate inflammation, we measured the concentrations of various inflammatory cytokines in the culture medium of the T cells 72 hours after activation. After activation with Con A, the KO T cells secreted significantly greater amounts of IL-4 but reduced amounts of IL-3 and IL-6 (Fig. 15G). When T cells were activated with a mixture of anti-CD3 and anti-CD28 antibodies, the KO T cells consistently secreted increased amounts of IL-2, IL-4, IL-5, and IL-6 when compared to the WT T cells (Fig. 15H). Note that the KO T cells also secreted increased amounts of the anti- inflammatory cytokine IL-10, which was due to the increased expression of *Il10* (Fig. 16B). These results suggest that KO T_{eff} cells became activated and proliferated normally but had a different cytokine secretion profile to that of WT T_{eff} cells. This likely contributed to the resistance to Con A–induced lethal hepatitis but may not constitute a full explanation. In search for additional explanations, we characterized the composition of hematopoietic infiltration in the livers of Con A–

injected mice.

The infiltration of T_{reg} cells is increased in the livers of Con A–treated KO mice

The liver constitutes a unique immunological environment, housing a large number and diversity of hematopoietic cells[137]. To quantify the composition of these cells by flow cytometry, we analyzed single-cell suspensions isolated from freshly excised livers and also evaluated liver sections by immunohistochemistry and scanning electron microscopy (SEM) (Fig. 17A). On the basis of the cell surface staining of CD45, a marker of hematopoietic cells, the livers of saline- injected WT and KO mice contained an equivalent proportion of hematopoietic cells (~40%), which nearly doubled (~80%) 24 hours after Con A injections in both WT and KO mice (Fig. 17, B and C). Therefore, there was no significant difference between the WT and KO mice in terms of overall infiltration of hematopoietic cells after injection with Con A. Because $CD4^+$ T cells are the key mediators of Con A–induced lethality[133], we assessed the proportion of liver- infiltrating $CD4^+$ T cells. The liver-resident $CD4^+$ T cell population was readily detectable in saline-injected mice (Fig. 17, D and E), and the proportion of $CD4^+$ T cells changed slightly upon Con A injection. The percentage of $FOXP3^+$ T_{reg} cells was also similar in the livers of saline-injected WT and KO mice (Fig. 17, F and G; see Fig. 18 for gating strategy). The T_{reg} cell proportion became significantly increased in Con A–treated KO mice

relative to that in their WT counterparts (Fig. 17, F and G). Because FOXP3$^+$ T_{reg} cells are highly immunosuppressive, these data suggest that the increased frequency of T_{reg} cells in the KO mice contributed to the protection of these mice from Con A-induced liver inflammation. Immuno-fluorescence microscopy of liver sections suggested that there were increased numbers of CD4$^+$ T cells in the Con A–injected WT mice but that substantially fewer cells were detectable in the livers of the Con A–injected KO mice (Fig. 17H). Analysis of the liver vasculature by SEM (Fig. 17I) revealed the presence of endothelium-adhesive immune cells in the livers of Con A–injected WT mice, but these were less evident in the Con A–injected KO mice. Together, these results led us to hypothesize that the deletion of *Trpm7* in T cells results in a significantly increased frequency of T_{reg} cells in the periphery. The increase in the T_{reg}:T_{eff} ratio may be but one important cause of overall immunosuppression, manifesting in this study as an insensitivity to Con A–induced liver inflammation. To gain further insight into the origin of the imbalance in the T_{reg}:T_{eff} ratio, we surveyed the T_{reg} cell frequency in the thymus and spleen.

KO mice have a higher frequency of CD4$^+$Foxp$^+$Treg cells in the thymus and spleen

We previously showed that the deletion of *Trpm7* in T cells results in impaired T cell development and a partial block in the transition from double-negative (CD4$^-$CD8$^-$; DN) to double-positive (CD4$^+$CD8$^+$; DP) cells[33]. This results in an

accumulation of DN thymocytes and reduces the development of single-positive (SP) $CD4^+$ and $CD8^+$ mature T cells[33]. The SP cells egress to the periphery and populate all of the lymphoid organs, but the mice exhibit lymphopenia despite these T cells being resistant to apoptosis[39]. We measured the frequency of T_{reg} cells in the thymus (Fig. 19, A to E) using flow cytometry. To assess thymus-derived T_{reg} cells, we analyzed $Thy1.2^+CD8^-CD4^+$ thymocytes for FOXP3-expressing cells. Thymi from KO mice showed a consistent about threefold increase in the frequency of $FOXP3^+$ T_{reg} cells when compared to thymi from WT mice (Fig. 19C). Because the overall cellularity of the thymus is significantly lower in the KO mice than in the WT mice[33], the ratio of the absolute numbers of T_{reg} cells was also compared (Fig. 19D). The $CD4^+$ thymocytes from KO mice showed modestly increased median fluorescence intensity (MFI) values for FOXP3 staining (Fig. 19E), indicating normal expression of FOXP3 in T cells. These results suggest that the KO thymi generated a T cell population that overrepresents T_{reg} cells. To check whether such a high frequency of T_{reg} cells was also seen in the periphery, we quantified $CD4^+FOXP3^+$ splenocytes (Fig. 19, F to I). The mean percentage of splenic T_{reg} cells was more than twofold higher in KO mice than in WT mice (Fig. 19G). Because the spleens of the KO mice contain a lower number of T cells[33], the mean absolute number of splenic T_{reg} cells in the KO mice was nearly identical to that quantified in the WT mice (Fig. 19H). Consistent with the $CD4^+$ thymocytes, the $CD4^+$ splenic T cells from the KO mice showed modestly

increased MFI for FOXP3 staining (Fig. 19I). We also analyzed the data by stipulating that T_{reg} cells be identified as Thy1.2$^+$CD4$^+$CD25$^+$Foxp3$^+$ cells and T_{eff} cells as Thy1.2$^+$CD4$^+$ cells. The percentage of T_{reg} cells phenotyped in this manner was also significantly higher in the KO mice thymi (Fig. 20B) and showed an increased trend in spleens (Fig. 20C). With this analytical approach, the ratio of T_{reg}:T_{eff} cells in the KO thymus trended higher than that in the WT mice but was not considered significantly different (Fig. 20D). However, the T_{reg}:T_{eff} ratio was still significantly higher in the spleens of the KO mice when compared to that in the spleens of the WT mice (Fig. 20D). Thus, regardless of how the T_{reg} cells were immunophenotyped, deletion of *Trpm7* appreciably increased the T_{reg}:T_{eff} ratio in the periphery. A very small percentage of CD8$^+$ T cells is known to express FOXP3[138]. Therefore, we checked whether the KO mice also showed an abnormally high percentage of CD8$^+$FOXP3$^+$ T cells. We found that the percentage of FOXP3$^+$CD8$^+$ cells was minor and statistically identical in the WT and KO mice (Fig. 20A). To rule out a trivial explanation for these findings, we checked whether the increase in the frequency of T_{reg} cells in the KO mice was due to inefficient deletion of *Trpm7* in T_{reg} cells, giving them an undefined proliferative advantage over T_{eff} cells. To assess the deletion of *Trpm7* in KO T_{reg} cells, we measured the relative abundance in freshly isolated CD4$^+$CD25$^+$ T_{reg} cells of *Trpm7* mRNA transcripts that contained loxP- flanked *exon 17* and confirmed its efficient deletion in KO T_{regs} (Fig. 20E). We also confirmed the loss of TRPM7 currents in KO T_{reg}

cells using patch-clamp electrophysiology (see Fig. 20F for the recording conditions and parameters). The WT $CD4^+CD25^+$ T_{reg} cells readily exhibited the characteristic outwardly rectifying I_{TRPM7} with a reversal potential at 0 mV (Fig. 19J, left). I_{TRPM7} was absent in KO T_{regs}, and only a modest leak current was evident (Fig. 19J, right). These results demonstrate that *Trpm7* was deleted efficiently in the T_{reg} cells. Similar recordings also showed that, when compared to WT $CD4^+CD25^-$ T_{eff} cells, the WT $CD4^+CD25^+$ T_{reg} cells elicited significantly higher TRPM7 current densities (Fig. 19K; see Fig. 20G). The functional importance of increased TRPM7 currents in T_{reg} cells, in comparison to that in T_{eff} cells, is not yet clear. Next, we confirmed that the functional characteristics of KO T_{reg} cells were identical to those of WT T_{reg} cells.

KO T_{reg} cells display normal cell surface and functional characteristics

Immunosuppression by T_{reg} cells is mediated by multiple mechanisms, including inhibitory cytokines (IL-10 and TGF-β), cytolysis of T_{eff} cells (granzyme B), disruption of purinergic signaling by ectonucleotidases (CD39 and CD73), and inhibition of dendritic cell maturation (CTLA4)[139]. First, we evaluated their functional competency in *ex vivo* suppression assays wherein the proliferation of WT $CD4^+CD25^-$ T_{eff} cells was suppressed by the presence of either WT or KO $CD4^+CD25^+$ T_{reg} cells co-cultured at varying ratios (Fig. 21A). The number of

CFSE-labeled WT T_{eff} cells was held constant, and the indicated ratios were achieved by varying the number of T_{reg} cells. The cells were then activated by a mixture of anti-CD3 and anti-CD28 for 3 days, and the cell division of CFSE-labeled T_{eff} cells was measured by flow cytometry (Fig. 21B). Both WT and KO T_{reg} cells suppressed the proliferation of WT T_{eff} cells comparably. Subsequently, we compared the cell surface density of the key functional proteins CD39, CD73, and CTLA4, as well as the expression of genes encoding these proteins, to compare the immunophenotypic features of KO and WT T_{reg} cells. We found that the cell surface abundance of CD39 was less on $CD4^+FOXP3^+$ thymocytes (tT_{reg}) compared to that on peripheral splenic T_{reg} (pT_{reg}) cells. In the KO mice, this trend was preserved, but we observed a substantially greater percentage of $CD39^+$ tT_{reg} and pT_{reg} cells than in their WT counterparts (Fig. 21C). A similar result was seen in the case of CD73 and CTLA4. The MFIs of CD39 and CD73 on thymic and splenic T_{reg} cells and of CTLA4 on splenic T_{reg} cells were significantly higher in KO than in WT mice. Through quantitative polymerase chain reaction (qPCR) analysis, we also showed that *Il10* was significantly higher in KO T_{reg} cells than in KO T_{reg} cells and that *Gzmb* displayed a trending increase (Fig. 22). The relative amounts of *Ctla4*, *Lag3*, *Nt5e*, and *Entpd1* mRNAs were comparable, but *Tgfb1* mRNA was less abundant in the KO T_{reg} cells. On the basis of these data, we conclude that the expression of these genes in KO T_{reg} cells was comparable, but not identical, to that in WT T_{reg} cells. The stability of FOXP3 expression is an important feature

of T_{reg} cells, with tT_{regs} showing the highest stability[140,141]. It has been proposed that tT_{regs} can be identified on the basis of the cell surface expression of neuropilin-1 (Nrp-1) because this marker is expressed only at very low amounts in pT_{reg} cells[142,143]. We found a substantially higher percentage of $NRP1^+$ T_{reg} cells in the thymus but not spleens of KO mice (Fig. 21, E and F). In conjunction with the analysis of T_{reg} cell–specific surface markers, gene expression, and functional competency, we conclude that the KO T_{reg} cells were functional and, because of their increased frequency, could contribute resistance to experimental hepatitis.

Deletion of Trpm7 in thymocytes and T cells increases their sensitivity to IL-2

IL-2 plays a crucial role in regulating the development, maintenance, and function of T_{reg} cells[115–117]. The downstream activity of STAT5, a key transcription factor for T_{reg} cell function, enables stable *Foxp3* gene expression[120,121]. To assess the state of IL-2 signaling in developing thymocytes, we first looked at the expression of its receptor subunit IL-2Rα (also known as CD25). We found that the *Il2ra* transcript abundance in KO thymocytes was five-fold greater than that in WT thymocytes (Fig. 23A). Accordingly, the percentage of $CD25^{hi}$ thymocytes was also increased (Fig. 23B). Concomitantly, deletion of *Trpm7* also increased the amount of IL-2 produced by the KO thymocytes. Analysis of intracellular IL-2 in $Thy1.2^+$ thymocytes showed that KO thymocytes exhibited a significant increase in the MFI

of intracellular IL-2 (Fig. 23, C and D). Although the KO thymocytes produced increased IL-2 in the thymus, the same was not true for the peripheral Thy1.2^{+}CD4^{+} KO T cells in the spleen and mesenteric lymph nodes (Fig. 24A). The concentrations of IL-2 in the sera of WT and KO mice were also identical (Fig. 24B). These results show that the deletion of *Trpm7* in the T cell lineage increased the expression of IL-2 and IL-2Rα in the developing thymocytes and suggest that this increase in IL-2 signaling promoted the development of FOXP3^{+} T_{reg} cells. To confirm that IL-2 signaling was potentiated, we evaluated the phosphorylation of STAT5, a transcription factor downstream of IL-2 signaling. We used flow cytometry to determine the extent of intracellular phosphorylated STAT5 (pSTAT5) staining in thymocytes obtained from WT and KO thymi (Fig. 23E). The frequency of pSTAT5^{+} cells and the MFI of pSTAT5, a measure of STAT5 activity per cell, were significantly higher in KO thymocytes than in WT thymocytes (Fig. 23, F and G). The increased pSTAT5 abundance was confined to thymocytes; freshly isolated splenic T cells showed no difference in pSTAT5 staining (Fig. 23H). Because the gene encoding IL-2Rα is also a transcriptional target of STAT5, we thought that KO thymocytes likely maintain high amounts of surface IL-2Rα and increased pSTAT5 through a positive, feed- forward loop. We measured the occupancy of STAT5 on the *Il2ra* promoter using chromatin immunoprecipitation coupled to qPCR (ChIP-qPCR). Immunoprecipitation of the crosslinked chromatin was performed with a ChIP-grade anti-pSTAT5 or control immunoglobulin Gα

(IgGα) antibody. Antibody- bound genomic DNA was incubated with qPCR primers designed to amplify the two promoter sequences of IL-2Rα. A twofold enrichment of Il2ra promoter sequence in the anti-pSTAT5 chromatin immunoprecipitates was observed in the KO thymocytes as compared to that in the WT thymocytes (Fig. 24G). We hypothesized that TRPM7 restrains the Janus kinase (JAK)–STAT pathway downstream of the *Il2ra* and thus tested whether KO thymocytes treated with IL-2 *ex vivo* would exhibit increased activation of STAT5. When WT thymocytes are treated with IL-2, a very small percentage of cells were $FOXP3^+$ $STAT5^+$ (Fig. 23I; see fig. 24C for gating strategy). In contrast, the KO thymocytes exhibited a substantial increase in the percentage of $pSTAT5^+FOXP3^+$ cells (Fig. 23J). We also quantified the percentage of $STAT5^+$ thymocytes and found that these were also increased in KO thymocytes (Fig. 24D). Although we did not see a difference in basal activation of STAT5 in freshly isolated splenic T cells from WT and KO mice, we examined their sensitivity to stimulation with IL-2 *ex vivo*. Splenic T cells from the KO mice responded rapidly to IL-2 stimulation by phosphorylating STAT5 and showed an almost threefold higher increase in the percentage of $pSTAT5^+FOXP3^+$ cells when compared to splenic T cells from WT mice (Fig. 23, K and L). The increased sensitivity of KO T cells to IL-2 was not limited to $FOXP3^+$ cells (Fig. 24E). The MFI of pSTAT5 staining was greater in IL-2–treated $CD4^+FOXP3^+$ T cells from the KO mice (Fig. 24H), supporting the conclusion that the absence of TRPM7 increases the IL-2 sensitivity of all T cells. Together, these

findings demonstrate that the deletion of *Trpm7* potentiates the development of T_{reg} cells by sensitizing the thymocytes to IL-2 stimulation and promoting the activation of STAT5, a key transcription factor for the regulation of *Foxp3* transcription. On the basis of this model, we evaluated whether the deletion of Trpm7 or pharmacological inhibition of TRPM7 promoted the expression of Foxp3 in IL-2–activated thymocytes *ex vivo*.

Deletion or pharmacological inhibition of TRPM7 augments the induction of Foxp3 during the ex vivo activation of thymocytes

When WT thymocytes were activated *ex vivo* by anti-CD3 antibodies in the presence of IL-2, a modest increase in the abundance of *Foxp3* transcripts was measured by quantitative reverse transcription PCR (qRT-PCR) analysis (Fig. 25A). The deletion of *Trpm7* further increased *Foxp3* transcription (Fig. 25A, left). This increase was abrogated in the presence of a highly selective JAK3 inhibitor (CP690550) (Fig. 25A, right). We then activated the thymocytes *ex vivo* with anti-CD3, IL-2, or a combination of anti-CD3 and IL-2 and evaluated the differentiation of T_{reg} cells ($CD4^+CD25^+FOXP3^+$) after 48 hours of stimulation. Activation by anti-CD3 antibodies and IL-2 resulted in a modest increase in the percentage of WT $CD4^+FOXP3^+$ thymocytes, but the percentage of KO $CD4^+FOXP3^+$ thymocytes almost doubled (Fig. 25, B and C). The augmented differentiation of $CD4^+FOXP3^+$

cells in the presence of anti-CD3 alone was likely due to paracrine production of IL-2 that activated JAK3 and STAT5 through the common γ chain. Because TRPM7 is a bifunctional protein (both an ion channel and a serine-threonine kinase), we investigated whether pharmacological inhibition of the channel pore was sufficient to recapitulate the effects of *Trpm7* deletion. To evaluate the role of the TRPM7 channel specifically, we used FTY720, a U.S. Food and Drug Administration (FDA)–approved sphingosine-1-phosphate receptor (S1PR)–targeting prodrug that is phosphorylated *in vivo* to generate FTY720-P, an analog of S1P[144]. FTY720 blocks the TRPM7 channel without being further modified to its phosphorylated form[145]. Because the previous report identified FTY720 as a TRPM7 channel blocker in experiments with TRPM7-overexpressing cell lines[145], we first confirmed that it blocked native I_{TRPM7} in mouse thymocytes (Fig. 25D). The residual current seen in the presence of FTY720 included leak currents, suggesting that we are underestimating the extent of TRPM7 inhibition. The phosphorylated FTY720 derivative (FTY720-P), which binds to S1PR[144], did not block TRPM7, as illustrated and compared to the known TRPM7 blocker Mg^{2+} (Fig. 25E). We activated WT thymocytes in the presence of FTY720 and FTY720-P to assess the effect on *Foxp3* gene expression. FTY720- treated, but not FTY720-P–treated, thymocytes exhibited an increase in the abundance of *Foxp3* mRNA (Fig. 25F). Because FTY720-P, unlike FTY720, is an agonist of S1PR, these results indicate that the increased transcriptional regulation of *Foxp3* was not

mediated by S1PR. Similar to TRPM7 deletion, inhibition of TRPM7 during *ex vivo* activation also increased the expression of FOXP3 (Fig. 25G), and there was a concomitant increase in STAT5 phosphorylation (Fig. 25, H and I). We then investigated whether injecting FTY720 intraperitoneally (three doses for 6 days at 0.1 μg/kg) could increase the number of T_{reg} cells in WT mice (Fig. 26, C and D). WT mice displayed a ~50% increase in the percentage of T_{reg} cells in the thymus, which was thus comparable to the T_{reg} cell proportion in the KO mice (Fig. 26D). Together, these data support the model that the TRPM7 channel is a negative regulator of JAK-STAT signaling downstream of IL-2R. In KO thymocytes or in WT thymocytes in which the TRPM7 channel is blocked, the activation of STAT5 was potentiated, resulting in increased transcription of *Foxp3* and increased thymic differentiation of $CD4^+FOXP3^+$ T_{reg} cells (Fig. 21, E and F). Because IL-2–dependent STAT5 activation also plays a role in the induction of pT_{reg} cells, we evaluated the *ex vivo* induction of splenic $CD4^+CD25^-$ cells in the presence of TGF-β1 and IL-2. We found that under these conditions, KO T cells showed a modestly increased propensity to differentiate into $CD4^+CD25^+FOXP3^+$ T_{reg} cells (Fig. 26, A and B).

Trpm7^{fl}(Lck Cre) BM chimeras support a non–cell-autonomous mechanism for the increased T_{reg} cell frequency

To gain further mechanistic insight, we performed BM transplantation (BMT) studies. The BM from either *Trpm7^{fl}(Lck Cre)* or *Trpm7^{fl}* control mice was isolated and transplanted into lethally irradiated CD45.1^{+} WT recipient mice. After 8 weeks of convalescence, during which the transplanted hematopoietic cells repopulated the lymphoid organs, the recipient mice were euthanized for the analysis of thymi and spleens by flow cytometry (Fig. 27A). We performed three different BMTs, all into CD45.1 WT recipients: *Trpm7^{fl}* (WT) BM, *Trpm7^{fl}(Lck Cre)* (KO) BM, and a 1:1 mixture of WT and KO BM (Fig. 27A, right). When we analyzed thymic cellularity, it became apparent that the KO BM recipients displayed a significantly reduced number of total thymocytes (on average, a sevenfold reduction; Fig. 27B). This loss of cellularity also manifested itself as thymic involution that was visible during dissection, which mirrored the highly penetrant phenotype of the KO [*Trpm7^{fl}(Lck Cre)*] mice[33]. Because the recipient mice were WT for TRPM7, this observation indicates that the deletion of *Trpm7* in thymocytes alone contributes to the deterioration of the thymic architecture, possibly through abnormal secretion of various paracrine factors. Despite the reduced number of retrieved donor thymocytes, the absolute number of tT_{reg} cells was comparable to those achieved with the WT and MIX (mix of WT and KO BM cells) donors (Fig. 27C). The number of Teff cells also trended lower with KO BMT, but this difference was not

statistically significant with the small sample size of the BMT experiments (Fig. 27D). Expectedly, in comparison to the WT or MIX recipients, the T_{reg}:T_{eff} ratio was much higher in the KO BMT recipients (Fig. 27E). To understand the relative contributions of donor and recipient populations in the overall thymic output, we quantified CD45.1$^+$ and CD45.2$^+$ cells in the WT, KO, and MIX BMTs (Fig. 28). The reconstitution efficiency was high for the WT cells in both the WT and MIX transplant scenarios (Fig. 28B). The KO cells, on the other hand, yielded greatly reduced numbers of thymocytes in the KO BMT and were outcompeted by the WT CD45.1$^+$ cells in the MIX BMT. Similarly, the yield of CD4$^+$ T cells (Fig. 28C) and T_{eff} cells (Fig. 28D) from the KO BMT was also very low. However, when we evaluated the composition of the T_{reg} cells in the KO BMT, we found that the transplantation of KO BM increased the differentiation of host (CD45.1$^+$) T_{reg} cells (Fig. 28E). This result suggests that the *Trpm7*$^{-/-}$ thymocytes enhanced the differentiation of WT thymocytes and that non–cell-autonomous mechanisms underlie the increased T_{reg} population in the *Trpm7*-targeted mice. We also assessed the corresponding T cell populations in the recipient spleens to further define this phenomenon. The absolute number of splenocytes was similar in the case of the WT, KO, and MIX BMTs (Fig. 28F). Thus, as was reported earlier[33], the loss of thymic cellularity caused by the deletion of *Trpm7* in thymocytes did not have a major negative effect on peripheral T cell numbers. In comparison to the WT BMT, the number of splenic T_{reg} cells was modestly higher in the KO and MIX

BMTs, but the difference was not statistically significant (Fig. 28G). The number of T_{eff} cells in the KO BMT was comparable to that in WT cell recipients (Fig. 28H) but the splenic T_{reg}:T_{eff} ratio was higher in the case of KO BMT when compared to the WT and MIX chimeras (Fig. 27I). We also examined the splenic cells for their origins by binning the cells into $CD45.1^+$ and $CD45.2^+$ populations (Fig. 28, F and G). Overall, the host population of T_{reg} cells was significantly increased in the KO BM recipients as compared to that in the WT BM recipients (Fig. 28G). These results indicate that the presence of transplanted *Trpm7*$^{-/-}$ T cells potentiated the number of T_{reg} cells and that the underlying mechanism is predominantly nonautonomous in manner. At its simplest level, this is best explained by the IL-2 overproduction by the *Trpm7*$^{-/-}$ T cells, but we cannot exclude other paracrine factors. Together, these results are consistent with our proposed model that the deletion of TRPM7 promotes T_{reg} cell development by increasing IL-2 production and thus promoting the subsequent IL-2–dependent FOXP3 expression in the thymocytes.

Discussion

The major insight derived from this study is the function of the ion channel TRPM7 in controlling the development and frequency of tT_{reg} cells. This serendipitous discovery emerged from the observation that the deletion of *Trpm7* in lineage cells

rendered the mice highly resistant to Con A–induced hepatitis, an experimental form of AIH that is driven by T cells. We propose that the increased generation of tT_{reg} cells in these mice is an important contributing factor, but not the only contributing factor, that protects these mice in this disease model. In addition, we also showed that although KO T_{eff} cells were activated normally, they showed differences in their cytokine output. We showed that KO thymocytes were competent in immunosuppression assays. Future studies will comprehensively characterize the physiological and immunosuppressive properties of *Trpm7*$^{-/-}$ tT_{reg} cells in the context of other models of T cell–driven autoimmune diseases. Because FTY720 is already an FDA- approved drug, the findings have implications for translational research and medicinal chemistry approaches for the development of more selective blockers of TRPM7. Our results suggest that increased IL-2 signaling in the KO thymocytes underlies the increased output of tT_{reg} cells. The KO thymocytes produced significantly increased amounts of IL-2, and they also showed increased expression of the IL-2R subunit CD25. BMT experiments supported the model that the mechanism that drives the increased differentiation of tT_{reg} cells is predominantly cell extrinsic. The increased production of IL-2 by KO thymocytes and increased cell surface CD25, which is encoded by a STAT5 target gene[146], likely contributes in a feed-forward loop to increase IL-2 sensitivity in the KO T cells. Consistently, during *ex vivo* activation, the KO thymocytes showed increased sensitivity to IL-2 and showed inducible synthesis

of FOXP3. In our conception, this increased sensitivity to IL-2 in *ex vivo* conditions is primarily a result of the high quantity of CD25 on the cell surface, but it remains possible that TRPM7 also regulates signals downstream of the IL-2R. In the lymph nodes, IL-2 signaling and STAT5 mediate a crucial function in enabling T_{reg} cells to constrain the local expansion of conventional T cells into damage-causing T_{eff} cells[147]. Future studies will evaluate whether increased sensitivity to IL-2 makes the KO T_{reg} cells more competent in restraining inflammatory cascades in organ systems such as the liver, gut, and skin. The mechanism through which the channel activity of TRPM7 influences IL-2 production in the developing thymocytes remains unclear at this point and will be a major focus of our future studies. During T cell activation, *Il2* transcription is predominantly controlled by the SOCE-dependent NFAT (nuclear factor of activated T cells) pathway. In mice in which SOCE, through Orai channels, is abolished selectively in the T cell lineage, the mice fail to develop an adequate number of T_{reg} cells[148]. In essence, the functions of the Orai and TRPM7 channels are designed to be in opposition during the process of T_{reg} cell development. Hence, the general design principles underlying the checks and balances in immune regulation appear to be preserved even at the scale of rapid electrical signaling[149]. From the standpoint of the two- step model[122] of T_{reg} cell development, Ca^{2+} entry through the Orai channels is likely essential for the strong, TCR-dependent signals that drive NFAT activation and the subsequent increased abundance of IL-2, IL-2R, and possibly other com-ponents

of the IL-2 signaling pathway in the developing thymocytes. As shown here, deletion of TRPM7 had no discernible effect on SOCE amplitude but did have a modest effect on its kinetics. Whether this is enough to substantially enhance NFAT activity (and increased *Il2* expression) is an outstanding question. It is also possible that TRPM7 influences *Il2* transcription independently of SOCE. In addition to conducting Ca^{2+}, TRPM7 also conducts Zn^{2+}, and the role of Zn^{2+} signaling in T cell biology is not yet well understood. TRPM7 channel activity is polymodally regulated by changes in internal Mg^{2+} concentration[150], phospholipids[151], pH[152], and C-terminal proteolysis[39,153]. These regulatory properties of TRPM7 may enable the developing thymocytes to integrate multiple signals in the thymic microenvironment to tune tT_{reg} cell development. Because FTY720 is already an FDA-approved drug, our findings have implications for translational research, as well as for medicinal chemistry approaches for more selective blockers of TRPM7. In the context of S1PR pharmacology, FTY720 functions as a prodrug, which is phosphorylated in vivo to generate FTY720-P, which is an S1PR ligand. Binding of S1PR by FTY720-P, but not by FTY720, promotes the sequestration of lymphocytes in lymph nodes, resulting in immunosuppression. Through patch- clamp recordings of thymocytes, we confirmed that the TRPM7 channel is blocked by FTY720, but not by FTY720-P; this enables the inhibition of TRPM7 without modulating S1PR. In the presence of FTY720, but not FTY720-P, stimulation of activated thymocytes with IL-2

increased the transcription of *Foxp3* and promoted the *ex vivo* differentiation of T_{reg} cells. Note that treating human patients with FTY720 increases the frequency of T_{reg} cells[154], suggesting that at least some component of FTY720- mediated immunosuppression may be mediated by increasing the frequency and function of T_{reg} cells through TRPM7 channel inhibition. Although the involvement of the channel activity of TRPM7 was indicated by experiments involving FTY720, the role of the kinase domain of TRPM7 cannot be ruled out. Cleavage of TRPM7 at Asp1510 increases the ion channel activity and liberates a functional kinase domain (M7CK-S)[39], whereas cleavage sites N-terminal of Asp1510 inactivate the channel and liberate a longer kinase domain (M7CK-L) that translocates to the nucleus and modifies chromatin through histone phosphorylation[130]. It remains possible that during T cell development, the kinase domain plays an important role in reprogramming the chromatin landscape. Our study opens the door toward a deeper investigation of TRPM7 and other ion channels in the development, function, and stability of T_{reg} cells. In the future, it may be possible to increase the number of T_{reg} cells in vivo with TRPM7-targeting drugs and thereby induce tolerance in patients suffering from autoimmunity.

CHAPTER THREE FIGURES

Figure 14

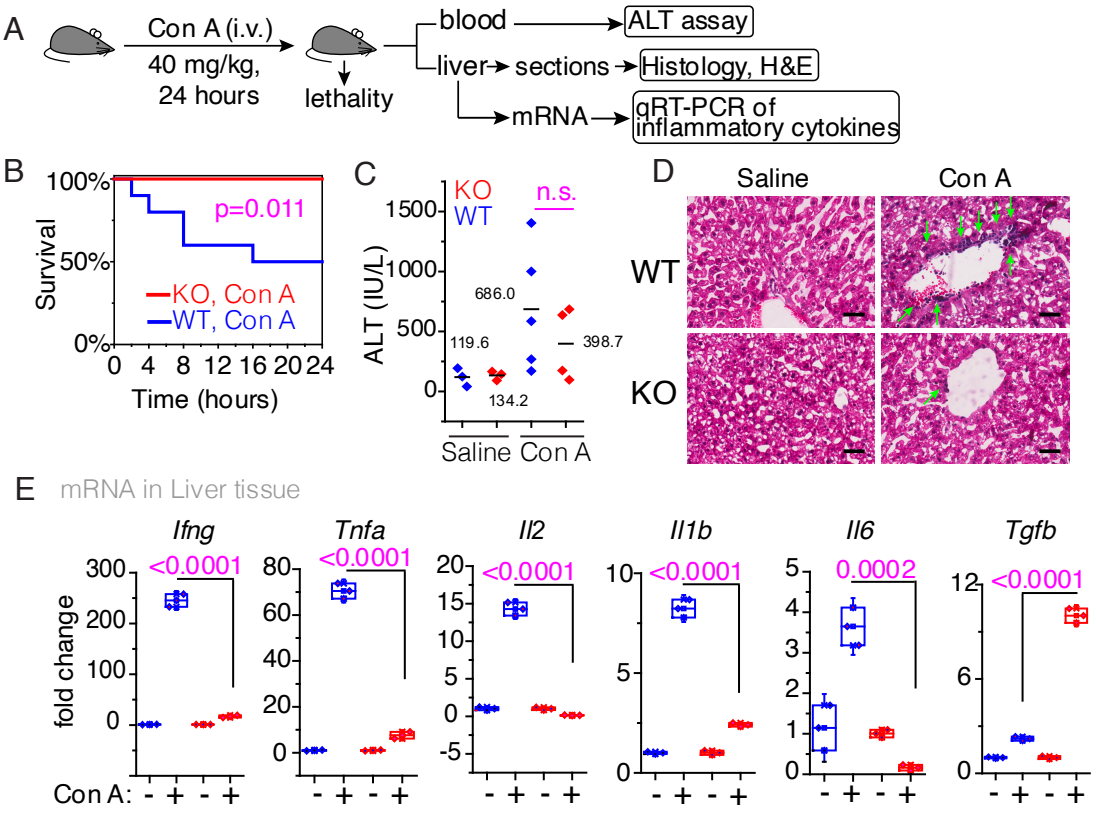

Figure 14. Deletion of *Trpm7* in T cells protects mice from Con A-induced experimental lethal hepatitis.

(A) Cartoon of the experimental scheme and sample processing.

(B) Kaplan-Meier survival analysis of $Trpm7^{fl/fl}$ (WT) and $Trpm7^{fl/fl}$*(Lck Cre)* (KO) mice injected intravenously (i.v.) with Con A (40 mg/kg) and assessed more than 24 hours. Log-rank value=6.36, P=0.011; *n=10* mice in each group.

(C) Serum alanine transaminase (ALT) concentrations in WT and KO mice 24 hours after the administration of Con A or saline. For the three WT mice that died before the 12- hour time point, ALT concentrations were not recorded (*n=4*; data analyzed by two-tailed *t* test). n.s., not significant.

(D) Hematoxylin and eosin (H&E) staining of liver sections from WT and KO mice injected intravenously with saline or Con A (40 mg/kg). Scale bars, 100 μm. Green arrows indicate regions of perivascular infiltration by immune cells. Images are representative of liver sections from three different WT and KO mice.

(F) Gene expression analysis (qPCR) of the indicated cytokine-encoding genes in WT (blue) and KO (red) mouse liver tissue 24 hours after administration of saline or Con A (*n=3*; P values were calculated by two-tailed *t* test).

Figure 15

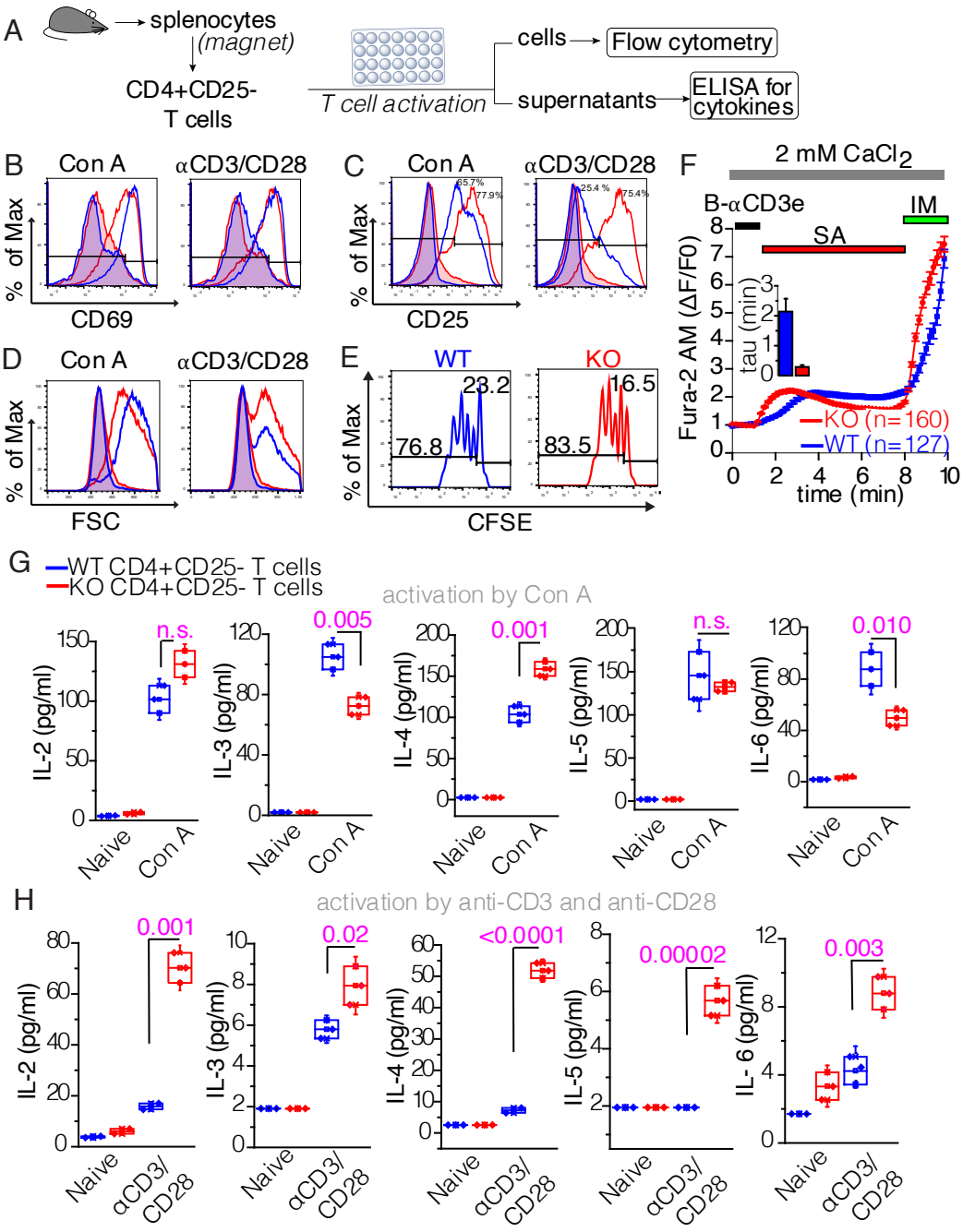
A
splenocytes
(magnet)
CD4+CD25-
T cells
T cell activation
cells
Flow cytometry
supernatants
ELISA for cytokines
B
Con A
αCD3/CD28
% of Max
CD69
C
Con A
αCD3/CD28
% of Max
CD25
D
Con A
αCD3/CD28
% of Max
FSC
E
WT
KO
% of Max
76.8
23.2
83.5
16.5
CFSE
F
2 mM CaCl2
B-αCD3e
IM
SA
Fura-2 AM (ΔF/F0)
tau (min)
KO (n=160)
WT (n=127)
time (min)
G
WT CD4+CD25- T cells
KO CD4+CD25- T cells
activation by Con A
IL-2 (pg/ml)
n.s.
IL-3 (pg/ml)
0.005
IL-4 (pg/ml)
0.001
IL-5 (pg/ml)
n.s.
IL-6 (pg/ml)
0.010
Naive
Con A
H
activation by anti-CD3 and anti-CD28
IL-2 (pg/ml)
0.001
IL-3 (pg/ml)
0.02
IL-4 (pg/ml)
<0.0001
IL-5 (pg/ml)
0.00002
IL- 6 (pg/ml)
0.003
Naive
αCD3/ CD28

Figure 15. Activation of KO T_{eff} cells is normal upon TCR stimulation.

(A) Schematic of the experimental procedures. Splenocytes were magnetically isolated and then activated with a mixture of anti-CD3 and anti-CD28 antibodies (αCD3/CD28) or Con A.

(B) Flow cytometry histograms showing the cell surface abundance of the activation marker CD69 on CD4+CD25−primary T cells from WT and KO mice after in vitro activation for 48 hours by Con A (5 μg/ml) (left) or by a mixture of anti-CD3 and anti-CD28 antibodies (right). Blue- and red-filled histograms show CD69 abundance on naive WT and KO cells, respectively. Unfilled histograms show CD69 after activation. Histograms are representative of three independent experiments.

(C) Flow cytometry analysis of the abundance of the activation marker CD25 on WT and KO $CD4^+CD25^-$T cells after stimulation as described in (B). Histograms are representative of three independent experiments.

(D) Representative histograms showing forward scatter (FSC) as a measure of activation for WT (blue) and KO (red) $CD4^+$CD25−T cells (*n*=*3*).

(E) Analysis of the division of CFSE-labeled WT and KO $CD4^+CD25^-$ T cells as measuring the dilution of CFSE 72 hours after activation by anti-CD3 and anti-CD28 antibodies. The percentage of dividing cells (left gate) and undivided cells (right gate) are shown. Data are representative of three experiments.

(F) Ca^{2+} responses in WT (blue) and KO (red) thymocytes after TCR stimulation.

The intracellular Ca^{2+} increase was observed in response to the binding of streptavidin (SA) to biotinylated anti-CD3e, which was previously added to the cells. Ionomycin (IM) was used as a positive control and denotes maximal Ca^{2+} responses. The number of cells assessed is shown. The inset bar graph illustrates the rise time (tau) of fluorescence upon streptavidin treatment in WT and KO thymocytes.

(G) Quantification of secreted cytokines as detected in the cell culture medium of $CD4^+CD25^-$ T cells activated for 72 hours with Con A (5 μg/ml). The P values were calculated by two-tailed *t* test and are denoted on the box charts (n=3 to 4).

(H) Quantification of secreted cytokines as detected in the cell culture medium of $CD4^+CD25^-$ T cells activated for 72 hours with a mixture of anti-CD3 and anti-CD28 antibodies (each at 5 μg/ml). The *P* values were calculated by two-tailed *t* test and are denoted on each box chart (*n*=3 or 4 samples).

Figure 16

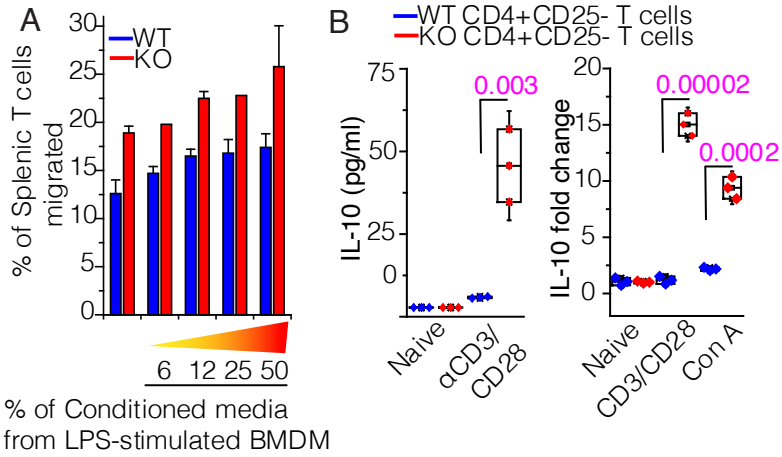
A
WT
KO
% of Splenic T cells migrated
30
25
20
15
10
5
0
6 12 25 50
% of Conditioned media from LPS-stimulated BMDM
B
WT CD4+CD25- T cells
KO CD4+CD25- T cells
IL-10 (pg/ml)
75
50
25
0
0.003
Naive
αCD3/ CD28
IL-10 fold change
20
15
10
5
0
0.00002
0.0002
Naive
CD3/CD28
Con A

Figure 16. Activation and migration of KO T cells.

(A) Analysis of the migration of WT and KO T cells through membranes (pore size: 5.0 μm) in a transwell system. Conditioned medium from LPS-treated bone marrow–derived macrophages (BMDMs) was used as chemoattractant in the bottom chamber (see Materials and Methods for details). Data are presented as the percentage of T cells that migrated across the membrane.

(B) Left: Quantification of IL-10 secretion by WT and KO $CD4^+$ T cells 72 hours after activation with anti-CD3 and anti-CD28 antibodies. Box charts represent mean cytokine concentrations (n = 3); error bars indicate SEM. Right: Quantification of *Il10* mRNA in WT and KO $CD4^+$ T cells after 48 hours of activation with either anti-CD3 and anti-CD28 antibodies or Con A.

Figure 17

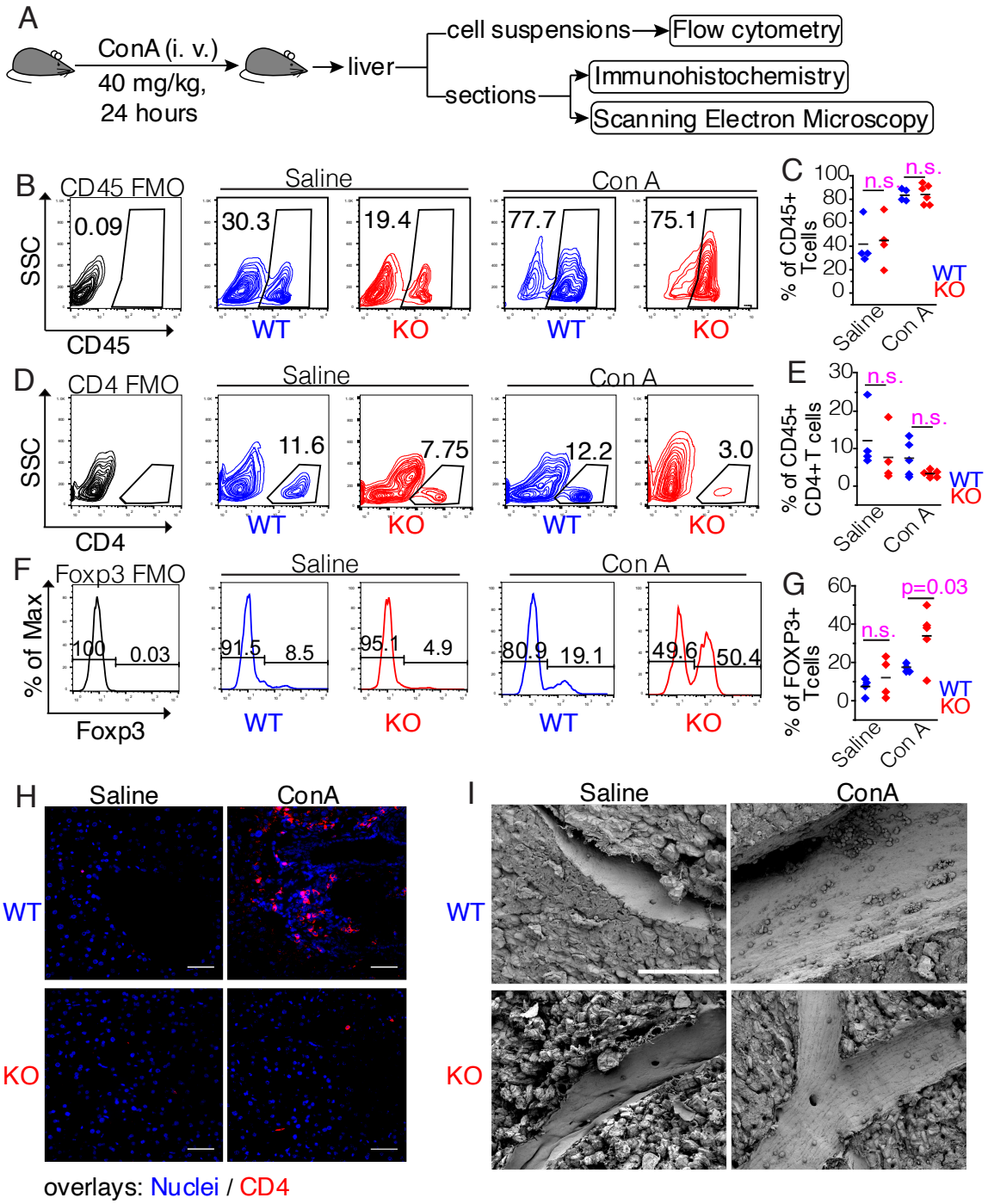
A
ConA (i. v.)
40 mg/kg,
24 hours
liver
cell suspensions
Flow cytometry
sections
Immunohistochemistry
Scanning Electron Microscopy
B
CD45 FMO
SSC
CD45
0.09
Saline
Con A
30.3
19.4
77.7
75.1
WT
KO
C
% of CD45+ Tcells
n.s.
n.s.
Saline
Con A
D
CD4 FMO
CD4
11.6
7.75
12.2
3.0
E
% of CD45+ CD4+T cells
F
Foxp3 FMO
% of Max
Foxp3
100
0.03
91.5
8.5
95.1
4.9
80.9
19.1
49.6
50.4
G
% of FOXP3+ Tcells
p=0.03
H
Saline
ConA
I
overlays: Nuclei / CD4

Figure 17. Increased infiltration of T_{reg} cells in the livers of Con A–treated KO mice.

(A) Experimental scheme.

(B) Bivariant cytographs showing infiltration of $CD45^+$ hematopoietic cells into the livers of WT (blue) and KO (red) mice 24 hours after the administration of saline or Con A (40 mg/kg, intravenously). CD45 FMO refers to the "fluorescence minus one" control, wherein cells were analyzed without staining with anti-CD45 antibody to enable accurate gating. Plots are representative of four to six experiments.

(C) Quantification of the number of $CD45^+$ hematopoietic cells based on the flow cytometry analysis shown in (B). Mean values are indicated by dashes. The data were collected from four independent experiments.

(D) Bivariant cytographs showing the infiltration of $CD45^+CD4^+$ T cells into the livers of WT and KO mice 24 hours after administration of saline or Con A (40 mg/kg, intravenously). Plots are representative of four to six experiments.

(E) Quantification of the number of $CD45^+CD4^+$ T cells based on the flow cytometry analysis shown in (D). Mean percentage values are indicated by dashes. The data were collected from four independent experiments.

(F) Flow cytometry histograms of $CD4^+Foxp3^+$ cells from the livers of WT (blue) and KO (red) mice 24 hours after administration of saline or Con A. The Foxp3 histograms were obtained from a cell population determined by sequential gating for a FSC/SSC profile, $CD45^+$, and $CD4^+$ (see Fig. 18 for the gating scheme).

(G) Quantification of Foxp3$^+$ T_{reg} cells in the livers of WT (blue) and KO (red) mice from the experiments shown in (F). The *P* value was calculated by *t* test. The data were collected from four independent experiments.

(H) Immunofluorescence microscopy of infiltrating CD4$^+$ T cells in liver sections.

(I) Representative SEM images of liver sections from the indicated mice at ×850 magnification. Scale bars, 100 μm.

Figure 18

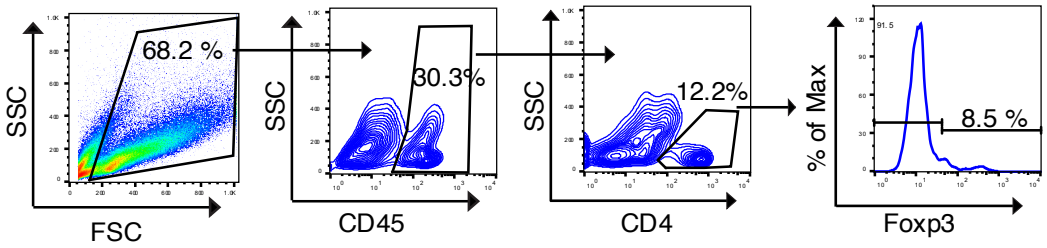

Figure 18. Gating scheme used to derive the Foxp3 histograms.

The gating strategy used for the graphs shown in Fig. 17F. From the FSC and SSC lymphocyte gate, $CD45^+$ cells, then $CD4^+$ cells, and $Foxp3^+$ cells were derived.

Figure 19

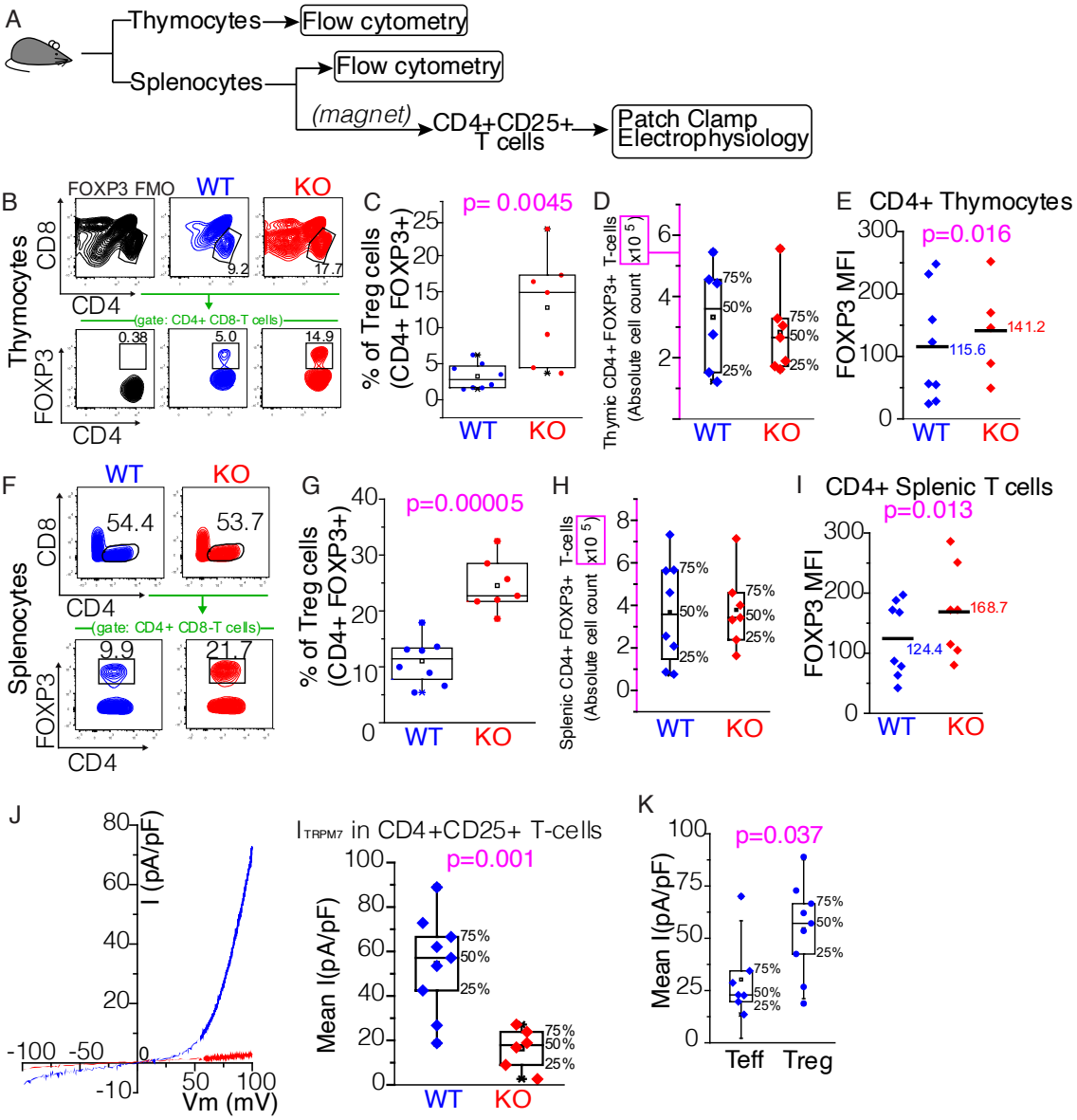
A
Thymocytes
Flow cytometry
Splenocytes
Flow cytometry
(magnet)
CD4+CD25+ T cells
Patch Clamp Electrophysiology
B
FOXP3 FMO
WT
KO
Thymocytes
CD8
CD4
(gate: CD4+ CD8-T cells)
FOXP3
9.2
17.7
0.38
5.0
14.9
C
p= 0.0045
% of Treg cells (CD4+ FOXP3+)
WT
KO
D
Thymic CD4+FOXP3+ T-cells (Absolute cell count x10^5)
75%
50%
25%
E
CD4+ Thymocytes
p=0.016
FOXP3 MFI
115.6
141.2
F
Splenocytes
54.4
53.7
9.9
21.7
G
p=0.00005
H
Splenic CD4+ FOXP3+ T-cells (Absolute cell count x10^5)
I
CD4+ Splenic T cells
p=0.013
124.4
168.7
J
I (pA/pF)
Vm (mV)
I_TRPM7 in CD4+CD25+ T-cells
p=0.001
Mean I(pA/pF)
K
p=0.037
Teff
Treg

Figure 19. KO mice display increased numbers of $CD4^+Foxp3^+$ T_{reg} cells in the thymus and spleen.

(A) Experimental scheme.

(B) Representative flow cytometry contour plots sequentially gated on $CD4^+$ (top) and $Foxp3^+$ T_{reg} cells (bottom) in thymi isolated from WT (blue) and KO (red) mice.

(C) Frequency of $CD4^+Foxp3^+$ T_{reg} cells in thymi from WT (blue) and KO (red) mice. The mean value is denoted by an empty square, and the median value is denoted by a horizontal line. The *P* value was calculated by two-tailed, unpaired Student's *t* test.

(D) Absolute numbers of $CD4^+Foxp3^+$ thymocytes in thymi from WT (blue) and KO (red) mice. The empty square denotes the mean, and the horizontal line denotes the median.

(E) MFI values of $FOXP3^{in}$ $CD4^+$ WT (blue) and KO (red) thymocytes. *P* value was calculated by two-tailed paired *t* test.

(F) Contour plots showing the frequencies of $CD4^+$ and $Foxp3^+$ T_{reg} cells in the spleens of WT (blue) and KO (red) mice.

(G) Box charts show the frequency of $CD4^+Foxp3^+$ Treg cells in the spleens of WT (blue) and KO (red) mice.

(H) Absolute numbers of $CD4^+Foxp3^+$ T_{reg} cells in splenocytes isolated from WT (blue) and KO (red) mice.

(I) Quantification of the MFI for $FOXP3^{in}$ $CD4^+$ splenic T cells from the indicated mice. *P* value was calculated by two-tailed paired *t* test.

(J) I-V relationship of I_{TRPM7} in $CD4^+CD25^+$ WT Treg (blue trace) and KO Treg (red trace) cells obtained by whole-cell patch-clamp recordings. The patch-clamp configuration and the recording conditions are shown in Fig. 7F. The box chart shows the I_{TRPM7} current densities quantified at 5min after break-in at 100 mV in WT and KO T_{reg} cells. See Materials and Methods for a description of the statistical parameters shown in the box chart.

(K) The box chart shows the I_{TRPM7} current densities quantified at 5min after break-in at 100 mV in T_{eff} ($CD4^+CD25^-$) and T_{reg} ($CD4^+CD25^+$) cells isolated from WT mice. The *P* value was calculated by two-tailed unpaired *t* test. Each filled circle represents data obtained from an individual cell.

Figure 20

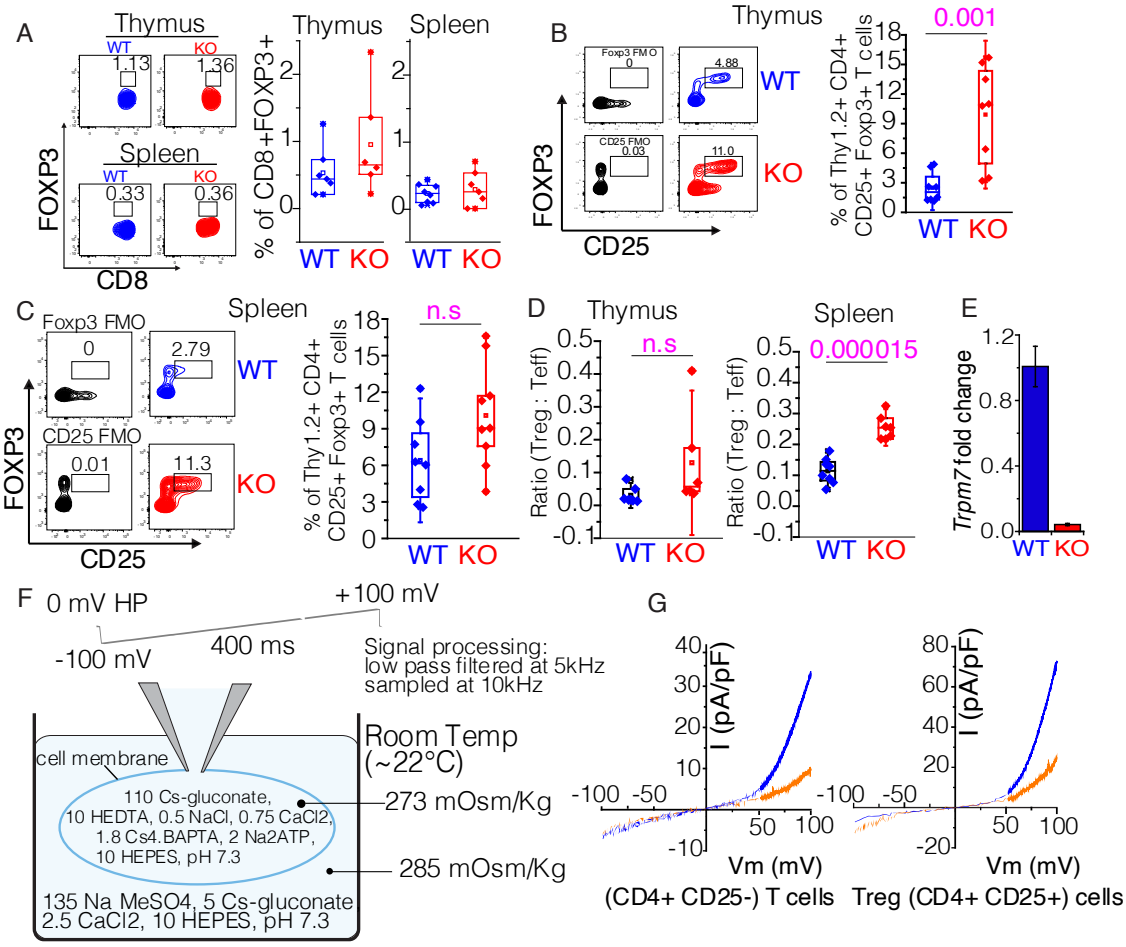
A
Thymus
WT
KO
1.13
1.36
Spleen
0.33
0.36
FOXP3
CD8
% of CD8+FOXP3+
Thymus
Spleen
WT KO WT KO
B
Thymus
Foxp3 FMO
0
4.88
WT
CD25 FMO
0.03
11.0
KO
FOXP3
CD25
% of Thy1.2+ CD4+ CD25+ Foxp3+ T cells
0.001
WT KO
C
Foxp3 FMO
0
2.79
WT
CD25 FMO
0.01
11.3
KO
FOXP3
CD25
Spleen
% of Thy1.2+ CD4+ CD25+ Foxp3+ T cells
n.s
WT KO
D
Thymus
n.s
Ratio (Treg : Teff)
Spleen
0.000015
WT KO
E
Trpm7 fold change
WT KO
F
0 mV HP
+100 mV
-100 mV
400 ms
Signal processing:
low pass filtered at 5kHz
sampled at 10kHz
Room Temp
(~22°C)
cell membrane
110 Cs-gluconate,
10 HEDTA, 0.5 NaCl, 0.75 CaCl2,
1.8 Cs4.BAPTA, 2 Na2ATP,
10 HEPES, pH 7.3
273 mOsm/Kg
285 mOsm/Kg
135 Na MeSO4, 5 Cs-gluconate
2.5 CaCl2, 10 HEPES, pH 7.3
G
I (pA/pF)
Vm (mV)
(CD4+ CD25-) T cells
Treg (CD4+ CD25+) cells

Figure 20. Quantification of T_{reg} cells in the thymi and spleens of WT and KO mice.

(A) Left: Bivariant cytograph showing the percentage of $Foxp3^+CD8^+$ cells in the thymi and spleens of WT and KO mice. Right: Box chart shows the quantification and statistical analysis of $CD8^+Foxp3^+$ T cells in the thymi and spleens.

(B) Left: Flow cytometry contour plot showing the staining of cell surface CD25 and intracellular FOXP3 in previously gated $Thy1.2^+CD4^+$ WT and KO thymocytes. Right: The box chart quantifies the percentage of $CD4^+CD25^+Foxp3^+$ thymocytes in WT and KO mice. The mean value (empty square) and the median (horizontal line) are shown in the boxes. Data were collected from four independent experiments and the diamonds in the box chart denote individual mice. The indicated *P* value was calculated by two-tailed Student's *t* test.

(C) Left: Flow cytometry contour plot shows the staining of cell surface CD25 and intracellular FOXP3 in previously gated $Thy1.2^+CD4^+$ splenic T cells obtained from WT and KO mice. Right: The box chart quantifies the percentage of $CD4^+CD25^+Foxp3^+$ T cells in spleens from the WT and KO mice. The mean value is shown by an empty square and the median by a horizontal line. Data were collected from four independent experiments. The indicated *P* value was calculated by two-tailed Student's *t* test.

(D) The box chart shows the calculated ratios of T_{reg}:T_{eff} cells in the thymi and spleens of WT and KO mice. The indicated *P* value was calculated by two-tailed

unpaired *t* test.

(E) Bar graph showing the relative expression of *Trpm7* in T_{reg} cells ($CD4^+CD25^+$) obtained from the spleens of WT and KO mice. The qPCR primers were specific for exon 17 of *Trpm7*, and the relative amounts of *Trpm7* exon 17–containing mRNA in the KO T_{reg} cells is shown.

(F) Whole-cell, patch clamp recording conditions used to isolate and measure I_{TRPM7} are schematized. Internal (pipet) and external (bath) solutions are shown. The voltage ramp parameters used to derive the I-V relationship of I_{TRPM7} are shown together with the filtering and sampling parameters used for signal processing.

(G) I-V relationship (blue trace) of I_{TRPM7} in WT $CD4^+CD25^-$ (T_{conv}) and $CD4^+CD25^+$ (T_{reg}) cells obtained by whole-cell, patch clamp recordings. The orange trace shows the inhibition of I_{TRPM7} by perfusion of 10 mM Mg^{2+}, a known TRPM7 channel inhibitor. These are representative IV relationships (*n*=7).

Figure 21

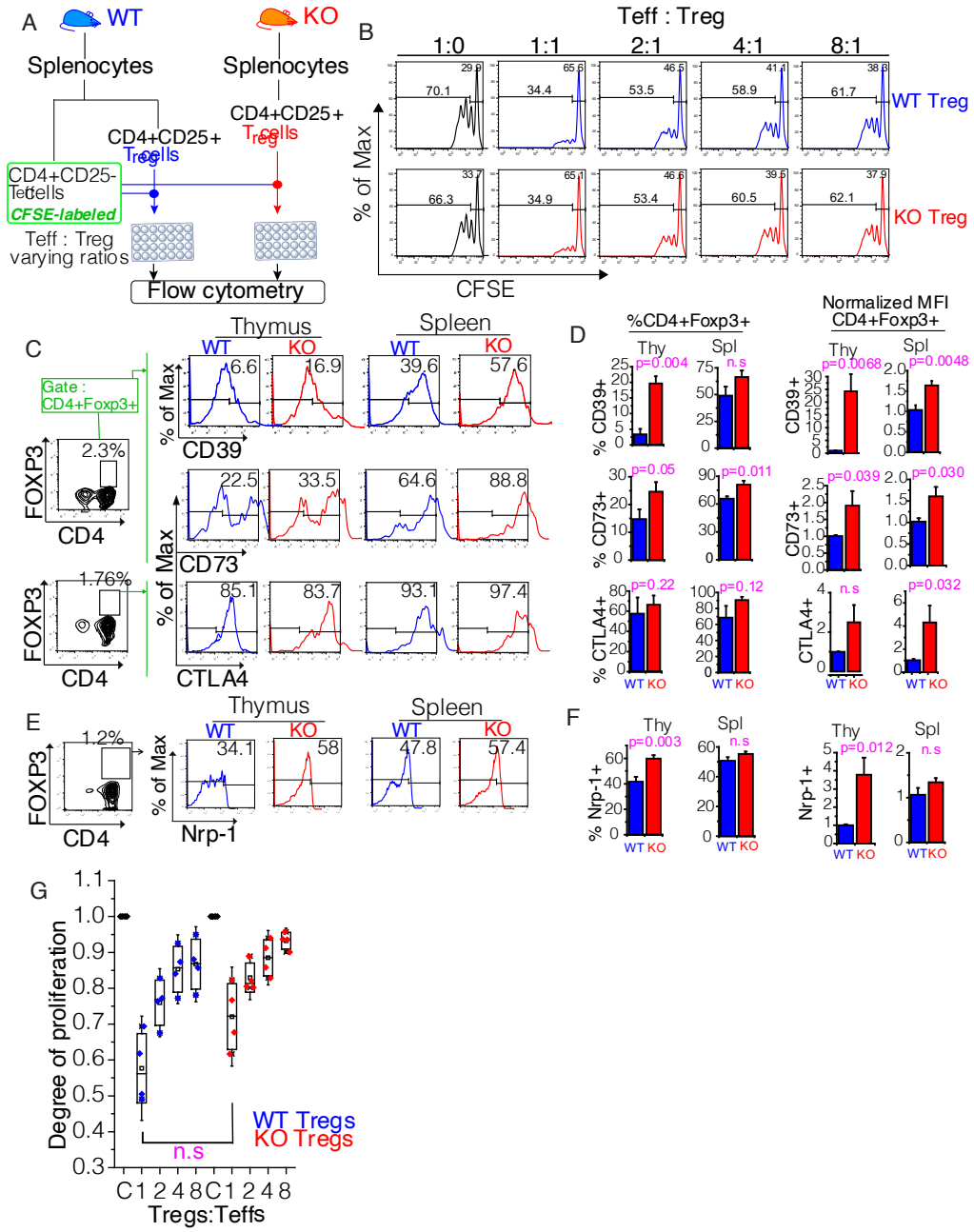
A
WT
KO
Splenocytes
Splenocytes
CD4+CD25+ Treg cells
CD4+CD25+ Treg cells
CD4+CD25- Tcells
CFSE-labeled
Teff : Treg varying ratios
Flow cytometry
B
Teff : Treg
1:0
1:1
2:1
4:1
8:1
70.1
34.4
53.5
58.9
61.7
WT Treg
66.3
34.9
53.4
60.5
62.1
KO Treg
% of Max
CFSE
C
Thymus
Spleen
WT
KO
Gate : CD4+Foxp3+
2.3%
FOXP3
CD4
% of Max
CD39
6.6
16.9
39.6
57.6
CD73
22.5
33.5
64.6
88.8
1.76%
CTLA4
85.1
83.7
93.1
97.4
D
%CD4+Foxp3+
Normalized MFI CD4+Foxp3+
Thy
Spl
% CD39+
p=0.004
n.s
CD39+
p=0.0068
p=0.0048
% CD73+
p=0.05
p=0.011
CD73+
p=0.039
p=0.030
% CTLA4+
p=0.22
p=0.12
CTLA4+
n.s
p=0.032
WT KO
E
Thymus
Spleen
1.2%
FOXP3
CD4
% of Max
Nrp-1
34.1
58
47.8
57.4
F
Thy
Spl
% Nrp-1+
p=0.003
n.s
Nrp-1+
p=0.012
n.s
G
Degree of proliferation
WT Tregs
KO Tregs
n.s
C 1 2 4 8 C 1 2 4 8
Tregs:Teffs

Figure 21. Characterization of T_{reg} cells isolated from the thymus and lymph nodes of KO mice.

(A) Experimental scheme used for the suppression assays.

(B) Analysis of CFSE-labeled WT T cell proliferation after 3 days of culture in the presence of T_{reg} cells isolated from WT (blue) and KO (red) mice. The ratios indicate the relative numbers of $CD4^+CD25^-$ T_{eff} cells to $CD4^+CD25^+$ T_{reg} cells plated on day 1. Histograms show the dilution of CFSE in T_{eff} cells as measured by flow cytometry. The percentage of T_{eff} cells showing dilution of the CFSE dye reflects the proportion of T_{eff} cells that underwent cell division. Data are representative of four experiments.

(C) T_{reg} cells from the thymi and spleens of WT (blue) and KO (red) mice were identified by flow cytometry (left, bivariant gating for CD4 and Foxp3) and further analyzed for the expression of the T_{reg} cell functional markers CD39, CD73, and CTLA4 (histograms).

(D) Percentages of positive cells (left) and MFI values (right) for CD39, CD73, and $CTLA4^{in}$ thymic and splenic $CD4^+Foxp3^+$ Tregs from WT and KO mice. The data were collected from two independent experiments with a total sample size of four mice. The *P* value was calculated by one-tailed unpaired *t* test.

(E) Cell surface expression of neuropilin-1 (Nrp-1) on thymic and splenic T_{reg} cells ($CD4^+Foxp3^+$) from WT (blue) and KO (red) mice.

(F) Bar graphs showing the percentage of positive cells (left) and MFI values (right)

for Nrp-1^{in} thymic and splenic T cells from WT and KO mice. The data were collected from two independent experiments with a total sample size of four mice. The *P* value was calculated by one-tailed unpaired *t* test.

(G) Proliferation of T_{eff} cells in the presence of T_{reg} cells at the indicated ratios in relation to maximal proliferation (no T_{reg} cells), which is represented by control, C.

Figure 22

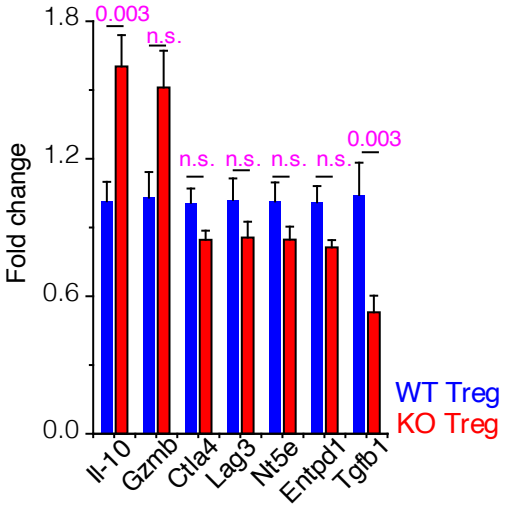
1.8
1.2
0.6
0.0
Fold change
0.003
n.s.
n.s.
n.s.
n.s.
n.s.
0.003
WT Treg
KO Treg
Il-10
Gzmb
Ctla4
Lag3
Nt5e
Entpd1
Tgfb1

Figure 22. Expression of selected mediators in WT and KO T_{reg} cells.

Gene expression analysis (as determined by qPCR) of the indicated T_{reg} cell markers in freshly isolated WT (*n* = 4) and KO (*n* = 6) splenic $CD4^+CD25^+$ cells. The indicated *P* values were calculated by two-tailed *t* test.

Figure 23

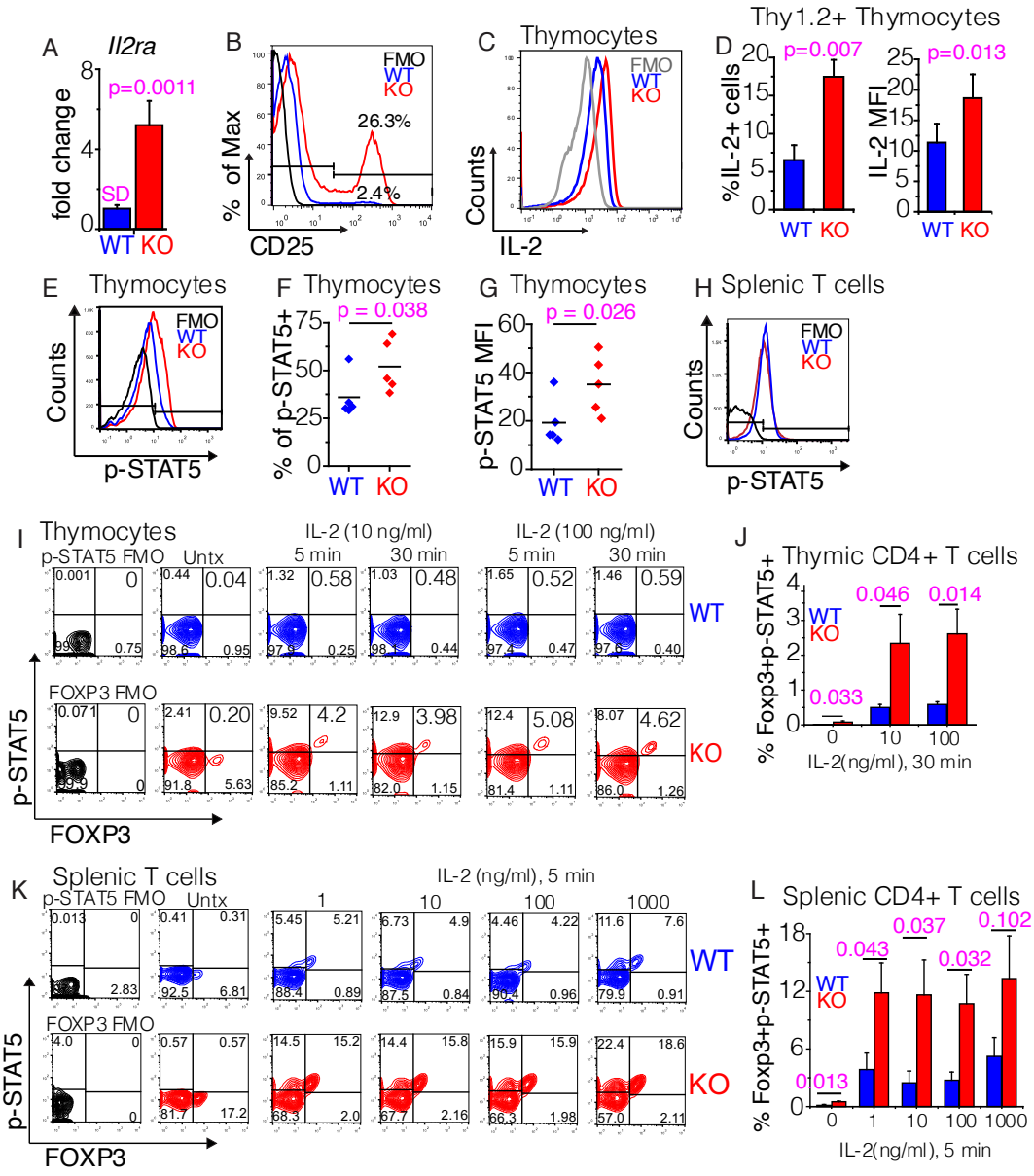
A
Il2ra
p=0.0011
fold change
SD
WT KO
B
FMO
WT
KO
26.3%
2.4%
% of Max
CD25
C
Thymocytes
FMO
WT
KO
Counts
IL-2
D
Thy1.2+ Thymocytes
p=0.007
p=0.013
%IL-2+ cells
IL-2 MFI
WT KO
E
Thymocytes
FMO
WT
KO
Counts
p-STAT5
F
Thymocytes
p = 0.038
% of p-STAT5+
WT KO
G
Thymocytes
p = 0.026
p-STAT5 MFI
WT KO
H
Splenic T cells
FMO
WT
KO
Counts
p-STAT5
I
Thymocytes
p-STAT5 FMO
Untx
IL-2 (10 ng/ml)
5 min
30 min
IL-2 (100 ng/ml)
5 min
30 min
WT
FOXP3 FMO
KO
p-STAT5
FOXP3
J
Thymic CD4+ T cells
% Foxp3+p-STAT5+
WT
KO
0.046
0.014
0.033
IL-2(ng/ml), 30 min
K
Splenic T cells
p-STAT5 FMO
Untx
IL-2 (ng/ml), 5 min
1
10
100
1000
WT
FOXP3 FMO
KO
p-STAT5
FOXP3
L
Splenic CD4+ T cells
% Foxp3+p-STAT5+
WT
KO
0.043
0.037
0.102
0.032
0.013
IL-2(ng/ml), 5 min

Figure 23. KO mouse thymocytes and splenic T cells show increased phosphorylation of STAT5 in response to IL-2.

(A) RT-qPCR analysis of the relative abundance of *Il2ra* mRNA in WT and KO thymocytes. The relative fold change was calculated after normalization to the abundance of mRNA encoding β2-microglobulin (*b2m*). The *P* value was calculated by two-tailed unpaired *t* test ($n = 3$ experiments).

(B) Flow cytometry analysis of the cell surface expression of IL-2Rα (CD25) in WT and KO thymocytes. The histogram is representative of seven independent experiments.

(C) Overlaid flow cytometry histograms showing intracellular IL-2 staining in Thy1.2$^+$ WT (blue) and KO (red) thymocytes. The gray line denotes an FMO control. The data are representative of three independent experiments.

(D) Left: Frequency of IL-2$^+$Thy1.2$^+$ thymocytes obtained from WT (blue) and KO (red) mice. Right: Bar graph of the MFI of IL-2 staining in Thy1.2$^+$ thymocytes from the indicated mice. The P value was calculated by two-tailed unpaired *t* test; error bars represent SEM ($n = 3$).

(E) Overlaid histograms show the intracellular pSTAT5 staining in Thy1.2$^+$CD4$^+$ T cells obtained from WT and KO thymocytes, as indicated. The data are representative of four independent experiments.

(F) Percentage of pSTAT5$^+$ cells (left) and pSTAT5 MFI values (right) in freshly isolated WT and KO thymocytes. The *P* value was calculated by two-tailed

unpaired *t* test ($n = 4$).

(G) MFI values of pSTAT5 in freshly isolated WT and KO thymocytes. The *P* value was calculated by two-tailed unpaired *t* test ($n = 4$).

(H) Representative histogram (of three independent experiments) showing intracellular staining of pSTAT5 in freshly isolated WT and KO splenic T cells. FMO control is shown as a black trace.

(I) Representative bivariant contour plots (of four independent experiments) showing Foxp3 and pSTAT5 staining in $CD4^+$ WT and KO thymocytes before and after stimulation with the indicated concentrations of IL-2 at the indicated times. Analysis was confined to $CD4^+$ thymocytes; for the gating strategy used, see Fig. 24C.

(J) Frequency of $pSTAT5^+$ T_{reg} cells as determined by the analysis shown in (I). Error bars indicate the SEM ($n = 4$ experiments); *P* values were calculated by *t* test.

(K) Foxp3 and pSTAT5 staining in WT and KO $CD4^+$ splenocytes before and 5 min after stimulation with the indicated concentrations of IL-2.

(L) Frequency of $pSTAT5^+$ splenic T_{reg} cells quantified from the analysis shown in (K). Error bars indicate the SEM ($n = 4$ experiments); *P* values were calculated by *t* test.

Figure 24

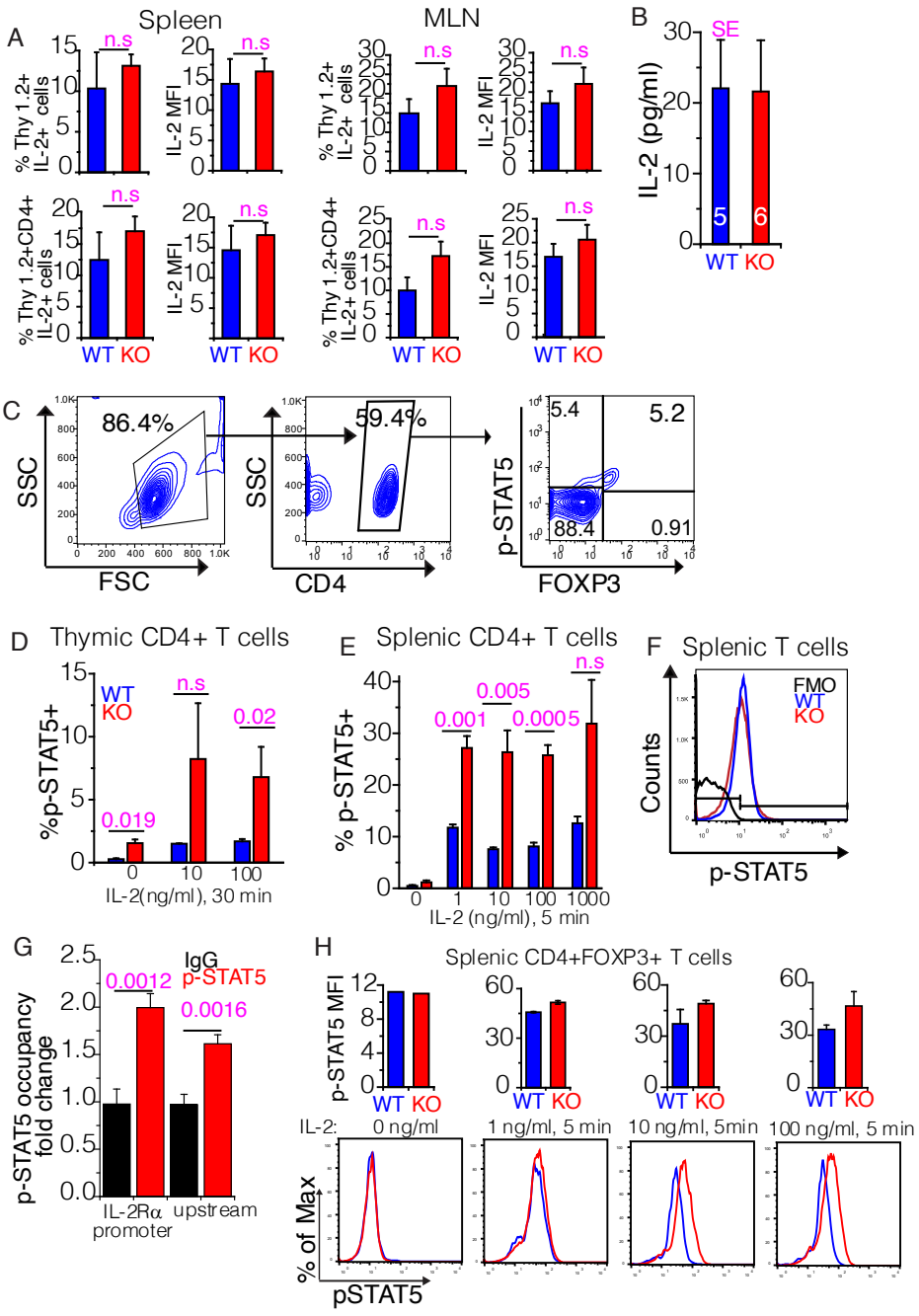
A
Spleen
MLN
% Thy 1.2+ IL-2+ cells
IL-2 MFI
% Thy 1.2+CD4+ IL-2+ cells
n.s
WT KO
B
SE
IL-2 (pg/ml)
5
6
C
86.4%
59.4%
5.4
5.2
88.4
0.91
SSC
FSC
CD4
p-STAT5
FOXP3
D
Thymic CD4+ T cells
%p-STAT5+
0.019
0.02
IL-2(ng/ml), 30 min
E
Splenic CD4+ T cells
% p-STAT5+
0.005
0.001
0.0005
IL-2 (ng/ml), 5 min
F
Splenic T cells
FMO
Counts
p-STAT5
G
p-STAT5 occupancy fold change
IgG
p-STAT5
0.0012
0.0016
IL-2Rα upstream promoter
H
Splenic CD4+FOXP3+ T cells
p-STAT5 MFI
IL-2:
0 ng/ml
1 ng/ml, 5 min
10 ng/ml, 5min
100 ng/ml, 5 min
% of Max
pSTAT5

Figure 24. Thymocytes and splenic T cells from KO mice show increased IL-2 sensitivity.

(A) The relative expression of IL-2 in T cells obtained from the spleens (left) and mesenteric lymph nodes (right) of WT and KO mice. Top: Analysis of total T cells (Thy1.2$^+$). Bottom: Analysis of CD4$^+$ T cells (Thy1.2$^+$CD4$^+$). Both the percentage of IL-2–expressing cells and the MFI of IL-2 staining are quantified. Data are from 3 experiments.

(B) Analysis of the average IL-2 concentrations, as measured by ELISA, in sera obtained from WT (5 mice) and KO (6 mice). Error bars indicate the SEM.

(C) Representative gating strategy used to analyze CD4$^+$ cells for p-STAT5 and Foxp3 expression.

(D) Percentages of p-STAT5$^+$ thymocytes as determined by the addition of the upper-left and upper-right quadrant gates from the flow cytometry analysis shown in Fig. 23I. Error bars indicate the SEM (n = 4 experiments); P values were calculated by t test.

(E) Percentages of p-STAT5$^+$ splenic T cells as determined by the addition of the upper-left and upper-right quadrant gates from the flow cytometry analysis shown in Fig. 23K. Error bars indicate the SEM (n = 4 experiments); P values were calculated by t test.

(F) Overlaid histograms show the intracellular p-STAT5 staining on T cells obtained from the spleens of WT and KO mice.

(G) ChIP-qPCR analysis of p-STAT5 occupancy on two different regions of the *Il2ra* promoter in thymocytes form WT and KO mice. The occupancy seen in thymocytes from WT mice was normalized (black bars) and the relative difference in occupancy in thymocytes from the KO mice is shown in red bars (*n*=3).

(H) Comparison of the MFI of pSTAT5 in splenic $CD4^{+}FOXP3^{+}$ T cells obtained from WT and KO mice (*n*=4). Bottom: Representative overlaid histograms of p-STAT5 staining in the indicated cells.

Figure 25

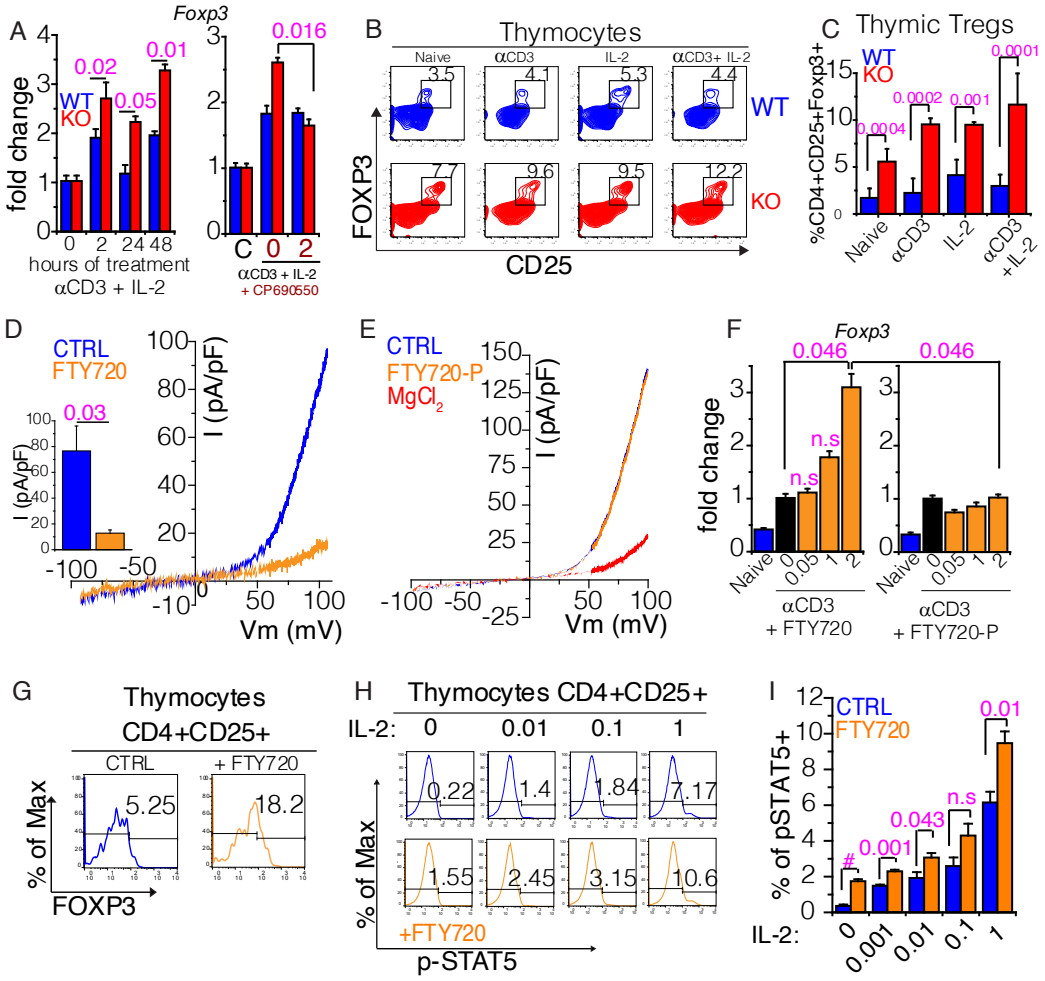
A
Foxp3
fold change
WT
KO
0.02
0.05
0.01
0.016
hours of treatment
αCD3 + IL-2
αCD3 + IL-2
+ CP690550
B
Thymocytes
Naive
αCD3
IL-2
αCD3+ IL-2
FOXP3
CD25
WT
KO
C
Thymic Tregs
%CD4+CD25+Foxp3+
0.0004
0.0002
0.001
0.0001
D
CTRL
FTY720
0.03
I (pA/pF)
Vm (mV)
E
CTRL
FTY720-P
MgCl2
F
Foxp3
0.046
n.s
fold change
αCD3
+ FTY720
αCD3
+ FTY720-P
G
Thymocytes
CD4+CD25+
CTRL
+ FTY720
5.25
18.2
% of Max
FOXP3
H
Thymocytes CD4+CD25+
IL-2:
0
0.01
0.1
1
0.22
1.4
1.84
7.17
1.55
2.45
3.15
10.6
% of Max
+FTY720
p-STAT5
I
CTRL
FTY720
0.01
0.043
n.s
0.001
#
% of pSTAT5+
IL-2:

Figure 25. *Foxp3* gene induction is enhanced by deletion or inhibition of TRPM7.

(A) Left: qRT-PCR analysis measuring the relative expression of *Foxp3* in WT and KO thymocytes activated with anti-CD3 and IL-2 at the indicated times. Right: Analysis of Foxp3 induction in KO thymocytes in the presence of 2 nM CP690550 (JAK inhibitor) at the 48-hour time point. C, untreated control. Both bar graphs denote mean values, and the error bars indicate the SEM ($n = 3$ experiments). The *P* value was calculated by *t* test.

(B) Analysis of Foxp3 and CD25 expression on $CD4^+$ thymocytes from WT (blue) and KO (red) mice after activation with anti-CD3, IL-2, or both, as indicated.

(C) Quantification of the frequencies of $CD4^+CD25^+Foxp3^+$ T_{reg} cells from the experiments shown in (B). Error bars indicate the SEM (WT, $n = 3$; KO, $n = 4$). Thymocytes were pooled from at least two mice in each experiment. The *P* values were calculated by two-tailed unpaired Student's *t* test.

(D) I-V relationship of I_{TRPM7} in WT thymocytes (blue trace) obtained by whole-cell patch-clamp recordings; orange trace shows inhibition of I_{TRPM7} after perfusion of 2 μM FTY720 in the bath solution. Inset bar graph shows I_{TRPM7} current densities for each condition, obtained 5 min after break-in at 100 mV ($n = 3$ experiments).

(E) I-V relationship of I_{TRPM7} in thymocytes during bath perfusion of 2 μM FTY720-P (S1PR agonist; orange trace). The control WT thymocyte current (blue trace) is identical to the I_{TRPM7} with perfused FTY720-P. $MgCl_2$-treated cells (10 mM, red trace) display inhibition of TRPM7 current.

(F) Quantification by qRT-PCR analysis of the relative expression of *Foxp3* in WT thymocytes activated for 48 hours with anti-CD3 antibody in the presence of the indicated concentrations of FTY720 (left) or FTY720-P (right). Error bars indicate the SEM ($n = 3$ experiments). The indicated *P* values were calculated by unpaired Student's *t* test.

(G) Representative histograms of Foxp3 staining in $CD4^+CD25^+$ WT thymocytes activated for 48 hours with anti-CD3 and IL-2 in the absence (blue) or presence of FTY720 (orange). Data are representative of three experiments.

(H) Histograms representing intracellular pSTAT5 staining. Thymocytes were pretreated with FTY720 (orange) or left untreated (blue) and then stimulated for 15 min with the indicated concentrations of IL-2. Representative data from three independent experiments are shown.

(I) Quantification of $pSTAT5^+$ thymocytes from the experiments shown in (H). Data are representative of three independent experiments, in which the cells were cultured in triplicate. *P* values were calculated by Student's *t* test ($\#P = 0.005$).

Figure 26

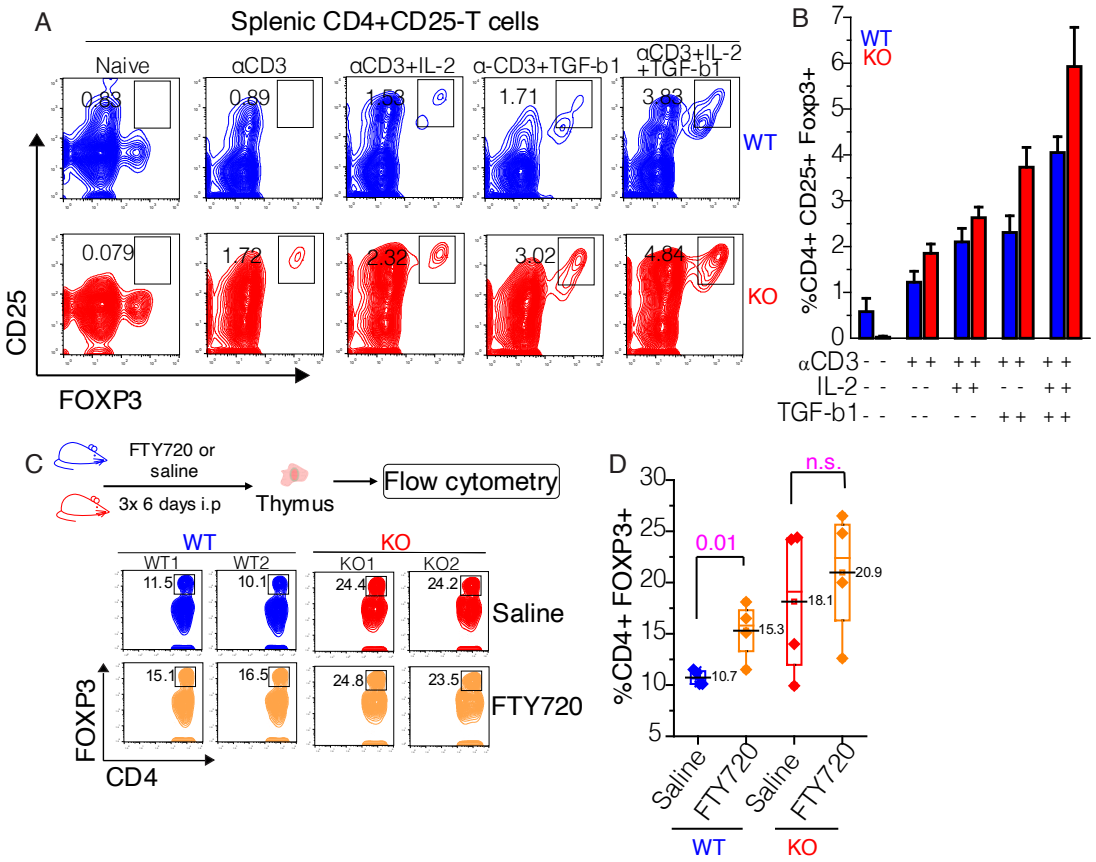
A
Splenic CD4+CD25-T cells
Naive
αCD3
αCD3+IL-2
α-CD3+TGF-b1
αCD3+IL-2 +TGF-b1
0.83
0.89
1.58
1.71
3.83
WT
0.079
1.72
2.32
3.02
4.84
KO
CD25
FOXP3
B
WT
KO
%CD4+ CD25+ Foxp3+
αCD3 - - + + + + + + + +
IL-2 - - - - + + - - + +
TGF-b1 - - - - - - + + + +
C
FTY720 or saline
3x 6 days i.p
Thymus
Flow cytometry
WT
KO
WT1
WT2
KO1
KO2
11.5
10.1
24.4
24.2
Saline
15.1
16.5
24.8
23.5
FTY720
FOXP3
CD4
D
%CD4+ FOXP3+
0.01
n.s.
10.7
15.3
18.1
20.9
Saline
FTY720
Saline
FTY720
WT
KO

Figure 26. Inhibition of TRPM7 augments *Foxp3* expression.

(A) Bivariant contour plots showing the induction of CD25 and FOXP3 expression in WT and KO splenic T cells ($CD4^+CD25^-$) in response to the indicated stimuli. The cells were initially gated for viability. Data are representative of three independent experiments.

(B) The mean percentage of T_{reg} cells ($CD4^+CD25^+FOXP3^+$) induced in the indicated culture conditions. Error bars indicate the SEM (*n* = 3 experiments). Each independent experiment used T cells pooled from three mice.

(C) Top: Experimental scheme. WT (blue) and KO (red) mice received three doses of FTY720 (0.1 μg/kg body weight; i.p.) every other day for 6 days. Bottom: Bivariant contour plots of thymocytes analyzed to quantify the number of $CD4^+FOXP3^+$ T_{reg} cells.

(D) Percentages of $CD4^+FOXP3^+$ T_{reg} cells found in the thymi of saline and FTY720 treated WT and KO mice. The mean is indicated by a horizontal line; *n* = 4 mice per treatment. The *P* values were calculated by two-tailed, unpaired *t* test.

Figure 27

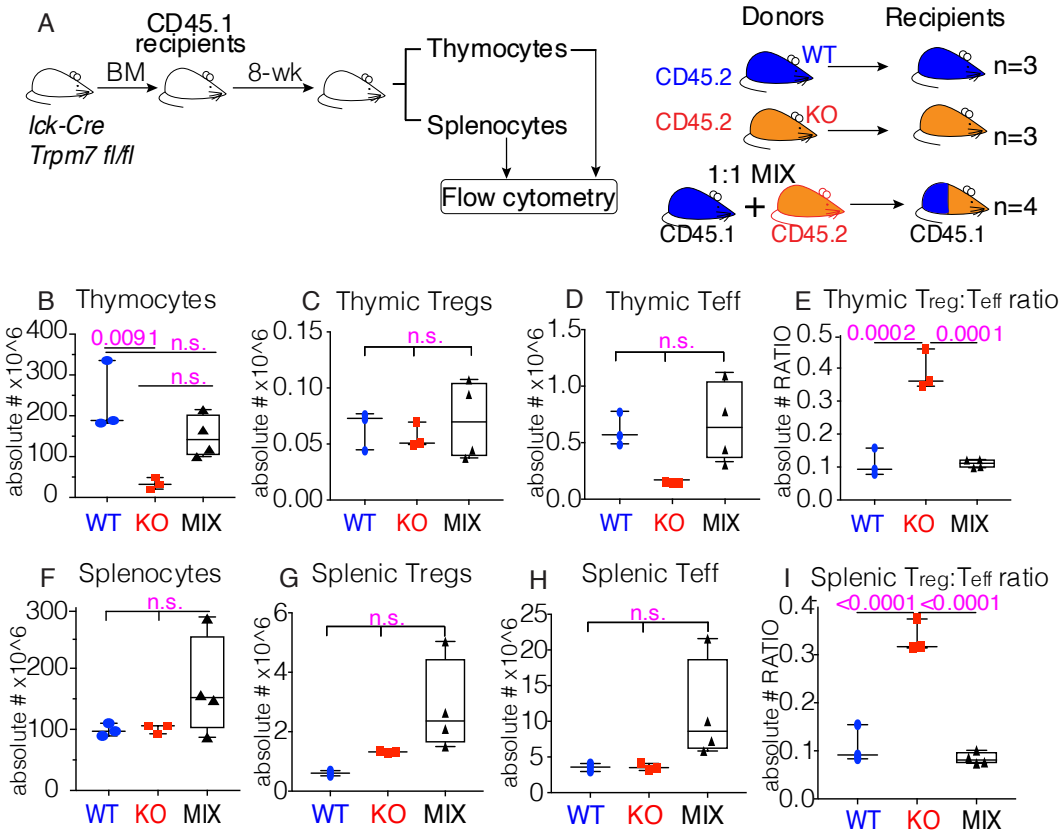
A
CD45.1 recipients
BM
8-wk
lck-Cre
Trpm7 fl/fl
Thymocytes
Splenocytes
Flow cytometry
Donors
Recipients
CD45.2
WT
n=3
CD45.2
KO
n=3
1:1 MIX
CD45.1
CD45.2
n=4
CD45.1
B Thymocytes
C Thymic Tregs
D Thymic Teff
E Thymic Treg:Teff ratio
F Splenocytes
G Splenic Tregs
H Splenic Teff
I Splenic Treg:Teff ratio
absolute # x10^6
absolute # RATIO
0.0091
n.s.
0.0002
<0.0001
WT
KO
MIX

Figure 27. KO BM chimeras suggest that the effects of *Trpm7* deletion are both cell-intrinsic and extrinsic.

(A) Experimental scheme (left) and bone marrow (BM) transplantation scenarios (right).

(B) Absolute numbers of thymocytes obtained from WT recipient mice after transplantation of BM from WT (blue), KO (red), or mixed (black) mice. The *P* value was calculated by one-way analysis of variance (ANOVA).

(C) Absolute numbers of $CD45^{+}TCRb^{+}CD4+CD25^{+}Foxp3^{+}T_{regs}$ in the thymi obtained from the indicated recipient mice (data analyzed by one-way ANOVA).

(D) Absolute numbers of $CD45^{+}TCRb^{+}CD4^{+}CD25^{-}Foxp3^{-}$ T_{effs} in the thymi obtained from the indicated recipient mice (data analyzed by one-way ANOVA).

(E) Ratio of T_{reg}:T_{eff} absolute numbers in the thymi of the recipient mice from each transplant. *P* values were calculated by one-way ANOVA.

(F) Total numbers of splenocytes resulting from the transplantation of WT (blue), KO (red), and mixed (black) BM into WT recipient mice.

(G) Absolute numbers of $CD45^{+}CD4^{+}CD25^{+}Foxp3^{+}$ T_{reg} cells in the spleens obtained from the indicated recipient mice.

(H) Absolute numbers of $CD45^{+}CD4^{+}CD25^{-}Foxp3^{-}$ T_{eff} cells in the spleens obtained from the indicated recipient mice.

(I) Ratio of the absolute numbers of splenic T_{reg}:T_{eff} cells in mice that received the indicated BM transplants. *P* values were calculated by one-way ANOVA.

Figure 28

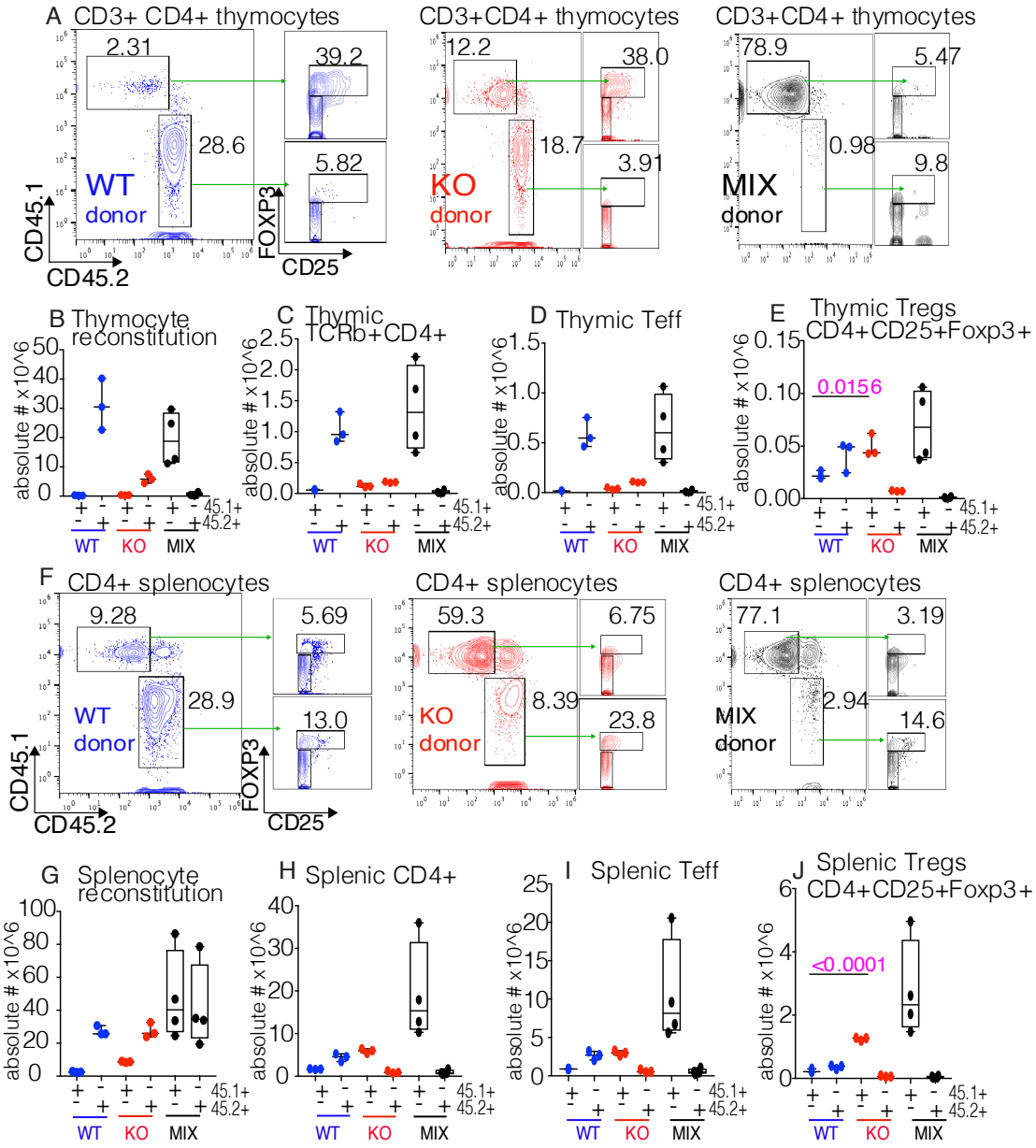
A CD3+ CD4+ thymocytes
2.31
28.6
39.2
5.82
WT
donor
CD45.1
CD45.2
FOXP3
CD25
CD3+CD4+ thymocytes
12.2
18.7
38.0
3.91
KO
donor
CD3+CD4+ thymocytes
78.9
0.98
5.47
9.8
MIX
donor
B Thymocyte reconstitution
C Thymic TCRb+CD4+
D Thymic Teff
E Thymic Tregs CD4+CD25+Foxp3+
0.0156
absolute # x10^6
45.1+
45.2+
WT
KO
MIX
F CD4+ splenocytes
9.28
28.9
5.69
13.0
CD4+ splenocytes
59.3
8.39
6.75
23.8
CD4+ splenocytes
77.1
2.94
3.19
14.6
G Splenocyte reconstitution
H Splenic CD4+
I Splenic Teff
J Splenic Tregs CD4+CD25+Foxp3+
<0.0001

Figure 28. Gating strategy and quantification of CD45.1$^+$ and CD45.2$^+$ cells from BM chimeras.

(A) Representative flow cytometry plots illustrating the frequencies and gating strategy for T_{reg} cells obtained from the thymi of recipient mice after the transplantation of WT (blue), KO (red), or mixed (black) BM cells.

(B) Quantification of the absolute numbers of thymocytes divided into CD45.1$^+$ (host) and CD45.2$^+$ (donor) populations, which visualizes the contribution of the host and donor hematopoietic cells. In the case of the mixed BM transplant, WT CD45.1$^+$ and KO CD45.2$^+$ cells were transplanted in equal ratios.

(C) Quantification of the absolute numbers of TCRb$^+$CD4$^+$ thymic T cells in the recipients of the WT (blue), KO (red), and MIX (black) transplants. The obtained T cells are plotted separately as the host (CD45.1$^+$) and donor (CD45.2$^+$) cells.

(D) Absolute numbers of thymic T_{eff} cells (TCRb$^+$CD4$^+$CD25$^-$Foxp3$^-$) resulting from each transplant, plotted separately as the host (CD45.1$^+$) and donor (CD45.2$^+$) cells.

(E) Absolute numbers of thymic T_{reg} cells (TCRb$^+$CD4$^+$CD25$^+$Foxp3$^+$) resulting from each transplant, plotted separately as the host (CD45.1$^+$) and donor (CD45.2$^+$) cells. *P* was calculated by Student's *t* test.

(F) Representative flow cytometry plots illustrating the frequencies and gating strategy for T_{reg} cells obtained from the spleens of the recipient mice after the transplantation of WT (blue), KO (red), or mixed (black) BM cells.

(G) Quantification of the absolute numbers of splenocytes divided into $CD45.1^+$ (host) and $CD45.2^+$ (donor) populations. The mixed BM condition had WT $CD45.1^+$ and KO $CD45.2^+$ hematopoietic cells transplanted in equal ratios.

(H) Quantification of the absolute numbers of all splenic $CD4^+$ T cells in the recipients of the WT (blue), KO (red), and MIX (black) transplants. T cells are plotted separately as the host ($CD45.1^+$) and donor ($CD45.2^+$) cells.

(I) Absolute numbers of splenic T_{eff} cells ($CD4^+CD25^-Foxp3^-$) resulting from each transplant, plotted separately as the host ($CD45.1^+$) and donor ($CD45.2^+$) cells.

(J) Absolute numbers of splenic T_{reg} cells ($TCRb^+CD4^+CD25^+Foxp3^+$) resulting from each transplant, plotted separately as the host ($CD45.1^+$) and donor cells ($CD45.2^+$). *P* value was calculated by Student's *t* test.

CHAPTER THREE TABLES

Table 2. Primer sequences used in the real-time qPCR experiments.

	Gene name	Forward primer sequence	Reverse primer sequence	Product size (bp)
1	*Ifng*	ATGAACGCTACACACTGCATC	CCATCCTTTTGCCAGTTCCTC	182
2	*Tnfa*	CCCTCACACTCAGATCATCTTCT	GCTACGACGTGGGCTACAG	61
3	*Il1b*	GCAACTGTTCCTGAACTCAACT	ATCTTTTGGGGTCCGTCAACT	89
4	*Il6*	TAGTCCTTCCTACCCCAATTTCC	TTGGTCCTTAGCCACTCCTTC	76
5	*Gzmb*	CTGCTAAAGCTGAAGAGTAAGGC	CACATTGACATTGCGCCTGG	78
6	*Il10*	CAGTACAGCCGGGAAGACAA	TGGCAACCCAAGTAACCCTTA	179
7	*Foxp3*	TCCTTCCCAGAGTTCTTCCAC	GGCGAACATGCGAGTAAACC	159
8	*Ctla4*	ATGGCTTGTCTTGGACTCCG	TTGGGTCACCTGTATGGCTTC	126
9	*Tgfb1*	GCTGAACCAAGGAGACGGAA	ATGTCATGGATGGTGCCCAG	138
10	*Nt5e*	GCAGCATTCCTGAAGATGCG	CTCCCGAGTTCCTGGGTAGA	88
11	*Lag3*	CCAGGCCTCGATGATTGCTA	ACGCGGTGAGTTGTAGACAG	148
12	*Entpd1*	AGGGCACTGGAGACTACGAA	AGAAAACGCCCCAAAACTCC	134
13	*Il2*	ACTAAAGGGCTCTGACAACACA	GGGCTTGTTGAGATGATGCTT	114
14	*Trpm7*	AGCAGTATTCCAATGATTTTGGC	TCATAGCCATCGTTTCATCCTGT	81
15	*B2m*	GGCCTGTATGCTATCCAGAA	GAAAGACCAGTCCTTGCTGA	198

Materials and Methods

Mice

Mice were housed and bred in accordance with policies and proto-cols approved by the Institutional Animal Care and Use Committee of the University of Virginia. Male and female mice aged between 4 and 12 weeks were used for the experiments. Trpm7fl mice, wherein exon 17 of Trpm7 is flanked by LoxP sites and Trpm7fl(Lck Cre) mice that deletes Trpm7 selectively in T cells, were described by us previously[33].

Genotyping of mice

Tail samples were dissolved at 85°C for 30 min in 75 µl of digestion buffer (25 mM NaOH and 0.2 mM EDTA), and the reaction was stopped by adding 75 µl of neutralization buffer (40 mM tris-HCl). One microliter was used as a template for PCR amplification with MyTaq Hot Start Polymerase (Bioline, #BIO-21112) and 5× MyTaq Red Reaction Buffer (Bioline, #BIO-37112). PCR products were separated in a 1% agarose gel and visualized with ethidium bromide. The presence of Cre recombinase was determined using the following primers: forward primer Cre S2F (5′-GATTTCGACCAGGTTCGTTC-3′) and reverse primer Cre S5R (5′-GCTAACCAGCGTTTCGTTC-3′). The presence (fl) or absence (WT) of LoxP sites flanking exon 17 was detected with the following primers: forward primer Geno 2F*

(5′-CAGAGGTACTGGCAATTGTG-3′) and reverse primer Geno 2R* (5′-ACGAGGACTCAGCATATAGC-3′).

Reagents

The following antibodies were used: anti-mouse Nrp-1–PE (phycoerythrin) (R&D Systems, #FAB5994P); rat anti-mouse CD25 PE-Cy7 (BD Pharmingen, #552880); anti-mouse CD39 PE-Cyanine7 (eBioscience Inc., #25-0391); anti-mouse CD73 PE (eBioscience Inc., #12-0731); rat anti-mouse CD4 FITC (fluorescein isothiocyanate) (BD Biosciences, #553046); purified hamster anti-mouse CD28 (BD Biosciences, #553294); anti-mouse/rat Foxp3 APC (allophycocyanin) clone FJK-16s (eBioscience); anti-Foxp3 (eBioscience, #17-5773); purified hamster anti-mouse CD3ε chain, clone 145-2C11 (BD Biosciences, #553058); anti-mouse CTLA-4 (CD152) PE (eBioscience, #12-1522); and anti-mouse CD16/CD32 antibody (BioLegend, TruStain fcX, #101320). The following sets of magnetic beads were used for T cell isolation: Dynabeads Untouched Mouse T Cells (Life Technologies, #11413D), CD4+ CD25+ Regulatory T Cell Isolation Kit, mouse (Miltenyi Biotec, #130-091-041), and Dynabeads FlowComp Mouse CD4+ CD25+ Treg Cells (Life Technologies, #11463D). We used the SensiMix SYBR Kit (Bioline USA Inc., #QT605-20), GoScript Reverse Transcription System (Promega Corporation, #A5001), and the ISOLATE II RNA Mini Kit (Bioline, #BIO-52073).

Human TGF-β1 was obtained from Cell Signaling Technology (#8915), and recombinant human IL-2 was from BD Biosciences (#BDB554603). CFSE was from Life Technologies, γ-irradiated Con A from *Canavalia ensiformis* was from Sigma-Aldrich, FTY720 was from Cayman Chemical, and 7-Aminoactinomycin D (7-AAD) was from BD Biosciences (#559925).

Con A–induced hepatitis model

Age- and sex-matched WT and KO mice were weighed 2 hours before injection to control for body weight differences. Con A (40 mg/kg) or phosphate-buffered saline (PBS) was administered intravenously through tail vein injection. Animals were monitored for 24 hours after injection. Animals were euthanized at the times indicated in the figures or at 24 hours. Blood was collected by cardiac puncture for the measurement of serum ALT in a blinded manner.

Serum ALT measurements

Blood was collected from mice by cardiac puncture and centrifuged at 1500g at 4°C for 10 min to collect serum. Samples with signs of hemolysis were discarded. Sera were preserved at −80°C and analyzed within 48 hours of collection. ALT activity was detected with the Liquid ALT (SGPT) Reagent Kit (Pointe Scientific Inc.) according to the manufacturer's instructions.

Histology

After perfusion with PBS, a portion of liver tissue was fixed by immersion in 4% paraformaldehyde (PFA) for 24 hours and transferred to 30% sucrose for 24 hours before tissue analysis. Tissue embedding, sectioning, and mounting were performed by the UVA Research Histology Core (University of Virginia, Charlottesville, VA). Tissues were embedded in frozen tissue blocks before sectioning. Hematoxylin and eosin (H&E) staining was performed by the UVA Research Histology Core, and slides were photographed and analyzed on an Aperio ScanScope (Leica Biosystems).

Immunofluorescence microscopy

Liver tissue sections were prepared on slides, rehydrated in water, washed with PBS and 0.05% Tween 20, and permeabilized for 15 min with PBS containing 0.1% Triton X-100. Slides were then blocked with blocking buffer [PBS with 1% bovine serum albumin (BSA), 0.1% fish gelatin, 0.1% Triton X-100, 0.05% Tween 20, and 5% animal serum, corresponding to the host species of the secondary antibody]. Slides were stained with rat anti-mouse CD4 (1 μg/ml; clone RM4-5, BioLegend) in blocking buffer overnight at 4°C. Slides were then washed three times in wash buffer and stained with Alexa Fluor 594–conjugated goat anti-rat secondary antibody (0.2 μg/ml; Life Technologies) and solubilized in blocking

buffer for 2 hours at room temperature. After being washed three times, the cells were stained with Hoechst 33342 nuclear dye (0.2 μg/ml) for 10 min at room temperature. Last, the slides were washed twice and coverslips (Fisherbrand, 22 mm #1) were mounted over VectaMount mounting medium (Vector Laboratories). Mounted samples were cured overnight at room temperature and imaged within 24 hours. All images were captured on a Zeiss AxioObserver microscope with a Zeiss 40× (1.3 NA) objective lens and Hamamatsu CMOS ORCA-Flash4.0 sCMOS camera. Images were then processed with National Institutes of Health (NIH) ImageJ software.

Scanning electron microscopy

Livers were perfused through the portal vein with 2.5% glutaraldehyde and 4% PFA in PBS at a constant flow rate (1 ml/min). Liver sections of 5-mm thickness were removed and immersed in 2.5% glutaraldehyde and 4% PFA for 48 hours at 4°C. Samples were then washed in osmium tetroxide (OsO_4) and dehydrated in an ethanol series before critical point drying. Samples were then mounted on aluminum studs and sputter-coated in gold/palladium before being subjected to SEM on a Zeiss Sigma VP HD field-emission SEM microscope (Carl Zeiss AG) at 3 kV.

Isolation of intrahepatic immune cells

Livers were perfused with PBS through the portal vein. A portion of the liver was removed for immunohistological, immunofluorescent, and qPCR analysis. PBS-perfused livers were excised, washed in Iscove's modified Dulbecco's medium [with 10% fetal bovine serum (FBS)], and digested in 0.05% collagenase (Collagenase IV, Sigma-Aldrich) for 25 min at 37°C.Mononuclear cells (MNCs) containing immune cells were purified with a 40% Histodenz (Sigma-Aldrich) gradient after centrifugation at 1500g for 20 min at 4°C. Spleens, thymi, and lymph nodes were physically disrupted in cold, sterile RPMI 1640. Cell suspensions were filtered through 70-μm nylon mesh, and contaminating erythrocytes were lysed with ACK buffer [150 mM NH_4Cl, 10 mM $KHCO_3$, and 100 μM Na_2EDTA (pH 7.3)]. These cell suspensions were then subjected to appropriate magnetic separation to isolate different subsets. We followed the protocols included in these kits: Dynabeads Untouched Mouse T Cells (Life Technologies, #11413D), $CD4^+$ $CD25^+$ Regulatory T Cell Isolation Kit, mouse (Biotec, #130-091-041), and the Dynabeads FlowComp Mouse $CD4^+$ $CD25^+$ Treg Cells (Life Technologies, #11463D).

Flow cytometry

Erythrocyte-free, single-cell suspensions isolated from livers, spleens, or thymi were processed in FACS (fluorescence-activated cell sorting) staining buffer

composed of 150 mM PBS, 0.5% BSA, and 2 mM EDTA. Fc receptors on the cells were blocked with anti-mouse CD16/CD32 antibody (BioLegend, TruStain fcX, #101320) for 20 min and then stained with fluorochrome-conjugated antibodies. For intracellular staining of Foxp3, the cells were fixed in 1% PFA and permeabilized with 0.1% saponin. Intracellular staining of pSTAT5 was performed after concomitant fixation and permeabilization with 100% methanol. The stained cells were analyzed with a FACSCalibur or LSRFortessa flow cytometer (Becton Dickinson). The data were acquired by CellQuest Pro Acquisition software or FACSDiva version 6 software (Becton Dickinson), respectively. Every experiment included single-stain and “fluorescence minus one” (FMO) controls to facilitate accurate compensation and analysis with FlowJo version 10 software (Tree Star).

T cell activation, CFSE proliferation assay, and transwell migration assay

T cells were cultured at a density of 0.5×10^6 cells/ml in a culture volume of 200 µl per well in 96-well round-bottom plates. The cells were activated with Con A (5 µg/ml) for 48 hours or as indicated in the figure legends. Alternatively, cells were activated with a mixture of anti-CD3e (2.5 µg/ml) and anti-CD28 (1 µg/ml) for 48 hours. After activation, cells or the cell culture medium was harvested for analysis. For CFSE proliferation assays, the T cell subsets were cultured at a reduced density (50,000 cells per well) in 96-well round-bottom plates. Proliferation was

then stimulated with a mixture of anti-CD3e (0.25 μg/ml) and anti-CD28 (0.125 μg/ml), and analysis was performed after 3 days of culture. For transwell-based migration assays, each transwell (5.0 μm pore size membrane) from Corning Costar Incorporation contained 5×10^5 splenic T cells from WT or KO mice suspended in 100 μl of complete medium (top chamber). Transwell inserts were placed in a 24-well tray containing 600 μl of variably diluted conditioned medium containing chemotactic signals secreted by LPS (lipopolysaccharide)–treated BM-derived macrophages (BMDMs). During the incubation of the transwell plates (16 hours at 37°C, 5% CO_2), the T cells transmigrated to the bottom chamber. They were manually counted using trypan blue. Data are presented as a percentage of the T cells that migrated across the membrane.

Luminex multiplex assay and ELISA

Cell culture supernatants were thawed from −80°C and analyzed in duplicate to measure cytokine concentrations. The data were acquired and analyzed with the Luminex multiplex assay (Luminex 100 IS). Standards were assayed for each cytokine with QC1 and QC2 in duplicate with bead counts of <25. The cytokine concentrations were calculated by curve-fitting five concentrations of standards. ELISAs were performed according to the manufacturer's instructions.

Real-time qPCR analysis

The concentrations of total RNA isolated from cells with the ISOLATE II RNA Mini Kit (Bioline, #BIO-52073) were measured with a NanoDrop 2000c spectrophotometer (Thermo Scientific). The complementary DNA (cDNA) was reverse-transcribed with the GoScript Reverse Transcription System (Promega, #A5001). The qPCR experiments were always set in triplicate with SensiMix SYBR Hi-ROX Kit (Bioline, #QT605-05) in a CFX Connect real-time system (Bio-Rad). After 40 cycles of PCR amplification, the data were analyzed with CFX Manager 3.1 software (Bio-Rad). The primers used for qPCR analysis are shown in table S1. Data were analyzed with the ΔΔCt method[155] using the average Ct values of β2-microglobulin (*b2m*) to normalize for cDNA input error. Statistical analysis was based on three independent experiments.

ChIP assays

Equal numbers of freshly isolated thymocytes from WT and KO mice were cross-linked with 1% formaldehyde for 10 min before the cross-linking reaction was stopped with the addition of glycine. The cytoplasmic contents were extracted and removed with cell lysis buffer containing 1% SDS. The nuclear pellets were resuspended in ChIP buffer (1.1% Triton X-100 containing nuclear lysis buffer). These nuclear pellets were subjected to sonication with a Bioruptor Pico

(Diagenode Inc.). The sheared chromatin was then immunoprecipitated for 12 hours at 4°C with ChIP-grade antibodies [anti-pSTAT5 (Tyr694) and control IgG] and ChIP-grade protein G magnetic beads (Cell Signaling Technology). The immunoprecipitated samples were then eluted with ChIP elution buffer and treated with proteinase K for 12 hours at 65°C to release the DNA fragments. The released DNA was purified with a column-based DNA purification kit (Qiagen) and subjected to qPCR with the following primers. For Il2ra promoter site 1, forward: TGACAGACTGAGAGGCCTGA; reverse: TGGGTCAACCCCTTTACTGC. For Il2ra promoter site 2, forward: TTTGACGTCGGGTGTCTTCC; reverse: GTGGAACTCTGGGTTCAGCA. The data were then analyzed to assess the occupancy of STAT5 on Il2ra promoters in KO thymocytes relative to that in WT thymocytes. Briefly, the Ct values obtained from mock IgG ChIPs were first used to calculate the fold change in anti-STAT5 ChIPs in WT and KO samples. The KO STAT5 ChIPs showed significantly higher fold-change values compared to those in the WT samples. These are shown as bar graphs after normalizing the WT values to 1.

Ca^{2+} imaging in T cells

The cells were loaded with Fura-2 AM, and the recording was performed in 2 mM $CaCl_2$. The baseline was recorded in the presence of biotinylated anti-CD3e

antibody, and the Ca^{2+} response was observed by adding streptavidin. Ionomycin (Ca^{2+} ionophore) served as a positive control. The 340/380-nm fluorescence ratio was back-ground-subtracted and normalized to baseline ($\Delta F/F0$). The rise time (tau) of fluorescence was derived and plotted. The number of cells assessed is outlined in the figures. Ca^{2+} imaging data were collected on a Zeiss Axio Observer microscope with Zeiss 40× [1.3 numerical aperture (NA)] objective lens and a Hamamatsu CMOS Orca-Flash 4.0 sCMOS camera.

Electrophysiology

The TRPM7 current (I_{TRPM7}) was measured in the whole-cell configuration (Fig. 20F). T cells were activated with a mixture of anti-CD3e and anti-CD28 antibody (or Con A) and cultured in 96- well plates at 37°C, 5% CO_2 for 1 to 4 days before being subjected to patch-clamp electrophysiology. The standard external solution contained the following: 135 mM sodium methanesulfonate (Na-$MeSO_3$), 5 mM cesium gluconate, 2.5 mM $CaCl_2$, and 10 mM HEPES (pH 7.3, adjusted with NaOH); osmolality, 280 to 290 mOsm/kg. The standard pipette solution contained 110 mM Cs-gluconate, 0.5 mM NaCl, 0.75 mM $CaCl_2$, 10 mM HEPES, 10 mM HEDTA, 1.8 mM Cs_4-BAPTA, and 2 mM Na_2ATP (pH 7.3, adjusted with CsOH). Osmolality was 273 mOsm/kg, and the calculated free [Ca^{2+}] = ~100 nM. We used the MaxChelator algorithm to calculate free Ca^{2+}: https://so-

mapp.ucdmc.ucdavis.edu/pharmacology/bers/maxchelator/webmaxc/webmaxcS.htm. FTY720 (2 μM) or $MgCl_2$ (10 mM) was used in the external solution to inhibit TRPM7 currents. All currents were re-corded with an Axopatch 200B amplifier (Molecular Devices). The recording protocol consisted of 400-ms ramps from −100 to +100 mV and a holding potential (HP) of 0 mV. The signals were low-pass–filtered at 5 kHz and sampled at 10 kHz. All electrophysiology experiments were performed at room temperature (~22°C). The average current densities were plotted with the relevant statistical information as a box chart.

T_{reg} cell-based suppression assay

Splenic cell suspensions were isolated from WT and KO mice. T_{eff} or T_{reg} cells were then isolated by negative and positive magnetic selection with Dynabeads FlowComp Mouse $CD4^+CD25^+$ Treg Cells Kit (Life Technologies). T_{eff} cells were labeled with 5 μM CellTrace CFSE for 20 min, washed, and cultured in RPMI 1640 medium supplemented with 2 mM l-glutamine, 10% FBS, 50 μM β-mercaptoethanol, 1% sodium pyruvate, 5 mM HEPES, penicillin (100 U/ml), and streptomycin (100 μg/ml). The CFSE-labeled T_{eff} cells were cultured in 96-well round-bottom plates and stimulated with a mixture of anti-CD3e and anti-CD28 antibodies in 5% CO_2 humidified incubator at 37°C for 3 days. The number of T_{eff} cells was kept constant at 5×10^4 cells per well, whereas the number of co-cultured

T_{reg} cells varied to generate the ratios indicated in the figures. On day 4, the cells were collected and stained for 7-AAD, CD4, and CD25 before undergoing flow cytometry analysis on a FACSCalibur instrument. The data were analyzed with FlowJo software and represented as the percentage of T_{eff} cells showing proliferation-induced dilution of the CellTrace CFSE dye. This parameter reflects the percentage of cells undergoing cell division.

Ex vivo generation of T_{reg} cells from thymocytes

Thymocytes were isolated from WT and KO as single-cell suspensions and cultured in X-VIVO 15 growth medium (Sartorius Biotech, catalog no. 04-744Q) supplemented with penicillin (100 U/ml) and streptomycin (100 μg/ml). Thymocytes were activated for 48 hours with anti-CD3ε antibody in the presence of recombinant human IL-2 (10 ng/ml) in 96-well round-bottom plates at 5% CO_2, 37°C. The thymocytes were then collected and were either used to isolate mRNA for Foxp3 mRNA analysis by qPCR or analyzed by flow cytometry for immunophenotyping and staining for intracellular Foxp3.

BM transplantation

BM was harvested from adult mice (12 to 15 weeks of age), and the cells were counted. Equal numbers of the BM hematopoietic cells from the WT and KO mice

were transplanted into the lethally irradiated (1000 cGy) syngeneic recipients, which expressed the CD45.1$^+$ marker for the ease of differentiation between the donor and the recipient cells. The recipient mice were allowed to recover for 8 weeks, which also enabled the hematopoietic cells to repopulate the periphery. Mice were then euthanized, and the thymi and spleens were collected for further analysis.

Statistical analysis

Box charts were plotted using data analysis and graphing software Origin Pro 9.1.0 (OriginLab). Statistical box charts are shown as boxes (range of 25th to 75th percentile), whisker bars (1st to 99th percentile), and data overlap. Each data point including outliers is shown along with the median (horizontal lines) and the arithmetic mean (empty squares). All data points including outliers are shown with the median (horizontal lines) and mean (empty squares) in the box. *P* values were calculated using a two-tailed unpaired Student's *t* test and as shown in each figure. Sample size equals the number of data points shown in the box charts.

Author Contributions

Conception: SKM, BND, TJB; Research Design: SKM, BND, MES; The study was spearheaded by SKM; Revised and completed by MES, Experimental execution:

SKM, MES, MSS, EKM, JKK, JSR, EJS, CAP, JSAP; Data analysis: SKM, MES; Technical assistance: EJS, JKK, JSR; Manuscript writing: SKM, MES, BND with inputs from MSS, JSAP; Project Administration: BND

CHAPTER FOUR: DISCUSSION AND FUTURE DIRECTIONS

The above studies outlined in Chapter Two and Chapter Three describe several observations pertinent to the role of TRPM7 chanzyme in the core functions of immune cells. Although TRPM7 expression in immune cells is relatively high, its functions in immune responses were not well-understood. By creating the conditional knockout models *Trpm7*$^{fl/fl}$*LysM-Cre* and *Trpm7*$^{fl/fl}$*Lck-Cre*, we gained an advantage in assessing TRPM7 activity in an *in vivo* setting for myeloid cells and T cells, respectively. We unravel two distinct modes of immunomodulation: first, in macrophages, where TRPM7 biological function orchestrates cytoskeletal and membrane dynamics for efficient phagocytosis of fungi and second, in T cells, where it affects T cells and T_{reg} development, altering the immune tolerance. Herein, I address some of the outstanding questions in the field, together with implications arising from the above studies, which will be the subject of future explorations.

Chapter Two study presents TRPM7 as a key modulator of efficient phagocytosis of fungal particles. We concede that the specific molecular mechanism, through which TRPM7 is activated remains unclear, nevertheless the study implicates the chanzyme's dual activity in the process. We report the electrical activity of TRPM7 at early stages of phagocytosis. Importantly, TRPM7-

dependent and FTY720-sensitive engulfment-triggered current (ETC) does not develop in KO macrophages. The data derived from engulfment assays and Ca^{2+}-imaging experiments imply that both activities of TRPM7 may rely on PLC activity. TRPM7 kinase interacts with PLC and PIP_2 modulates the channel activity. This should position TRPM7 downstream of PLC activation. However, the soluble yeast ligands, which normally lead to robust Ca^{2+} influx and also activate PLC, as verified in our previous studies[68], do not lead to any current development, therefore TRPM7 activation additionally appears to require physical contact. Interestingly, a study found that the membrane phosphatidylserine (PS) and phosphatidylinositol 4,5-bisphosphate (PIP_2) seem to undergo nanoclustering in response to changes in membrane potential, which did not affect other anionic phospholipids, such as phosphatidic acid (PA) or phosphatidylinositol 3,4,5-trisphosphate (PIP_3)[156]. The contents of this work lack detailed insights into the local changes in membrane potential, but it is expected from the potent Ca^{2+} influx observed in macrophage stimulation with yeast ligands. Interestingly, we recorded large TRPM7-independent macrophage Ca^{2+} fluctuations when presented with zymosan (*S. cerevisiae* cell wall extract; Fig.9) and lower Ca^{2+} peaks in live *S. cerevisiae*-stimulated macrophages, whose sustainability, in contrast seem to be TRPM7-dependent. We are currently uncertain how this difference arises; however, we propose a model. The first obvious difference between the two ligands is the particle size: on average zymosan particle is ~3 μm[88], whereas a live yeast ~5-10

μm[89]. In our study we confirmed that there is a size dependence to TRPM7 functions in engulfment, especially prominent in phagosomal sealing (Fig. 11), which implies TRPM7-dependent myosin-II regulation. Secondly, live yeast present ordered layers with mannoproteins (30-50% of dry yeast wall) exposed on its outermost layer, followed by β-glucans (50-60%) and chitin (1-2%)[157]. This could alter the sequence of responding receptors and trigger those recognizing mannoproteins first, for example: mannan-binding lectin (MBL) in plasma, mannose receptors, CR3 (binding O-mannan), galectin 3 (β-mannosides). Zymosan is a potent activator of TLR2 and Dectin-1 signaling[55,56,81,82,158]. Additionally, some receptors require FcγR cooperation for signaling, such as mincle (α-mannosyl residues) and Dectin-2 or Dectin-3 (α-mannans)[159] and for a number of these there is no recognized intracellular signaling, yet they are implicated in phagocytosis through binding of yeast ligands. FcR and Dectin-1 are examples of ITAM or ITAM- like containing receptors, which via Syk/PLC route mobilize the SOCE response. CR3 (also known as integrin αM, Mac-1 or CD11b), participates in yeast recognition by binding complement component iC3b or, in collaboration with Dectin-1, β-glucans. CR3-Dectin-1 cooperation induces Syk/JNK/AP-1 cytokine responses to stimulated adaptive immunity[160]. In CR3-deficient murine macrophages, recognition of *C. albicans* released reduced number of TGF-β1-transporting vesicles[161], whose release is also Ca^{2+} dependent. TRPM7 KO macrophages displayed normal mRNA expression of the main

receptors binding yeast ligands (Fig.6), which further implicates the chanzyme's activity, rather than developmental expression deficiency.

TRPM7 shows higher selectivity for Zn^{2+} over Ca^{2+} ions and Zn^{2+} is an important trace element, displaying antimicrobial effects in the clinic and in animal models[162]. Interestingly, some mycobacteria gained a survival advantage by expressing a P1-type ATPase, which regulates the efflux of heavy metals, neutralizing the toxic effects of Zn^{2+} ions[163]. Another study directly showed the lowered *C. albicans* load in Swiss albino mice supplemented with 3 mg/kg Zn-acetate intraperitoneal injections[164]. However, there is no clear consensus on the Zn^{2+} influence in phagocytosis, possibly due to the use of different animal models and microbial challenges. Performing a series of engulfment assays with zinc supplementation ($ZnCl_2$) and chelation (TPEN) in our study would address this issue. Abiria *et al*[165], found TRPM7-rich intracellular vesicles to be loaded with Zn^{2+} and glutathione, which release their contents during oxidative stress stimulus and attenuate oxidation-induced cell damage. Production of reactive oxygen species (ROS) is one of the major defenses against yeast pathogens. However, we did not assess the ROS-mediated killing in our study, because the killing of pathogens was independent of TRPM7. Attenuating oxidative damage may be important in the later stages during restoration of tissue homeostasis and may bear higher significance in *in vivo* setting. In future studies we aim to address TRPM7-dependent Zn^{2+} fluxes and Zn^{2+} dynamics in macrophages in responses to various

phagocytic cargo, which could also partially address the intracellular, Zn^{2+}-rich vesicles dynamics. Fluozin-3-AM is a commercially available ester dye, which detects intracellular Zn^{2+} and is unperturbed by Ca^{2+} ions to concentrations reaching 1 μM. To avoid loading or specificity artifacts, a genetically engineered Zn^{2+} probes, like eCALWY-4 or ZnGreen-1 can be used in a cell line for more sophisticated imaging.

During phagocytosis there are molecular forces that are at play in regard to the engulfed cargo and the phagocyte. A comprehensive model was proposed by Jaumouillé and Weaterman[166] wherein the protrusive forces, created by actin polymerization and receptor-particle engagement forming the phagosome, work against the membrane and cortical tension of the cell. Beyond the immunology literature, TRPM7 often displays mechano- and sheer-stress sensitivity[167–169], which in the context of our study, poses a fascinating possibility for TRPM7 involvement in the intramolecular membrane force-dynamics. Recently, Arp2/3-dependent F-actin nucleation was shown to exert constrictive forces around the phagosome with contractile myosin-II displaying crucial roles in the phagosome closure[91]. Inhibition of myosin-II, however, did not show the uptake deficiency, but rather “stalled” the phagocytic cups. In TRPM7- deficient macrophages both, inefficient engulfment and increased incidence of open phagocytic cups take place, suggesting that the ion channel and the kinase activities of TRPM7 contribute to the observed phenomenon. Myosin-IIA is one of the recognized substrates of

TRPM7 kinase domain[42,60] and *Trpm7*-KO macrophages display aberrant myosin-IIA distribution (Fig.13). 2D microscopy techniques laid out the fundamentals of cellular cortical forces that drive the cell morphological changes and structure formation during phagocytosis. In particular, the work from Grinstein lab studying frustrated phagocytosis set the stage for identifying molecules engaging in efficient uptake of opsonized targets[93,170]. This technique combined with traction force microscopy was subsequently used by many[92,171] to measure forces at the cell-target interface. Myosin motors, Arp2/3 actin nucleators, β_2-integrins, focal adhesion proteins and talin surfaced as targets regulating the molecular machinery powering the extension and closure of the phagocytic cups. These findings were put to the test by a recently published work[91], in which the authors combined lattice light sheet microscopy (LLSM) with microparticle-traction force microscopy (MP-TFM) to reenact phagocytic process and measure the contractile forces in 3D. Arp2/3-dependent nucleation sites were referred to as “teeth” protruding into the target, while the myosin-II filaments, denoted as “jaw”, and overlooked by previous studies, were shown to be key in target constriction. This technique applied to TRPM7 KO macrophages would provide useful mechanistic insights into the myosin filaments regulation by TRPM7 during the phagocytic process.

Currently, the lack of specific TRPM7 agonists hindered our investigation into the potential pharmacological benefits of increasing TRPM7-driven engulfment. Expression of TRPM7 without the kinase domain, which enhances the

channel current, leads to increased cell death, possibly due to aberrant protein folding. Analogously, the homozygous mice with the deleted C' terminus are also embryonic lethal[172], phenocopying the global deletion of TRPM7. Identifying molecules specifically targeting and potentiating TRPM7 activity would advance the molecular investigation into its functions in immune cells.

Chapter Three describes serendipitous discovery showing that targeting TRPM7 activity promotes the development of regulatory T cells (T_{regs}). Previous work[33] from Clapham lab showed that TRPM7 plays important roles in T cell development. *Trpm7^{flfl}Lck-Cre* conditional KO mice led to defective thymopoiesis, displayed a higher proportion of CD4-CD8- (double negative; DN) cells. The analysis of the surface markers CD44 and CD25 revealed a significant block in the DN3 stage (CD44-CD25+), wherein the authors observed a significant inability of T cells to downregulate CD25, without alteration of TCR-β surface expression. However, *Trpm7^{flfl}Lck-Cre* T cells are also resistant to Fas-induced apoptosis[39], but the animals instead of harboring a lymphoproliferative phenotype display lymphopenia. The mechanistic means of T_{reg} development are still largely unknown. The current model assumes a two-step induction process: first, the CD4 single positive (SP) cells receive a high affinity signal from the medullary thymic epithelial cells (mTEC), and second, the exposure to IL-2 or IL-15 induces Foxp3 expression that defines Tregs[122,173]. The role of Ca^{2+} signals in developmental steps also remains undefined, but peripheral T cells studies show that Ca^{2+} is an

indispensable signal in key T cell sustainability and functions[174,175]. The affinity with which TCR binds to self-antigens, presented by mTECs during negative selection in the thymus is the basis for their apoptotic cell death (if they are binding with high affinity). Therefore, the modulation of Ca^{2+} dynamics, key in antigenic TCR stimulation, possibly drive such signals, which duration and kinetics may prove to be essential during this process. During the bone marrow (BM) transplantation study, we observed the BM transplantation from *Trpm7$^{fl/fl}$ Lck-Cre* donor mice into the WT recipients mirrored the thymic phenotype of the KO mice and increased T_{reg} ratio (Fig. 27), however no structural alteration, nor increased T_{reg}:T_{eff} ratio was observed in the mixed BM chimeras. It would be interesting to test whether the soluble factors secreted by the TRPM7-deficient T cells, aberrant T cell-mTEC interaction or the fact that there is more T cell death are the cause of such structural thymic alteration. The answer to such questions would lead to better understanding of what signals are essential in shaping the proper thymocyte development.

The reports considering the context of ion channel signaling so far are most focused on the potent Ca^{2+} responses from the intracellular stores (SOCE). In our study, we also observe important regulation of T cell functions through TRPM7 activity. Just by a pharmacological inhibition of TRPM7[78] with an FDA-approved immunosuppressive drug, FTY720, we observe an increase in T_{reg} numbers (Fig. 25 and Fig. 26). FTY720 (fingolimod) is a pro-drug, an analog of sphingosine-1-phosphate (S1P) that is currently used in clinic to treat patients with relapsing

multiple sclerosis[176–178]. There is a growing interest to repurpose the immuno-suppressive capabilities of FTY720 and target other diseases, like Alzheimer's Disease[179,180] (FTY720 crosses blood-brain barrier), hence recognizing the molecular targets, which are affected by its biological activity are of clinical importance. FTY720 is phosphorylated by sphingosine kinase 2 (SK2) to its bioactive form and then acts as an agonist for sphingosine-1-phosphate (S1P) receptors[181], but the phospho-FTY720 does not inhibit TRPM7[62]. In lymphocytes, S1PRs are internalized, and this inhibits autoreactive lymphocytes egress from the secondary lymphoid organs, reducing their circulating numbers and attenuating the inflammation and tissue damage. We observe potent, inhibitory effects of biological functions of FTY720 in both T cells and macrophages that seem to be TRPM7-dependent because they phenocopy the outcomes observed in the TRPM7-deficient cells. However, we fully do not understand the mechanism by which FTY720 inhibits TRPM7 and to what degree what we observe in the *in vivo* models is presented by the action of blocking the TRPM7 channels or rather attributable to S1PR inverse agonism. S1PR (subtype 1) is a GPCR that exclusively couples to $G_{i/o}$ that inhibits adenyl cyclase and activates PLC, leading to Ca^{2+} mobilization. Other S1PR subtypes (2-5) can either couple to $G_{i/o}$, $G_{12/13}$ or G_q[182], so it is possible that TRPM7 also exerts broader regulation of GPCR signaling.

Macrophages, as well as T cells functions depend on cytoskeletal rearrangements. Actin dynamics at the T cell immunological synapse are important in antigen scanning and targeted delivery of secreted effector molecules[183]. Loss-of-function mutations in actin regulatory proteins in patients render immune deficiencies, collectively called “actinopathies”, which mainly present as impairment in cytotoxicity by T_{eff} cells. Interestingly, TRPM7 has been previously implicated in cytoskeletal regulation, mainly because its kinase phosphorylated the cytoskeletal constituents, like myosin-IIA[42] fibers or Annexin A1[41] *in vitro*. T cell cytotoxicity is widely measured by the production of IFNγ, however recent literature suggests that it may not correlate with the T_{eff} cytotoxic potential [184]. Cytotoxic T cells ($CD8^+$) are antigen-specific and display MHC-I restriction. Unifying the cytotoxic responses, for example by breeding OT-I mice (ovalbumin; $OVA_{257-264}$-specific $CD8^+$cells) into a *Trpm7*$^{fl/fl}$ *Lck-Cre* background and *Trpm7*$^{fl/fl}$ controls would provide a platform to assess the T_{eff} cytotoxic killing potential in the *in vivo*, as well as *in vitro* models, where $OVA_{257-264}$ is injected or transfected into cells. Studying TRPM7 function in different immune cell responses helps us understand its molecular regulation and activities.

Beyond phagocytosis, autophagy or self-eating is another lysosomal delivery pathway that requires local branched-actin nucleation and Ca^{2+} signals for efficient fusion to the lysosomes. Autophagy is activated during various cell stresses, for example, nutrient deprivation, sensing of damaged organelles,

infection with intracellular pathogens, or ER stress. In Apendix 1, I describe and summarize the preliminary data suggesting TRPM7 is a regulator of the efficient autophagic flux. Collectively, our investigation into the roles of TRPM7 in immune cells, places it in the center of efficient endocytic processes and membrane dynamics.

An uncharted path of molecular investigation for TRPM7 regulation is the hypothesis that TRPM7 forms hetero-tetramers with other members of the TRP family channels, hence its regulation does not come across as linear, but instead is subject to modulation and different activation mechanism, depending on the cell and the surrounding environment. TRPM7 is a large (~210 kDa) membrane protein, composed of 1864 amino acids, which equals 5,592 bp of the coding sequence. This effectively impedes biochemical experimentation, on top of which macrophages are notoriously difficult to transfect or transduce. The lentiviral vectors offer transduction of non-dividing cells, but they have packaging constraints and can incorporate sequences only up to 10 kb in size. Packaging larger constructs leads to severely lowered viral titers and the formation of unstable viral particles[185]. Moreover, overexpression studies may not efficiently characterize the subcellular compartmentalization and are often discounted for their lack of specificity. Additionally, there are no reliable TRPM7 commercially available antibodies and antibodies recognizing the C'-terminal kinase can lead to obtaining misleading results in immunofluorescent studies, as TRPM7 kinase can be freed

and localize to different cellular compartments[43,66]. A large proportion of TRPM7 is contained in the intracellular vescicles[165] that are distinct from any membranous, well-characterized cellular compartment. This illustrates a dearth of molecular tools to study TRPM7 and the necessity of creating genetically edited mice with tagged-TRPM7, without affecting its function. To this end, we have successfully engineered a CRISPR-Cas9 knock-in mouse with an N'-terminal FLAG tag in the *Trpm7* sequence that appears in frame and is expressed at an mRNA and protein level (Appendix 2). However, we were unsuccessful in visualizing TRPM7 protein localization in macrophages through sensitive methods, like flow cytometry or confocal microscopy. Moreover, we observed reduced currents in the homozygous N'-FLAG-tagged primary macrophages, suggesting that the genetic tag may interfere with TRPM7 trafficking to the surface. We strive to create new CRISPR-Cas9 genetically edited mice, for example, extracellular-loop tag-insertion or kinase activity dead mutant mice that would help us track the localization and the TRPM7 kinase functions in the *in vivo* setting and would be of insurmountable scientific significance and information about TRPM7 expression, subcellular localization and kinase function.

APPENDIX 1: Toward an understanding of TRPM7 function in autophagy

Disclaimer: The contents of this chapter (text and figures) present unpublished data.

Abstract

Autophagy is a self-eating process, performed by all cells to prevent the accumulation of damaged organelles or protein aggregates and balance intracellular energy. Autophagy-induced proteins are recruited to elongate intracellular membranes that engulf the cytoplasmic ‘cargo’. The autophagosome is progressively acidified to degrade and recycle the engulfed contents. Here, we identify TRPM7 as a novel protein regulator of autophagic flux.

Background

To cope with transient stress, cells evolved a protective survival mechanism, known as autophagy, as an alternative to programmed cell death. Autophagy, or self-eating, is an evolutionarily conserved adaptation that involves activation of a lysosomal delivery pathway for recycling of damaged organelles, ubiquitinated and misfolded proteins, as well as the clearance of intracellular pathogens[186]. Three different types of autophagy mechanisms are recognized and include macro- and microautophagy and chaperone-mediated autophagy. The molecular mechanism of microautophagy has not been fully elucidated, however, it involves invagination of the lysosomal membrane to directly engulf the cytosolic material. Chaperone-mediated autophagy recruits chaperones, which recognize and bind to a KFERQ-related amino acid sequence exposed on misfolded proteins. The chaperone-complexes bind to Lamp2 protein on the lysosomal membrane and are translocated into the lumen for degradation. The generation of large, double-membrane intracellular vesicles, called autophagosomes is a defining feature of macroautophagy, herein referred to as autophagy. More than 40 autophagy-related effector proteins (Atg) have been identified so far, however, they are not exclusively involved in autophagy, but also can aid in phagocytosis[187]. Microtubule-associated protein 1 light chain 3 (MAPLC3; abbreviated LC3) is a 17 kDa soluble protein ubiquitously expressed in mammalian cells. Although LC3 has several

homologs, LC3B is most frequently assessed in autophagy assays. During autophagy induction, sequential activation of E1-like enzyme Atg7 and, E2-like enzyme Atg3 and the Atg12 complex catalyze the conjugation of phosphatidylethanolamine to LC3. Lipidated LC3 (LC3-II) is then inserted into the autophagosomal membrane and directs its maturation[188]. The increase in LC3-II correlates with the number of formed autophagosomes, hence it is widely used as a marker of autophagy activation. Autophagy is inhibited during intracellular Ca^{2+} chelation[189], the endoplasmic reticulum (ER) is an origin for autophagosome formation[190] and stimulation of TLR was shown to link autophagy and phagocytosis[191]. During starvation induced autophagy, lysosomal calcium (Ca^{2+}) signaling through TRPML1 channel activates calcineurin, which dephosphorylates transcription factor EB (TFEB). Dephosphorylated TFEB translocates to the nucleus and warrants transcription of genes, whose products are involved in lysosomal biogenesis[192].

Both phagocytosis and autophagy constitute lysosomal delivery pathways that use the cytoskeleton as means of intracellular trafficking. Branched actin polymerization is essential in the formation of the autophagosomes[193], moreover, autophagy machinery induction was observed during phagocytosis of yeast particles, albeit via different initiation mechanisms[194]. Considering the involvement of TRPM7 in the phagocytosis of yeast and its regulation of the cytoskeletal structure (Chapter One), we sought out to assess its roles in the process of

autophagy in macrophages. We found that TRPM7-deficient macrophages accumulate LC3-II proteins due to inhibition of the autophagic flux.

Results

Trpm7-deficient macrophages accumulate autophagic markers

Under fed conditions, mammalian target of rapamycin complex 1 (mTORC1) associates with and phosphorylates Unc-51-like kinase 1 (Ulk1) and Atg13, which are parts of the autophagy initiation complex, and prevents the initiation complex activation. During starvation, when the ATP levels decrease, adenosine monophosphate-activated protein kinase (AMPK) is activated and phosphorylates Ulk1 at a different site, which triggers initiation of autophagy[195]. Direct inhibition of TORC1 by Torin1, mimics starvation phenotype and potently induces autophagy. We sought to assess the role of TRPM7 in starvation or Torin1-induced autophagy in macrophages through assessing the LC3 autophagic markers. To evoke the maximal autophagic response we deprived the cells of nutrients by incubating them in $HBSS^{++}$, and Torin1 was added complete media. Macrophages were starved for 5h or overnight (O/N) and Torin1 treatment was applied at different concentrations (300 nM or 1 μM) also for 5h. Cells lysates were probed for LC3B via the western blot (Fig. 29 A). Both forms of LC3B (LC3B-I and LC3B-II) are recognized by the antibody and the lipidated LC3B (LC3B-II) denotes the lower,

~14 kDa band. From the western blot analysis, it was readily apparent that the TRPM7-deficient macrophages accumulated increased levels of LC3B-II, regardless of the autophagy inducer. A similar analysis in the RAW264.7 cell line, in which TRPM7 was knocked down using siRNA-mediated silencing, revealed a slightly higher accumulation of both, p62 and LC3-II. A classical autophagy receptor, p62, interacts with mono- and poly-ubiquitinated proteins to deliver them into the autophagosomal lumen. Autophagy activation reduces the expression of p62, since it is degraded together with the cargo it delivers and is widely used as a predictor of the autophagic flux[196]. Additionally, we used chloroquine (CQ), which is an inhibitor of the autophagic flux[197] and FTY720, a known inhibitor of the TRPM7 channel. As shown in the western blot, (Fig. 29 B) the increase of both, p62 and LC3B-II, is most evident in Trpm7-knock-down cells, regardless of the treatment.

Next, we tested whether this phenotype could also be observed in other cell types deficient in TRPM7. We used siRNA-mediated knockdown of TRPM7 expression in HeLa cells and tested the marker accumulation during CQ autophagic flux inhibition. No difference in LC3B-II levels was observed upon silencing of TRPM7, compared to WT or control siRNA treated cells (Fig. 29 C). In the meantime, we also generated a genetically edited TRPM7 KO HeLa cell line using the CRISPR-Cas9-mediated system. Stable transfection of a vector carrying Cas9, TRPM7-targeting sgRNA and puromycin resistance. To confirm the vector incorporation,

we blotted for Cas9 protein expression (Fig. 29 D) and tested the clone with the high levels of Cas9 expression as a proxy for an efficient TRPM7 deletion. However, no visible difference was observed between WT and TRPM7 KO HeLa cell line in their LC3B-II levels.

TRPM7 activity regulates the autophagic flux in macrophages

To further dissect the reason for the increased levels of LC3B-II in TRPM7-KO macrophages, we used transmission electron microscopy (TEM) and visualized the formed autophagosomes. Both WT and KO macrophages displayed an increased number of intracellular vesicles. Strikingly, the vacuoles in the TRPM7-deficient cells were visibly larger (Fig. 30 A), suggesting an autophagosome resolution defect. Autophagosomal flux depends on the efficient fusion of autophagosomes with the lysosomes. Confocal characterization and colocalization of the characteristic markers for each organelle give snapshots of the process at a given time. We starved cells for 6h in $HBSS^{++}$ and colocalized Lamp1, a lysosomal marker, and LC3B, an autophagosomal marker. We show a lower colocalization efficiency across all TRPM7-deficient KO BMDMs, as compared to their WT counterparts.

Dual-tagged-LC3 protein became a gold standard in assessing the autophagic flux dynamics. Green (GFP) and red fluorescent proteins (RFP) are fused to LC3 and

expressed in tandem. GFP and RFP expressed together, yield a yellow fluorescent signal as their ratio is ~1:1. GFP is unstable in acidic pH, therefore upon the delivery into lysosomes its fluorescence is quenched and so the increased ratio of RFP/GFP mirrors the increase in the autophagic flux (Fig. 30 C). To avoid the issues with inefficient transduction of macrophages, we purchased CAG-RFP-eGFP-LC3 reporter mice, which allow for tracking of the autophagic flux dynamics in primary cells. We isolated the BMDMs from the reported mice and knocked down the expression of TRPM7, as before. Torin1-induced autophagy increased the autophagic flux in the reporter BMDMs, however, only a marginal increase was observed in TRPM7-deficient cells (Fig. 30 D). Bafilomycin A1 (BafA1) inhibits the activity of v-ATPase and was used as a control of cell acidification. The data were normalized to BafA1 treated cells. These results clearly establish TRPM7 role in the regulation of autophagic flux.

Lysosomal activity is unperturbed in TRPM7 KO BMDMS

TFEB transcription factor is activated in autophagy and regulates transcription of multiple genes important for lysosomal biogenesis[192,198,199]. Efficient lysosomal degradation is dependent on the activity of resident acidophilic hydrolases and low pH=~5. To assess the activity of intracellular proteases we loaded macrophages with a DQ BSA substrate, which is a self-quenched BODIPY Dye of Bovine Serum

Albumin. Upon proteolytic activity the pH insensitive, highly quenched fluorescent dye, de-quenches and release bright fluorophores. We first assessed the Ca^{2+}-dependence of the proteolytic activity. We loaded RAW264.7 with Ca^{2+} chelators BAPTA-AM, EGTA-AM or pre-treated them with cytochalasin D (CytoD), a potent inhibitor of actin polymerization. We observed that efficient proteolysis was dependent on Ca^{2+} and actin dynamics (Fig.31 A), however, no difference in proteolytic activity was recorded for the TRPM7 KO BMDMs (Fig. 31 B). Cathepsin F (CTSF), dipeptyl peptidase 7 (DPP7), and galactosidase alpha (GLA) are some of the exemplary TFEB-targets important in lysosomal biogenesis. We measured their mRNA transcripts in WT and KO macrophages basally and after autophagy induction. No statistically significant difference was observed in TRPM7-deficient macrophages. Lastly, we measured the levels of intracellular acidification in the WT and KO macrophages basally and upon autophagy induction with Torin1. LysoSensor dyes are acidotropic probes that accumulate in the acidic organelles as a result of protonation. They are membrane-permeant and exhibit a pH-dependent increase in fluorescence upon acidification. Incubation of LysoSensor in WT and KO BMDMs revealed no difference basally (Fig. 31 D) and over time upon Torin1 (1 μM)-induction of autophagy (Fig. 31 E).

Future implications

Overall, the presented preliminary data assessed the autophagic flux in TRPM7-deficient macrophages and shows that its inhibition in BMDMs is independent of intracellular protease activity or pH. A more detailed characterization of the results obtained with different autophagy inducers and molecular investigation into the effector proteins is needed to understand the basis of the defect in the TRPM7-deficient macrophages.

APPENDIX ONE FIGURES

Figure 29

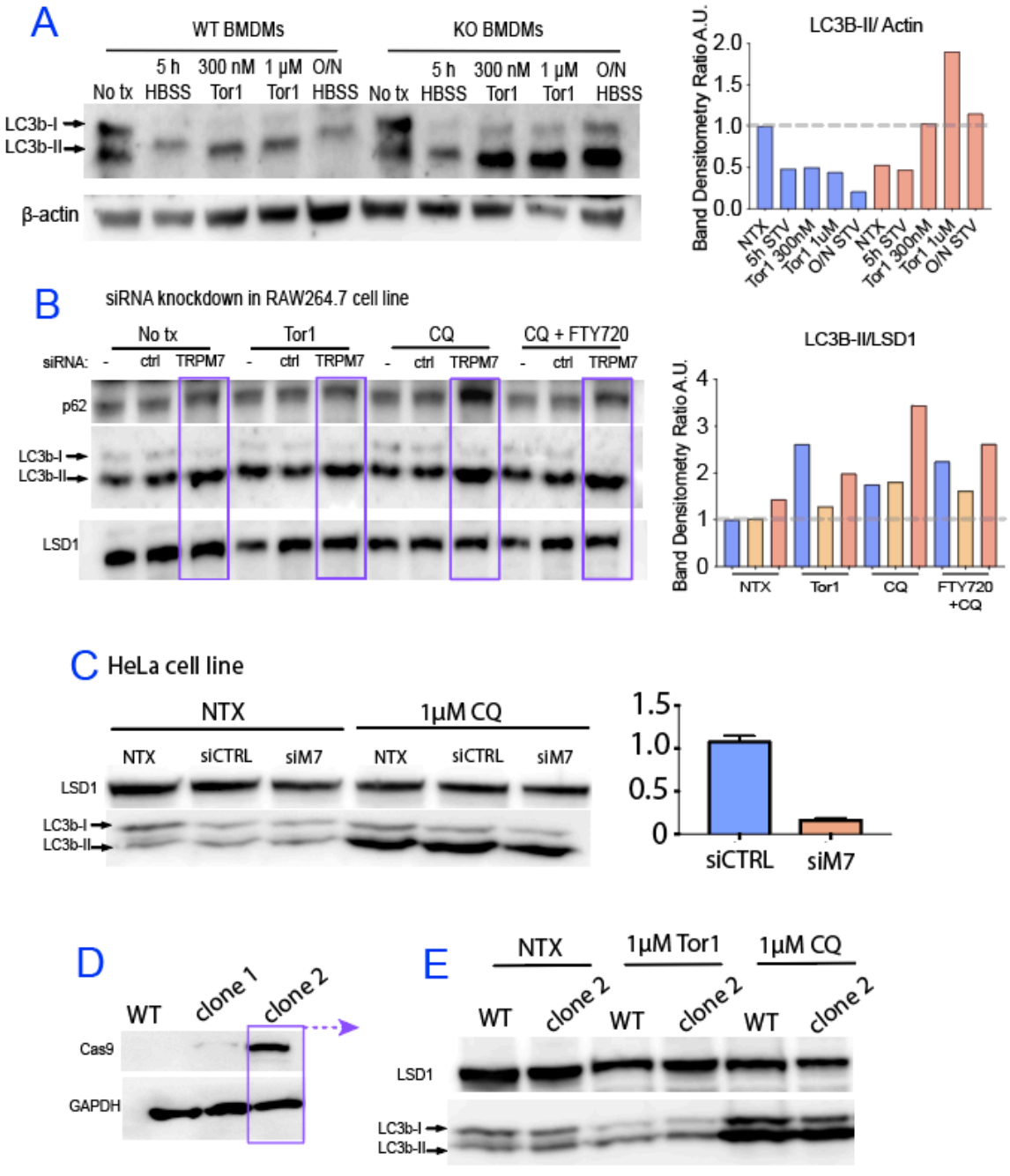

Figure 29. Increased autophagic markers accumulation in the TRPM7-deficient macrophages, but not HeLa cells

(A) Western blot analysis of LC3B autophagic marker in WT and KO BMDMs. The right panel represents a densitometric measurements ratio of the LC3B-II and β-actin loading control (WT-blue bars, KO-orange bars).

(B) Western blot analysis of the autophagic markers p62 and LC3B in the RAW264.7 cell line. The three lanes in each treatment condition are: no siRNA treatment (blue bars), siRNA control (yellow bars), siRNA targeting TRPM7 (red bars; additionally outlined with a purple rectangle on the western blot).

(C) Western blot analysis of LC3B in HeLa cells. The cells were subjected to siRNA-mediated knockdown of TRPM7 expression. Chloroquine (CQ) was applied for 5h.

(D) Western blot analysis for Cas9 protein expression in CRISPR-Cas9 mediated KO of TRPM7 in HeLa cell line. Two different clones were assessed and clone 2 was selected for further analysis.

(E) Western blot analysis of LC3B in TRPM7 KO HeLa cells (clone 2) upon induction of autophagy for 5h with Torin 1 (Tor1) or inhibition of autophagic flux with chloroquine (CQ).

Figure 30

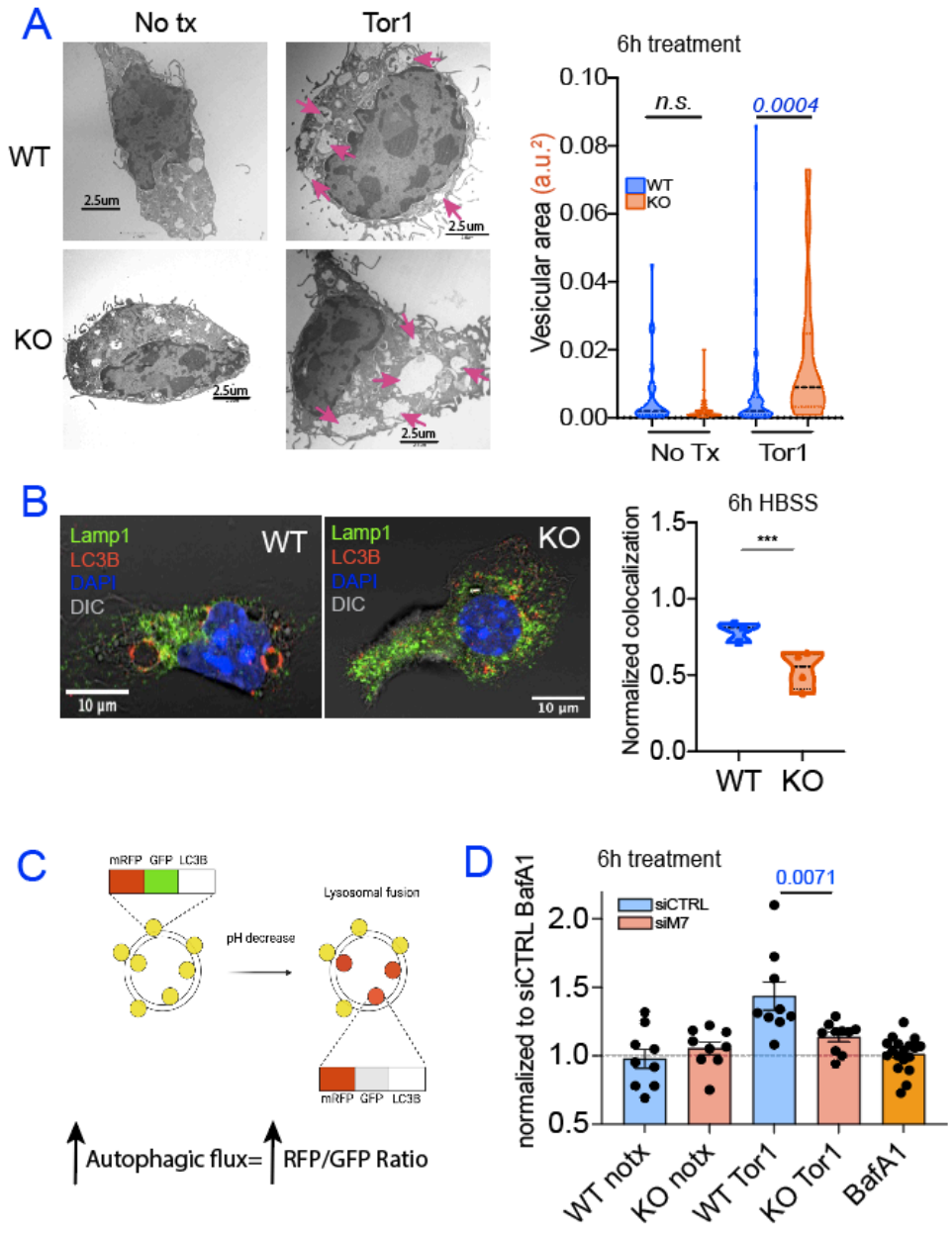
A
No tx
Tor1
WT
KO
2.5um
6h treatment
n.s.
0.0004
Vesicular area (a.u.²)
WT
KO
No Tx
Tor1
B
Lamp1
LC3B
DAPI
DIC
WT
KO
10 µm
6h HBSS
***
Normalized colocalization
WT
KO
C
mRFP GFP LC3B
pH decrease
Lysosomal fusion
Autophagic flux= RFP/GFP Ratio
D
6h treatment
0.0071
siCTRL
siM7
normalized to siCTRL BafA1
WT notx
KO notx
WT Tor1
KO Tor1
BafA1

Figure 30. Autophagic flux inhibition in TRPM7- deficient BMDMs.

(A) Representative images from TEM analysis of WT and TRPM7 KO macrophages at 6h treatment with Tor1 (1 μM). Right panel: the vesicular area was derived from tracing each vesicle in an image processing program (Fiji).

(B) Confocal microscopy images of WT and KO macrophages probed with LC3B and Lamp1 markers. The colocalization of autophagosomes ($LC3B^+$ organelles) and lysosomes ($Lamp1^+$ signal) serves as a proxy for autophagy flux. Autophagy was induced by 6h starvation in HBSS.

(C) The schematic of the autophagy flux measurement used in the reporter mice.

(D) The autophagic flux analysis in primary macrophages isolated from the reporter mice. To decrease TRPM7 expression, BMDMs were subjected to siRNA mediated knockdown. Autophagy was induced by a 6h Torin1 treatment (1 μM) and the results were obtained via flow cytometry. The RFP/GFP ratio of bafilomycin A1 (BafA1, 10 nM) treated macrophages was used to normalize all samples.

Figure 31

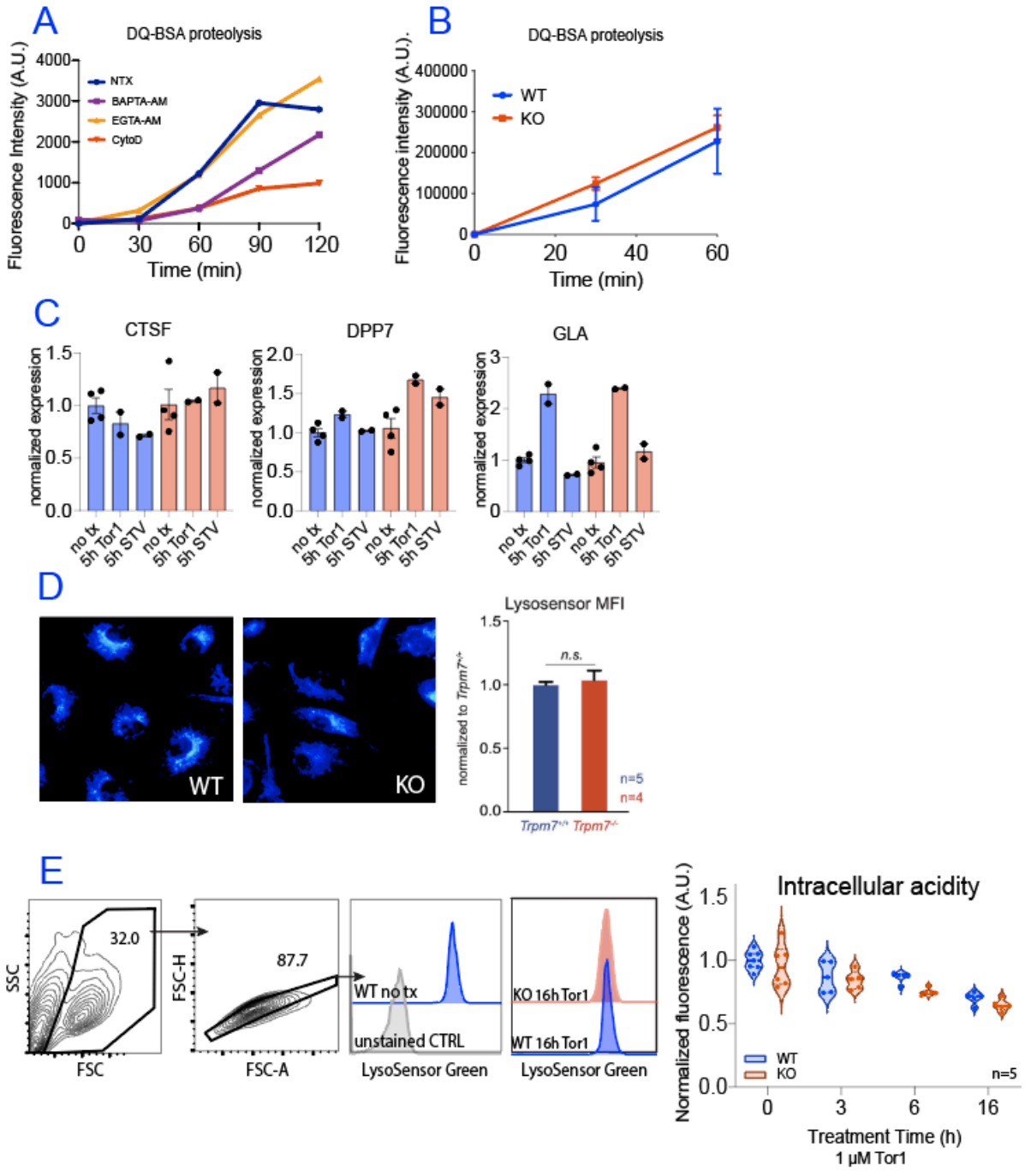
A
DQ-BSA proteolysis
Fluorescence Intensity (A.U.)
NTX
BAPTA-AM
EGTA-AM
CytoD
Time (min)
B
DQ-BSA proteolysis
Fluorescence intensity (A.U.).
WT
KO
Time (min)
C
CTSF
DPP7
GLA
normalized expression
no tx
5h Tor1
5h STV
D
WT
KO
Lysosensor MFI
n.s.
n=5
n=4
E
SSC
FSC
FSC-H
FSC-A
32.0
87.7
WT no tx
unstained CTRL
KO 16h Tor1
WT 16h Tor1
LysoSensor Green
Intracellular acidity
Normalized fluorescence (A.U.)
WT
KO
n=5
Treatment Time (h)
1 μM Tor1

Figure 31. Lysosomal activities are intact in TRPM7 KO BMDMs.

(A) DQ-BSA proteolysis assay in WT RAW264.7 cell line using Ca^{2+} chelators (EGTA-AM and BAPTA-AM, both at 10 μM) and cytochalasin D (CytoD, at 1 μM).

(B) DQ-BSA proteolysis assay in WT (blue) and KO (red) macrophages showing the increase of the intracellular proteolytic activity over time.

(C) qRT-PCR analysis of the TFEB gene-targets (*Ctsf*, *Dpp7*, *Gla*), which regulate the lysosome biogenesis and function. Autophagy was induced by 5h starvation in HBSS or Tor1 treatment (1 μM).

(D) Analysis of the LysoSensor fluorescence under a light microscope (images) or flow cytometry (right panel).

(E) Analysis of the LysoSensor fluorescence over time upon Tor1 treatment in WT (blue) and KO (red) BMDMs.

Methods

Western blots

Whole cell lysates were prepared by harvesting and incubating cells for 30 min on ice, in a desired volume of Lysis Buffer (300mM NaCl, 1% NP-4, 50mM Tris-HCl, 0.5% sodium deoxycholate, 0.1% SDS, pH= 7.4). Soluble proteins were harvested by centrifugation at 20,000 xg for 15 min in a table top centrifuge (4°C). Supernatants were mixed with 5X Laemmli Buffer (0.3M Tris-H-Cl, 10% SDS, 50% glycerol, 25% β-mercaptoethanol, 0.05% bromophenol- blue) and boiled at 95°C for 10 min. Samples were loaded onto 4–20% Mini-PROTEAN® TGX™ Precast Protein Gels (BioRad; #4561096) and separated by electrophoresis (150V, 90 min in SDS-PAGE buffer).

Generation of CRISPR-Cas9 HeLa cell line

Lenti-CRISPR-Cas9 plasmid with sgRNA targeting TRPM7 was purchased from Sigma (target site: CTATTGGAATAGCTCCATGGGG). HeLa cell line was transfected with 1-5 µg of the plasmid DNA and at day 3 put under puromycin pressure for at least a week. Cells were then single cell cloned and a couple of surviving colonies were grown out and subsequently tested for Cas9 protein expression.

Flow cytometry

The cells were stained with LysoSensor Green DND-189 (#L7535) according to the manufacturer's protocol. Incubation with 5 µg/ml DQ-BSA (#D12050) was performed as outlined in the figure. The stained cells were analyzed with an Attune Nxt (ThermoFisher). Every experiment included a positive and a negative control to facilitate the analysis with FlowJo version 10 software (Tree Star).

qRT-PCR

Macrophages were seeded onto a 12-well plate at a density of 0.5x 10^6 and cultured overnight. Next day they underwent stimulation as outlined in the figure panels. When using pharmacological treatment, the appropriate drug was added 10 min prior stimulation or as outlined in the manufacturer's protocol. RNA isolation was performed using RNeasy Plus Kit (Qiagen#74134) and cDNA synthesis was performed using GoScriptTM Reverse Transcriptase Kit (Promega #A5001). qRT-PCR reactions were performed using SensiFast SYBR no-rox kit (BIO-98020).

Author contributions

Conception: MES, BND; Research Design: MES; Experimental execution: MES, JJJ, Data analysis: MES, JJJ; Technical assistance: EJS, JK; Project Administration: BND

APPENDIX 2: Generation of CRISPR-Cas9 knock-in mice

Disclaimer:

The contents of this chapter (text and figure) present unpublished data.

The generation and validation of Panx1-S205A knock-in mice was previously described and published in: Medina CB, Chiu YH, **Stremska ME**, Lucas CD, Poon I, Tung KS, Elliott MR, Desai B, Lorenz UM, Bayliss DA, Ravichandran KS. *Pannexin 1 channels facilitate communication between T cells to restrict the severity of airway inflammation.* Immunity. 2021 Aug 10;54(8):1715-1727.e7. doi: 10.1016/j.immuni.2021.06.014. Epub 2021 Jul 21. PMID: 34283971; PMCID: PMC8363584.

Abstract

Genetically modified mice have been broadly used to further our understanding of the physiological functions of proteins *in vivo*. The implementation of the CRISPR-Cas9 system into the generation of genetically modified mice dramatically outperformed classical means of obtaining knockout (KO) and knock-in (KI) mice. Here, I describe our approach at generation 3 different genome-edited KI mice: N'-terminal FLAG-tag sequence insertion in TRPM7, an extracellular loop HA-tag insertion in Panx1, and a Panx1 point mutation, changing serine at position 205 into alanine. Tag-insertion mutant proteins are a useful tool in tracking the overall protein expression or subcellular protein trafficking. Point mutations are indispensable in assessing the roles of a particular amino acid in the signaling cascades.

Background

The CRISPR-Cas9 gene-editing method has been widely used to manipulate the genetic make-up of animal models to create gene-specific knockouts or knock-ins[200]. The CRISPR-Cas9 system outperforms standard procedures of creating a gene-edited animal and shortens the time required to develop such models. The CRISPR/Cas9 technology uses a sequence-specific short guide RNA (sgRNA), a Cas9 nuclease that is led to the site of DNA cleavage by the sgRNA, and a homologous recombination (HR) repair template (Fig. 32 A). To design the specific sgRNA, I used a web engine designed by the Zhang Lab at MIT (crispr.mit.edu), as well as another website: http://crispor.tefor.net. The chosen DNA sequence is scanned for possible sgRNA-target sites, which must meet the following criteria: (1) the 20 nucleotides (nts) sgRNA sequence has to be immediately followed by a PAM sequence (NGG; where "N" signifies any nucleotide) and (2) the 20 nts guide RNA sequence has to be unique throughout the indicated species genome. The guide scoring is computed as "*100% minus a weighted sum of off-target hit-scores in the target genome*" (from: http://crispr.mit.edu:8079/about). From the proposed guides (score of 50 or higher), I chose those which were positioned directly at, or closest to the region where I planned to insert the protein tag or point mutation. Cas9 endonuclease cuts both strands of the DNA 3nts upstream of the PAM site, therefore the induction of the DNA repair machinery is activated. Consequently, I

designed a 200 nts repair template, in which the mutation or tag is flanked by ~100 nts homology regions (in frame). This process facilitates repair through HR, as opposed to non-homologous end joining (NHEJ). The transcribed sgRNAs, the Cas9 protein, and the DNA template were submitted to Dr. Wenaho Xu at the Genetically Engineered Mouse Model (GEMM) Core, UVA, who microinjected them into the ES cells directly (B6.SJL strain), followed by transferring the injected embryos into pseudo-pregnant mice (Fig. 32 A).

Each single-stranded DNA (ssDNA) HR template was designed explicitly in a way to facilitate genotyping in the successful KI mutant mice. For tag-insertion (INS) mutants, one of the genotyping primers was complementary to the unique tag sequence (Fig. 29 B), producing an additional PCR band of a distinct size in the first round of the PCR reaction. This approach, however, did not differentiate between the hetero- and homozygous insertion. Therefore, a second genotyping strategy was designed, wherein a “split” primer was used. The “split” primer spanned the original genomic sequence, hence it would not bind to the DNA, in which the inserted-tag sequence was present, detecting tag-insertion in both alleles, by the absence of an additional PCR band. When designing a repair template for point-mutation knock-in mice, the mutated amino acid codon was selected deliberately to introduce a novel and unique restriction enzyme recognition site for facilitated genotyping. Specifically, for the Panx1-S205A mutant, the serine amino acid codon (TCT) was changed to alanine codon (GCG),

resulting in a restriction site recognized by Bsh1236I enzyme (Fig. 32 C). Additionally, all ssDNA repair templates contained a silent mutation of the PAM site to cease Cas9 endonuclease cutting, once the template was incorporated.

Results

Validation of N'-FLAG-TRPM7 mutant mice

Upon confirming the successful insertion via PCR genotyping and Sanger sequencing, the founder mouse was outbred with a wild-type C57BL/6J mouse. Subsequent heterozygous pups were bred together to achieve tag-insertion homozygosity and some were put aside for further outbreeding. Once the homozygous pups of both sexes were available, as confirmed by Sanger sequencing (Fig. 33 A) they became a breeding pair. It was apparent from the homozygous N'-FLAG-Trpm7 breeding pair that they produced smaller litters, usually of around 4 pups, and the heterozygous breeding pairs produced homozygous pups at a lower Mendelian ratio than expected (<25%). The pups, however, were of the same size as their WT counterparts and did not display signs of distress. We continued to closely monitor the ratio of the homozygous offspring because a global TRPM7 loss-of-function mutation is embryonic lethal. We performed a qRT-PCR to measure the mRNA expression of *Trpm7* and the FLAG-tag-*Trpm7* in WT/WT, WT/FLAG and FLAG/FLAG pups (Fig. 33 B). All mice

expressed *Trpm7* mRNA, however, we were subsequently unable to visualize the expression of the FLAG-tag at a protein level with anti-FLAG antibodies via confocal microscopy, western blot, flow cytometry or transmission electron microscopy with immuno-gold staining (Fig. 33 C). Electrophysiological analysis revealed decreased TRPM7 currents in heterozygous N'FLAG-TRPM7 mice (Fig. 33 D), suggesting that the TRPM7 protein is expressed at a lower level on the cell surface.

At this time, we are unsure whether the inefficient expression of TRPM7 is caused by protein misfolding or its lower trafficking to the cell membrane. Less-efficient trafficking, however, would retain the pool of TRPM7 intracellularly, and the fact that we were not able to visualize it intracellularly would suggest misfolding being the likely explanation. Genomic manipulation of the DNA sequence may have also altered regulatory sequences, like enhancer regions, that aid in transcription. However, we were able to detect mRNA *Trpm7* transcripts and the data implied they were even slightly elevated in the homozygous mutant mice. Further experimentation on the nature of lower TRPM7 function in the knock-in mutant mice will determine whether they could be used experimentally to assess TRPM7 activities in different cell types.

Validation of Panx1-EC-HA and Panx1-S205A gene-edited mice

Generation of the PANX1 CRISPR-Cas9 mutant KI mice was a part of a collaborative effort that aims to study the function of PANX1 in different disease models. Pannexins comprise a 3-member family of proteins (PANX1-3), which belong to the invertebrate innexin gap junction family[201]. PANX1 is a pore-forming hemichannel recently reported to form a heptameric structure[202]. The best-studied activation mechanism is through the C-terminal cleavage of PANX1 by caspase-3 and -7, during apoptosis[203], however, recent reports also suggest activation in a receptor-mediated manner via G_q-coupled receptors[204].

PANX1 global KOs are viable and develop normally, hence any perturbation to their genomic DNA sequence, would not alter the embryonic development of mice. Consequently, both genetically targeted PANX1 mutant mice displayed unperturbed development and normal litter sizes. PANX1 with an HA-tag in the extracellular loop (PANX1-EC-HA), was developed, as described earlier, with a slight modification. The ssDNA repair template was based on a previously validated PANX1-EC-HA expression construct, in which the least conserved residues in the EC-loop, were substituted for the HA-tag coding sequence. Amino acid residues FSWRQAAFV became the HA tag sequence: YPYDVPDYA. Genotyping strategy, described earlier (Fig. 32 B), revealed a positive insertion of the tag, which was further confirmed via Sanger sequencing to be in-frame (Fig. 34 A). The founder mouse was heterozygous for the HA-tag insertion and was

outbred to a wild-type C57BL/6J background mouse. The splenocytes and thymocytes from the hetero- and homozygous PANX1-EC-HA mice were isolated and assessed for the HA-tag expression. Flow cytometry results in the unpermeabilized cells revealed no detectable HA signal on the cell surface (Fig. 34 B). Pannexin 1 is post-translationally glycosylated and appears as 3 different-sized bands on the western blot[205]. Western blot analysis of the PANX1 expression in CRISPR-Cas9 genetically edited mouse thymocytes and splenocytes indicated alteration to the PANX1 glycosylation pattern, readily observed in the WT and heterozygous PANX1-EC-HA mice (Fig. 34 C). Unglycosylated PANX1 can traffic to the cell surface, however, there is a clear preference for glycosylated Panx1[205]. Nevertheless, whole-cell patch-clamp recordings of the PANX1 current in the UV-light-treated splenocytes from the homozygous EC-HA mice (Fig. 34 E), showed normal current activation. The peak current was also comparable to the PANX-1 current in the WT PANX1 overexpressing 293T cell line (Fig. 34 D). We are currently carrying out further characterization of the mutant protein to determine its functional consequence.

Serine at position 205 in the PANX1 amino acid sequence was found to be a phosphorylation site of the SIK kinase[206]. *In vitro* studies in 293T cells, co-expressing the PANX1-S205A and α1D adrenergic receptor constructs, confirmed cells unresponsiveness during the phenylephrine (PE) receptor-mediated activation of the PANX1 current. PANX1-S205A successful incorporation was also

observed in one heterozygous founder mouse, which was further bred to homozygosity. We resolved the 2 alleles of the founder mouse by TOPO-TA cloning of the PCR product (Fig. 35) and confirmed the desired amino acid substitution. The mice were transferred to our collaborators who performed the functional characterization[206].

Conclusions

Here, I described the successful generation of three novel mouse lines: N-FLAG-TRPM7, PANX1-EC-HA, and PANX1-S205A. We were not able to use the tag-insertion gene-edited mice as predicted, however, both mouse lines display an alteration to the protein function, which will be further explored. N-FLAG-TRPM7 primary cells display a hypomorph protein phenotype, as assessed by the TRPM7 current recordings, yet the homozygous pups are viable. Further functional studies will reveal the consequences of expressing altered TRPM7 channel activity. PANX1-EC-HA are currently undergoing characterization and the first results suggest the tag-substituted amino acids play an important role in the protein glycosylation and possibly trafficking to the cell membrane, without modifying the PANX1 current activation during UV-induced apoptotic cells death. PANX1-S205A gene-edited mice were already successfully incorporated into functional studies.

APPENDIX TWO FIGURES

Figure 32

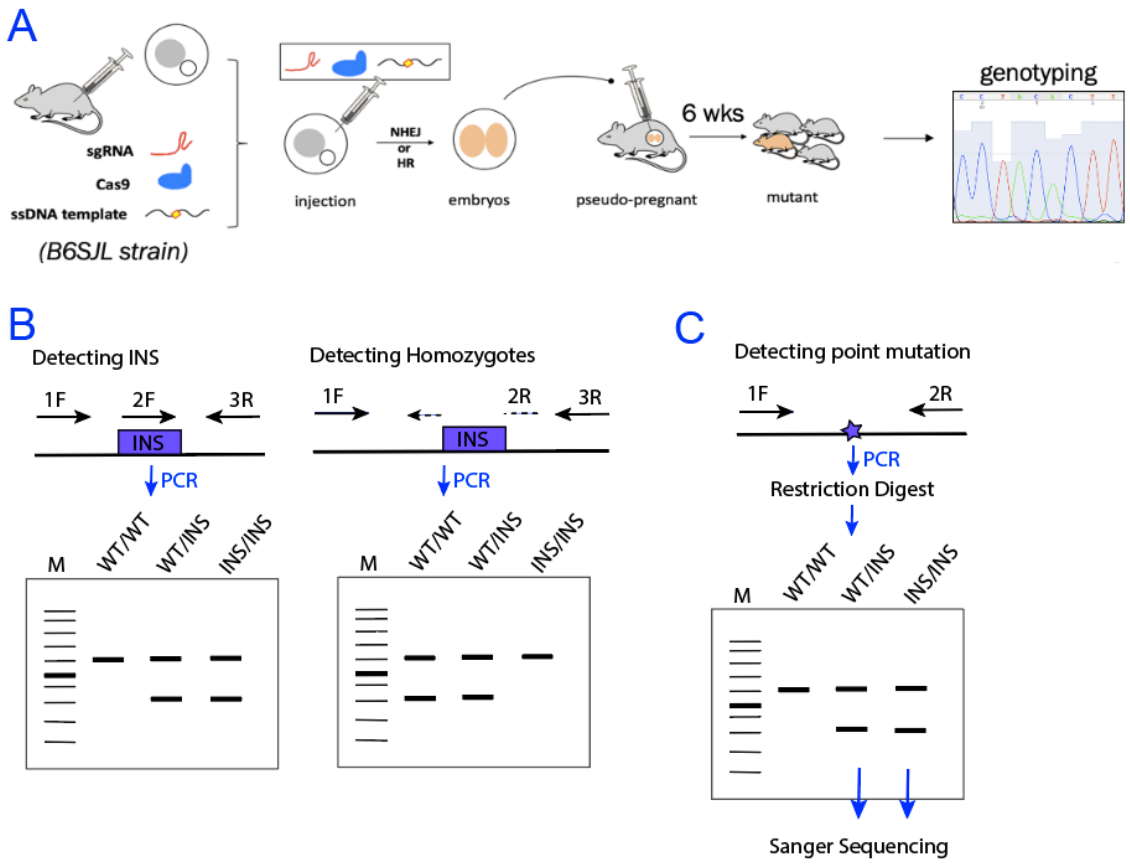

Figure 32. A general outline of the CRISPR-Cas9 gene-edited mice generation and genotyping strategy.

(A) Outline of knock-in mutant mice generation.

(B) General genotyping scheme for tag-insertion mutant mice. Left panel PCR outline detects the tag-sequence presence, whereas the right panel PCR outline helps distinguish between the homozygous and heterozygous insertions.

(C) Genotyping schematic for point mutation insertions. The ssDNA template is designed to harbor a novel restriction site for the ease of genotyping. This method however does not differentiate between the hetero- and homozygous mice, therefore mice positive for the lower band need to be additionally sequenced.

Figure 33

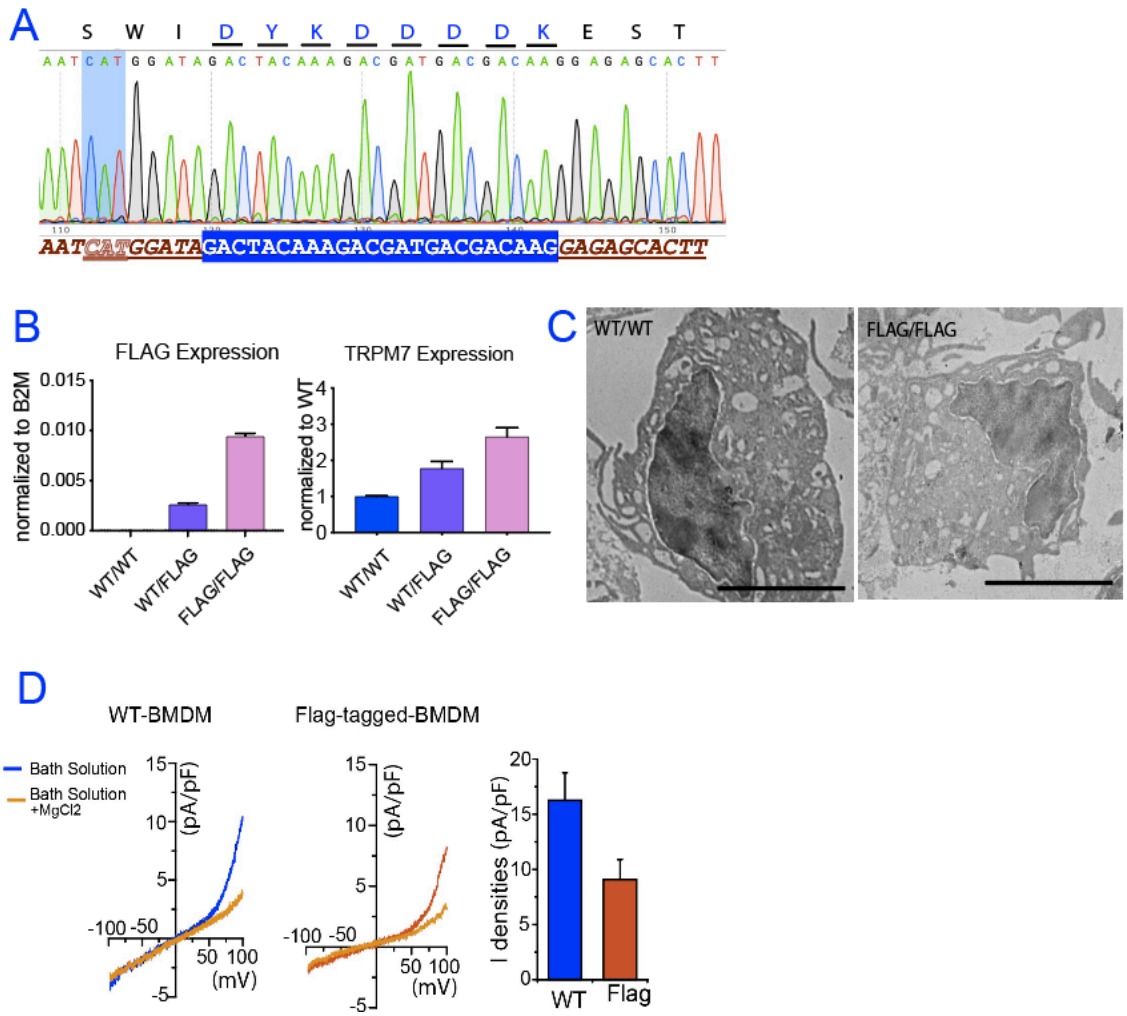
A
S W I D Y K D D D D K E S T
AATCATGGATAGACTACAAAGACGATGACGACAAGGAGAGCACTT
AATCATGGATAGACTACAAAGACGATGACGACAAGGAGAGCACTT
B
FLAG Expression
normalized to B2M
0.015
0.010
0.005
0.000
WT/WT
WT/FLAG
FLAG/FLAG
TRPM7 Expression
normalized to WT
4
3
2
1
0
WT/WT
WT/FLAG
FLAG/FLAG
C
WT/WT
FLAG/FLAG
D
WT-BMDM
Flag-tagged-BMDM
Bath Solution
Bath Solution +MgCl2
15
10
5
-5
(pA/pF)
-100 -50
50 100
(mV)
I densities (pA/pF)
20
15
10
5
0
WT
Flag

Figure 33. Validation of N'-FLAG-TRPM7 knock-in mice.

(A) Sanger sequencing histogram of a homozygous N'-FLAG-*Trpm7* mouse, outlining the FLAG insertion (blue shading) and the mutation of a PAM site (CCT to CAT; note the sgRNA sequence was designed in reverse, so the PAM sequence recognized by Cas9 was AGG). The underlined text symbolizes the sgRNA recognition sequence and the resulting insertion was in-frame, inserted in between amino acids: MSQSWI-FLAG-ESTLT, as outlined in the figure.

(B) qRT-PCR of mRNA expression of the FLAG insertion and *Trpm7* gene in WT, heterozygous and homozygous mutant mice.

(C) Transmission electron microscopy of the immuno-gold-stained WT and homozygous knock-in mice. No staining was observed in either genotype. Scale bar is 5 μm.

(D) Whole-Cell patch electrophysiology representative I-V graphs of the TRPM7 current in WT (blue) and heterozygous N'-FLAG-TRPM7 (red) BMDMs. $MgCl_2$ was added at the end of the recording to inhibit the current (orange traces). The quantification plot on the right represents the cumulative current densities at 10 mV.

Figure 34

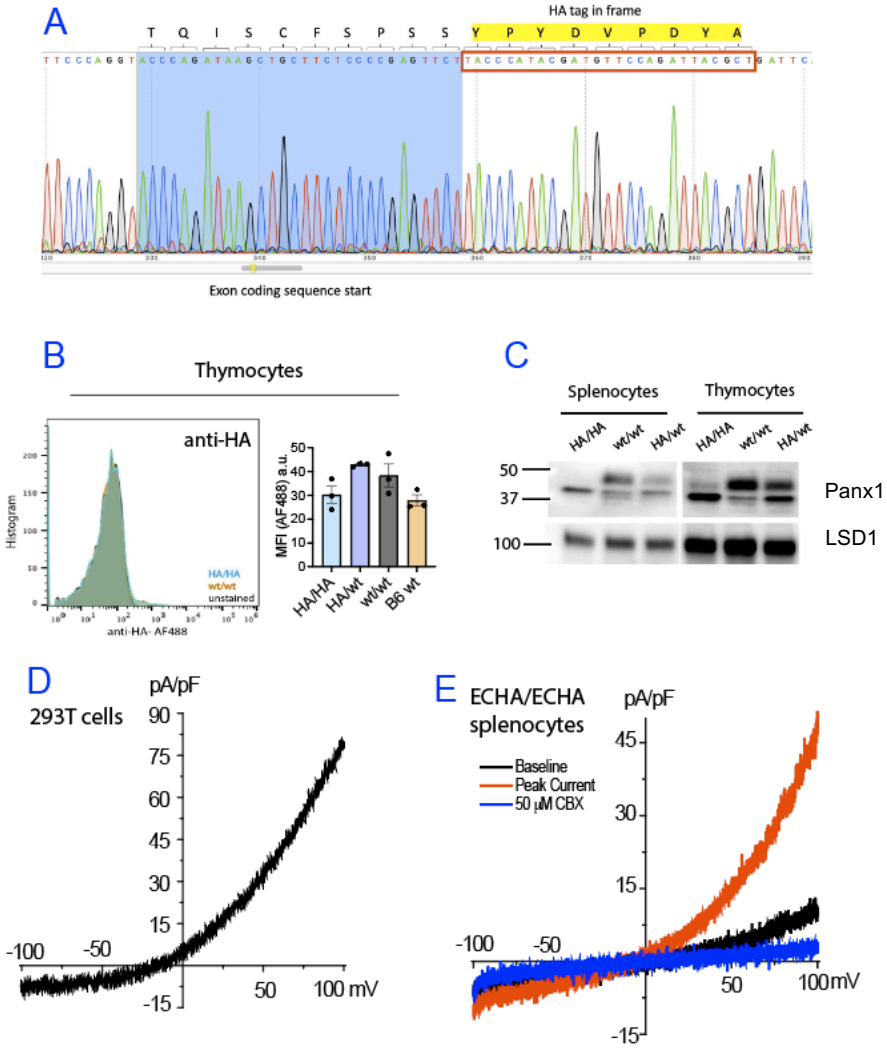
A
HA tag in frame
T Q I S C F S P S S Y P Y D V P D Y A
Exon coding sequence start
B
Thymocytes
anti-HA
Histogram
anti-HA- AF488
HA/HA
wt/wt
unstained
MFI (AF488) a.u.
HA/HA
HA/wt
wt/wt
B6 wt
C
Splenocytes
Thymocytes
HA/HA
wt/wt
HA/wt
50
37
100
Panx1
LSD1
D
293T cells
pA/pF
90
75
60
45
30
15
-15
-100
-50
50
100 mV
E
ECHA/ECHA
splenocytes
Baseline
Peak Current
50 μM CBX
pA/pF
45
30
15
-15
-100
-50
50
100mV

Figure 34. Validation of the PANX1-EC-HA knock-in mice.

(A) Sanger sequencing histogram of the genomic DNA sequence from a homozygous PANX1-EC-HA mutant mouse. Extracellular loop HA-tag (EC-HA) coding sequence is outlined in yellow. Exon coding sequence is shaded blue.

(B) Flow cytometry analysis of the HA-tag expression and quantification of the mean fluorescent intensity (MFI) signal for each sample. There was no detected positive signal for the HA-tagged protein.

(C) Western blot analysis of *Panx1* expression in splenocytes and thymocytes in the homozygous mutant (HA/HA), WT (WT/WT), and heterozygous (HA/WT) mice. Note that the homozygous mutant knock-in mice lack the characteristic glycosylation pattern (upper bands) of PANX1.

(D) Characteristic PANX1 I-V graph showing the PANX1 current (black trace). The measurement was performed in WT PANX1-overexpressing 293T cells, which were subjected to UV-induced apoptosis to activate PANX1.

(E) I-V graph representing the PANX1 current in EC-HA homozygous mutant splenocytes. Apoptosis was induced by UV-light to activate PANX1 current (orange trace) and carbenoxolone (CBX) was added at the end of the recording to inhibit PANX1 activity (blue trace).

Figure 35

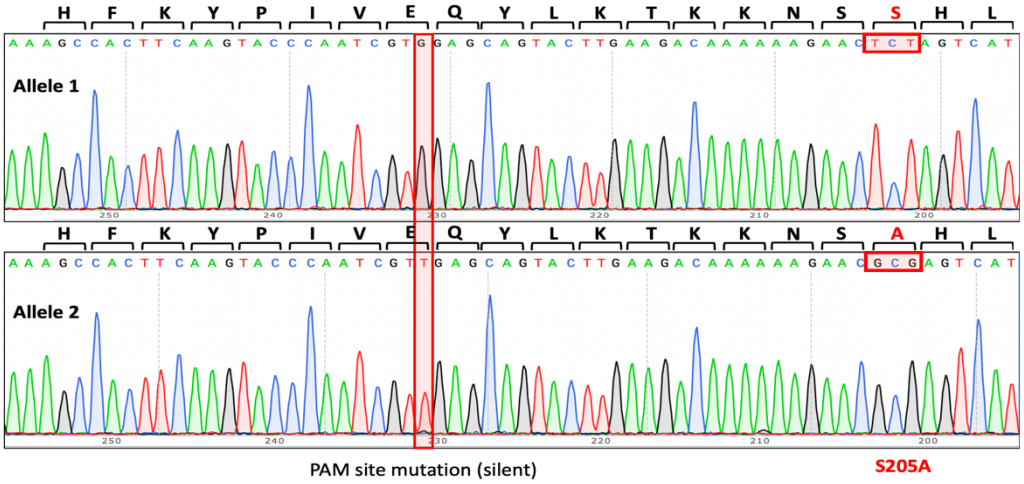
H F K Y P I V E Q Y L K T K K N S S H L
Allele 1
H F K Y P I V E Q Y L K T K K N S A H L
Allele 2
PAM site mutation (silent)
S205A

Figure 35. Sequencing results of the PAXN1-S205A knock-in mice.

Histogram of Panx1-S205A alleles, resolved through TOPO-TA cloning from a heterozygous knock-in mutant mouse. Allele 1 (upper panel) represents the WT DNA sequence, whereas Allele 2 (lower panel) shows the mutated DNA sequence. Outlined in the graph are PAM site silent mutation TGG to TTG and a serine (S; TCT) to alanine (A; GCG) mutation successfully incorporated into the mouse genome. The novel GCG insertion introduced a unique restriction site in the PCR product, recognized by Bsh1236I (CG^CG).

Methods

In-house-made sgRNA (for: N-FLAG-Trpm7, Panx1 S205A) and synthesized sgRNA (for Panx1-EC-HA; Synthego), Cas9 protein (PNA Bio # CP01) and single-stranded 200 bp oligo template (ssDNA; IDT) were submitted to the UVA GEMM (Genetically Engineered Mouse Model) Core, where the microinjection was performed into an embryo of B6.SJL mouse strain, followed by transplantation into a pseudo-pregnant mother.

sgRNA design

The highest scoring sgRNA, closest to the region of interest, was identified using http://crispor.tefor.net website. The oligos were synthesized through IDT, annealed, and cloned into pX330 expression plasmid (gift from Wenhao Xu), previously digested with BbsI (NEB#R3539). The ligation reaction was transformed into chemically competent cells. A couple of colonies were picked, mini-prepped (Invitrogen #K210010), and sequenced to ensure accurate cloning. High-fidelity PCR reaction was completed on confirmed clones, PCR was purified (Qiagen#28004) and in-vitro transcription reaction was performed, using MEGAscript™ T7 Transcription Kit (Cat# AMB13345). The products were purified with MEGAClear kit (#AM1908).

ssDNA template design

DNA repair template was precisely designed for tag-insertion or, in the case of S205A (TCT→GCG), the novel point mutation introduced a unique restriction site, recognized by Bsh1236I (#ER0921) for the ease of genotyping. The template also carried a silent mutation of the PAM site to cease Cas9 cutting.

Genetically-modified mouse breeding

The founder mouse for each insertion was heterozygous, as confirmed by genotyping and TOPO-TA cloning (#K4575J1), followed by Sanger sequencing. The founder mouse was bred to a wild-type C57BL/6J male (Jackson) and the offspring were bred to homozygosity.

Contributions

Conception of N-FLAG-TRPM7 CRISPR-Cas9 mouse creation: MES, BND, Conception of Panx1 CRISPR-Cas9 gene-edited mice: a collaborative effort between Bayliss Lab, Ravichandran Lab and Desai Lab. Design of sgRNAs and ssDNA templates: MES. Microinjection: Dr. Wenhao Xu. Genotyping and sequencing analyses: MES. Eva Chiu, PhD generated the Panx1-S205A vector. Electrophysiological recordings: SKM, GBW, WHI, all other experiments performed by MES.

APPENDIX TWO TABLES

Table 3. DNA sequences used for each CRISPR-Cas9 knock-in mouse generation

	DNA sequence
Panx1-S205A sgRNA	5'- CCACTTCAAGTACCCAATCG-3' (PAM site: TGG)
Panx1-S205A ssDNA	5'-GTGAAGAGAGGCTGAAGTAATAGCTCAAGTAGATACATGC CAACAGTATAACCACAAATGTCACCAGCCGGCAGCTAATGTA TTTCATGATTAAATGACT**CGC**GTTCTTTTTTGTCTTCAAGTACT GCTCAACGATTGGGTACTTGAAGTGGCTTTCAGATATCTCCC ACAGACTGAAAAACAAAGCAAATAAAAATAAT-3'
N-FLAG-Trpm7 sgRNA	5'-GGTCAAAGTGCTCTCTATCC-3' (PAM site: AGG)
N-FLAG-Trpm7 ssDNA	5'TCTTTTGTAAAATTACTTCCTCAGATTAGCAGGCTGTAAATT TGTAAACCATCTTTGAATTCTGTTTCAGTCCCAGAAATCATGG ATA**GACTACAAAGACGATGACGACAAG**GAGAGCACTTTGAC CAAGAGGGAGTGTGTATATATTATACCAAGCTCCAAAGACCC TCACAGGTAAACATACATTGATTTCTTCTAAA-3'
Panx1-EC-HA sgRNA	5'-TCGCCAGGAGAAAGAACTCG-3' (PAM site: GGG)
Panx1-EC-HA ssDNA	5'AGCGCTGACCACAGACAGCACTTAAGTTCCGTGGGGATAG TTCCGTCGAGCGAGGAAGGCAGGTCCGTGCTTCATTCATTT GGAACTATCTGCTTTGCTTCCCAG*GT*ACCCAGATAAGCTGCT TCTCCCCGAGTTCT**TACCCATACGATGTTCCAGATTACGCT**G ATTCATACTGCTGGGCTGCTGTACAGCAGAAGAGCTCCCTG CAGAGCGAGTCTGGAAACCTCCCACTGTGGCTGCACAAGGT AATGAGATGCTCTACAGATAGAGATGTGGAGGCCTGGGAAG GCGGTGCCAGCC-3'

Resulting publications:

1. *Mendu SK, ***Stremska ME**, Schappe MS, Moser EK, Krupa JK, Rogers JS, Stipes EJ, Parker CA, Braciale TJ, Perry JSA, Desai BN. Targeting the ion channel TRPM7 promotes the thymic development of regulatory T cells by promoting IL-2 signaling. Sci Signal. 2020 Dec 8;13(661):eabb0619. doi: 10.1126/scisignal.abb0619. PMID: 33293462; PMCID: PMC7884026. *equal contributing authors
2. **Stremska ME**, Stipes EJ, Jang JJ, Busey GW, Iobst WI, Seegren PV, Kennedy J, Desai BN, TRPM7- dependent electrical signals drive phagocytic clearance in effective anti-fungal defense. This work was recently submitted for publication.

Additional publications:

3. Etchegaray JI, Penberthy K, Gasperino S, Nagasaka Y, Paul S, Seshadri V, Raymond MH, Royo Marco A, Pinney J, **Stremska ME**, Barron BJ, Lucas CD, Wase N, Tabas I, Fan Y, Unanue ER, Kundu B, Burstyn-Cohen T, Gelfand BD, Perry JSA, Ravichandran KS, Unexpected local source of insulin in the eye that links to phagocytosis and starvation. This work was submitted to Nature.

4. Schappe MS, Szteyn K, **Stremska ME**, Mendu SK, Downs TK, Seegren PV, Mahoney MA, Dixit S, Krupa JK, Stipes EJ, Rogers JS, Adamson SE, Leitinger N, Desai BN. Chanzyme TRPM7 Mediates the Ca^{2+} Influx Essential for Lipopolysaccharide-Induced Toll-Like Receptor 4 Endocytosis and Macrophage Activation. Immunity. 2018 Jan 16;48(1):59-74.e5. doi: 10.1016/j.immuni.2017.11.026. PMID: 29343440; PMCID: PMC5783319.
5. Seegren PV, Downs TK, **Stremska ME**, Harper LR, Cao R, Olson RJ, Upchurch CM, Doyle CA, Kennedy J, Stipes EL, Leitinger N, Periasamy A, Desai BN. Mitochondrial Ca^{2+} Signaling Is an Electrometabolic Switch to Fuel Phagosome Killing. Cell Rep. 2020 Nov 24;33(8):108411. doi: 10.1016/j.celrep.2020.108411. PMID: 33238121; PMCID: PMC7793167.
6. Medina CB, Chiu YH, **Stremska ME**, Lucas CD, Poon I, Tung KS, Elliott MR, Desai B, Lorenz UM, Bayliss DA, Ravichandran KS. Pannexin 1 channels facilitate communication between T cells to restrict the severity of airway inflammation. Immunity. 2021 Aug 10;54(8):1715-1727.e7. doi: 10.1016/j.immuni.2021.06.014. Epub 2021 Jul 21. PMID: 34283971; PMCID: PMC8363584.
7. *Sabapathy V, ***Stremska ME**, Mohammad S, Corey RL, Sharma PR, Sharma R. Novel Immunomodulatory Cytokine Regulates Inflammation, Diabetes, and Obesity to Protect From Diabetic Nephropathy. Front Pharmacol. 2019 May

22;10:572. doi: 10.3389/fphar.2019.00572. PMID: 31191312; PMCID: PMC6540785. *equal contributing authors

8. ***Stremska ME**, *Dai C, Venkatadri R, Wang H, Sabapathy V, Kumar G, Jose S, Mohammad S, Sung SJ, Fu SM, Sharma R. IL233, an IL-2-IL-33 hybrid cytokine induces prolonged remission of mouse lupus nephritis by targeting Treg cells as a single therapeutic agent. J Autoimmun. 2019 Aug;102:133-141. doi: 10.1016/j.jaut.2019.05.005. Epub 2019 May 15. PMID: 31103267; PMCID: PMC6642024.*equal contributing authors
9. **Stremska ME**, Jose S, Sabapathy V, Huang L, Bajwa A, Kinsey GR, Sharma PR, Mohammad S, Rosin DL, Okusa MD, Sharma R. IL233, A Novel IL-2 and IL-33 Hybrid Cytokine, Ameliorates Renal Injury. J Am Soc Nephrol. 2017 Sep;28(9):2681-2693. doi: 10.1681/ASN.2016121272. Epub 2017 May 24. PMID: 28539382; PMCID: PMC5576940.
10. Norek A, **Stremska M**, Sobczyńska-Tomaszewska A, Wertheim-Tysarowska K, Dmeńska H, Jurek M. Novel de novo large deletion in cystic fibrosis transmembrane conductance regulator gene results in a severe cystic fibrosis phenotype. J Pediatr. 2011 Aug;159(2):343-6.e1. doi: 10.1016/j.jpeds.2011.04.022. Epub 2011 Jun 12. PMID: 21663921.

References

1. Barzaghi, F. & Passerini, L. IPEX Syndrome: Improved Knowledge of Immune Pathogenesis Empowers Diagnosis. *Frontiers Pediatrics* 9, 612760 (2021).

2. Pate, M., Damarla, V., Chi, D. S., Negi, S. & Krishnaswamy, G. Endothelial cell biology: role in the inflammatory response. *Adv Clin Chem* 52, 109–30 (2010).

3. Larsen, S. B., Cowley, C. J. & Fuchs, E. Epithelial cells: liaisons of immunity. *Curr Opin Immunol* 62, 45–53 (2020).

4. Pober, J. S. & Sessa, W. C. Evolving functions of endothelial cells in inflammation. *Nat Rev Immunol* 7, 803–815 (2007).

5. Gouaux, E. & MacKinnon, R. Principles of Selective Ion Transport in Channels and Pumps. *Science* 310, 1461–1465 (2005).

6. Feske, S., Skolnik, E. Y. & Prakriya, M. Ion channels and transporters in lymphocyte function and immunity. *Nat Rev Immunol* 12, 532–47 (2012).

7. Prakriya, M. & Lewis, R. S. Separation and Characterization of Currents through Store-operated CRAC Channels and Mg2+-inhibited Cation (MIC) Channels. *J Gen Physiology* 119, 487–508 (2002).

8. Feske, S., Wulff, H. & Skolnik, E. Y. Ion Channels in Innate and Adaptive Immunity. *Annu Rev Immunol* 33, 291–353 (2015).

9. Voolstra, O. & Huber, A. Post-Translational Modifications of TRP Channels. *Cells* 3, 258–287 (2014).

10. Laedermann, C. J., Abriel, H. & Decosterd, I. Post-translational modifications of voltage-gated sodium channels in chronic pain syndromes. *Front Pharmacol* 6, 263 (2015).

11. Petegem, F. V. Ryanodine Receptors: Structure and Function*. *J Biol Chem* 287, 31624–31632 (2012).

12. Fomina, A. F. Neglected wardens: T lymphocyte ryanodine receptors. *J Physiology* 599, 4415–4426 (2021).

13. Hosoi, E. *et al.* Expression of the Ryanodine Receptor Isoforms in Immune Cells. *J Immunol* 167, 4887–4894 (2001).

14. Vaeth, M. & Feske, S. Ion channelopathies of the immune system. *Curr Opin Immunol* 52, 39–50 (2018).

15. Vig, M. & Kinet, J.-P. Calcium signaling in immune cells. *Nat Immunol* 10, 21–27 (2009).

16. Nunes, P. & Demaurex, N. The role of calcium signaling in phagocytosis. *J Leukocyte Biol* 88, 57–68 (2010).

17. Desai, B. N. & Leitinger, N. Purinergic and Calcium Signaling in Macrophage Function and Plasticity. *Front Immunol* 5, 580 (2014).

18. Spix, B., Chao, Y.-K., Abrahamian, C., Chen, C.-C. & Grimm, C. TRPML Cation Channels in Inflammation and Immunity. *Front Immunol* 11, 225 (2020).

19. Rosato, A. S. *et al.* TRPML1 links lysosomal calcium to autophagosome biogenesis through the activation of the CaMKKβ/VPS34 pathway. *Nat Commun* 10, 5630 (2019).

20. Haase, H. & Rink, L. Functional Significance of Zinc-Related Signaling Pathways in Immune Cells. *Annu Rev Nutr* 29, 133–152 (2009).

21. Desai, B. N. & Clapham, D. E. TRP channels and mice deficient in TRP channels. *Pflügers Archiv* 451, 11–18 (2005).

22. Nilius, B. & Owsianik, G. The transient receptor potential family of ion channels. *Genome Biol* 12, 218–218 (2011).

23. Fischer, M. J. M. *et al.* Direct evidence for functional TRPV1/TRPA1 heteromers. *Pflügers Archiv - European J Physiology* 466, 2229–2241 (2014).

24. Cheng, W. *et al.* Heteromeric Heat-sensitive Transient Receptor Potential Channels Exhibit Distinct Temperature and Chemical Response*. *J Biol Chem* 287, 7279–7288 (2012).

25. Staruschenko, A., Jeske, N. A. & Akopian, A. N. Contribution of TRPV1-TRPA1 Interaction to the Single Channel Properties of the TRPA1 Channel*. *J Biol Chem* 285, 15167–15177 (2010).

26. Nilius, B., Owsianik, G., Voets, T. & Peters, J. A. Transient Receptor Potential Cation Channels in Disease. *Physiol Rev* 87, 165–217 (2007).

27. Iordanov, I., Mihályi, C., Tóth, B. & Csanády, L. The proposed channel-enzyme transient receptor potential melastatin 2 does not possess ADP ribose hydrolase activity. *Elife* 5, e17600 (2016).

28. Schmitz, C. *et al.* The Channel Kinases TRPM6 and TRPM7 Are Functionally Nonredundant*. *J Biol Chem* 280, 37763–37771 (2005).

29. Schlingmann, K. P. *et al.* Hypomagnesemia with secondary hypocalcemia is caused by mutations in TRPM6, a new member of the TRPM gene family. *Nat Genet* 31, 166–170 (2002).

30. Walder, R. Y. *et al.* Mutation of TRPM6 causes familial hypomagnesemia with secondary hypocalcemia. *Nat Genet* 31, 171–174 (2002).

31. Duncan, L. M. *et al.* Down-regulation of the novel gene melastatin correlates with potential for melanoma metastasis. *Cancer Res* 58, 1515–20 (1998).

32. Kunert-Keil, C., Bisping, F., Krüger, J. & Brinkmeier, H. Tissue-specific expression of TRP channel genes in the mouse and its variation in three different mouse strains. *Bmc Genomics* 7, 159–159 (2006).

33. Jin, J. *et al.* Deletion of Trpm7 Disrupts Embryonic Development and Thymopoiesis Without Altering Mg2+ Homeostasis. *Science* 322, 756–760 (2008).

34. Runnels, L. W., Yue, L. & Clapham, D. E. TRP-PLIK, a Bifunctional Protein with Kinase and Ion Channel Activities. *Science* 291, 1043–1047 (2001).

35. Nadler, M. J. S. *et al.* LTRPC7 is a Mg·ATP-regulated divalent cation channel required for cell viability. *Nature* 411, 590–595 (2001).

36. Ryazanova, L. V., Pavur, K. S., Petrov, A. N., Dorovkov, M. V. & Ryazanov, A. G. Novel Type of Signaling Molecules: Protein Kinases Covalently Linked with Ion Channels. *Mol Biol+* 35, 271–283 (2001).

37. Schmitz, C. *et al.* Regulation of Vertebrate Cellular Mg2+ Homeostasis by TRPM7. *Cell* 114, 191–200 (2003).

38. Matsushita, M. *et al.* Channel Function Is Dissociated from the Intrinsic Kinase Activity and Autophosphorylation of TRPM7/ChaK1*. *J Biol Chem* 280, 20793–20803 (2005).

39. Desai, B. N. *et al.* Cleavage of TRPM7 Releases the Kinase Domain from the Ion Channel and Regulates Its Participation in Fas-Induced Apoptosis. *Dev Cell* 22, 1149–1162 (2012).

40. Ryazanova, L. V., Dorovkov, M. V., Ansari, A. & Ryazanov, A. G. Characterization of the Protein Kinase Activity of TRPM7/ChaK1, a Protein Kinase Fused to the Transient Receptor Potential Ion Channel*. *J Biol Chem* 279, 3708–3716 (2004).

41. Dorovkov, M. V. & Ryazanov, A. G. Phosphorylation of Annexin I by TRPM7 Channel-Kinase*. *J Biol Chem* 279, 50643–50646 (2004).

42. Clark, K. *et al.* TRPM7 Regulates Myosin IIA Filament Stability and Protein Localization by Heavy Chain Phosphorylation. *J Mol Biol* 378, 790–803 (2008).

43. Krapivinsky, G., Krapivinsky, L., Manasian, Y. & Clapham, D. E. The TRPM7 Chanzyme Is Cleaved to Release a Chromatin-Modifying Kinase. *Cell* 157, 1061–1072 (2014).

44. Cai, N., Bai, Z., Nanda, V. & Runnels, L. W. Mass Spectrometric Analysis of TRPM6 and TRPM7 Phosphorylation Reveals Regulatory Mechanisms of the Channel-Kinases. *Sci Rep-uk* 7, 42739 (2017).

45. Jiang, J., Li, M. & Yue, L. Potentiation of TRPM7 Inward Currents by Protons. *J Gen Physiology* 126, 137–150 (2005).

46. Langeslag, M., Clark, K., Moolenaar, W. H., Leeuwen, F. N. van & Jalink, K. Activation of TRPM7 Channels by Phospholipase C-coupled Receptor Agonists*. *J Biol Chem* 282, 232–239 (2007).

47. Schappe, M. S. *et al.* Chanzyme TRPM7 Mediates the Ca2+ Influx Essential for Lipopolysaccharide-Induced Toll-Like Receptor 4 Endocytosis and Macrophage Activation. *Immunity* 48, 59-74.e5 (2018).

48. Nadolni, W. *et al.* TRPM7 Kinase Is Essential for Neutrophil Recruitment and Function via Regulation of Akt/mTOR Signaling. *Front Immunol* 11, 606893 (2021).

49. Zierler, S. *et al.* TRPM7 kinase activity regulates murine mast cell degranulation. *J Physiology* 594, 2957–2970 (2016).

50. Aifantis, I., Gounari, F., Scorrano, L., Borowski, C. & Boehmer, H. von. Constitutive pre-TCR signaling promotes differentiation through Ca2+ mobilization and activation of NF-kappaB and NFAT. *Nat Immunol* 2, 403–9 (2001).

51. Brown, G. D. *et al.* Hidden Killers: Human Fungal Infections. *Sci Transl Med* 4, 165rv13-165rv13 (2012).

52. Hampe, I. A. I., Friedman, J., Edgerton, M. & Morschhäuser, J. An acquired mechanism of antifungal drug resistance simultaneously enables Candida albicans to escape from intrinsic host defenses. *Plos Pathog* 13, e1006655 (2017).

53. Roy, A., Kumar, A., Baruah, D. & Tamuli, R. Calcium signaling is involved in diverse cellular processes in fungi. *Mycol* 12, 1–15 (2020).

54. Underhill, D. M. & Pearlman, E. Immune Interactions with Pathogenic and Commensal Fungi: A Two-Way Street. *Immunity* 43, 845–858 (2015).

55. Brown, G. D. *et al.* Dectin-1 Mediates the Biological Effects of β-Glucans. *J Exp Medicine* 197, 1119–1124 (2003).

56. Gantner, B. N., Simmons, R. M. & Underhill, D. M. Dectin-1 mediates macrophage recognition of Candida albicans yeast but not filaments. *Embo J* 24, 1277–1286 (2005).

57. Jaumouillé, V. *et al.* Actin Cytoskeleton Reorganization by Syk Regulates Fcγ Receptor Responsiveness by Increasing Its Lateral Mobility and Clustering. *Dev Cell* 29, 534–546 (2014).

58. Park, H. & Cox, D. Syk Regulates Multiple Signaling Pathways Leading to CX3CL1 Chemotaxis in Macrophages*. *J Biol Chem* 286, 14762–14769 (2011).

59. Westman, J., Grinstein, S. & Maxson, M. E. Revisiting the role of calcium in phagosome formation and maturation. *J Leukocyte Biol* 106, 837–851 (2019).

60. Clark, K. *et al.* TRPM7, a novel regulator of actomyosin contractility and cell adhesion. *Embo J* 25, 290–301 (2006).

61. Beesetty, P. *et al.* Inactivation of TRPM7 kinase in mice results in enlarged spleens, reduced T-cell proliferation and diminished store-operated calcium entry. *Sci Rep-uk* 8, 3023 (2018).

62. Mendu, S. K. *et al.* Targeting the ion channel TRPM7 promotes the thymic development of regulatory T cells by promoting IL-2 signaling. *Sci Signal* 13, eabb0619 (2020).

63. Romagnani, A. *et al.* TRPM7 kinase activity is essential for T cell colonization and alloreactivity in the gut. *Nat Commun* 8, 1917 (2017).

64. Schappe, M. S. *et al.* Chanzyme TRPM7 Mediates the Ca2+ Influx Essential for Lipopolysaccharide-Induced Toll-Like Receptor 4 Endocytosis and Macrophage Activation. *Immunity* 48, 59-74.e5 (2018).

65. Wykes, R. C. E. *et al.* Functional Transient Receptor Potential Melastatin 7 Channels Are Critical for Human Mast Cell Survival. *J Immunol* 179, 4045–4052 (2007).

66. Desai, B. N. *et al.* Cleavage of TRPM7 Releases the Kinase Domain from the Ion Channel and Regulates Its Participation in Fas-Induced Apoptosis. *Dev Cell* 22, 1149–1162 (2012).

67. Conti, H. R., Huppler, A. R., Whibley, N. & Gaffen, S. L. Animal Models for Candidiasis. *Curr Protoc Immunol* 105, 19.6.1-19.6.17 (2014).

68. Seegren, P. V. *et al.* Mitochondrial Ca2+ Signaling Is an Electrometabolic Switch to Fuel Phagosome Killing. *Cell Reports* 33, 108411 (2020).

69. Gao, H. *et al.* EGF enhances the migration of cancer cells by up-regulation of TRPM7. *Cell Calcium* 50, 559–568 (2011).

70. Visser, D. *et al.* TRPM7 triggers Ca2+ sparks and invadosome formation in neuroblastoma cells. *Cell Calcium* 54, 404–415 (2013).

71. Green, T. D. *et al.* Directed migration of mouse macrophages in vitro involves myristoylated alanine-rich C-kinase substrate (MARCKS) protein. *J Leukocyte Biol* 92, 633–639 (2012).

72. Wang, M. *et al.* Mannan-Binding Lectin Inhibits Candida albicans-Induced Cellular Responses in PMA-Activated THP-1 Cells through Toll-Like Receptor 2 and Toll-Like Receptor 4. *Plos One* 8, e83517 (2013).

73. Wang, W. *et al.* A small secreted protein triggers a TLR2/4-dependent inflammatory response during invasive Candida albicans infection. *Nat Commun* 10, 1015 (2019).

74. Guo, Y. *et al.* C-Type Lectin Receptor CD23 Is Required for Host Defense against Candida albicans and Aspergillus fumigatus Infection. *J Immunol* 201, 2427–2440 (2018).

75. Zhu, L.-L. *et al.* C-Type Lectin Receptors Dectin-3 and Dectin-2 Form a Heterodimeric Pattern-Recognition Receptor for Host Defense against Fungal Infection. *Immunity* 39, 324–334 (2013).

76. Ganesan, S. *et al.* Caspase-8 Modulates Dectin-1 and Complement Receptor 3–Driven IL-1β Production in Response to β-Glucans and the Fungal Pathogen, Candida albicans. *J Immunol* 193, 2519–2530 (2014).

77. Jaeger, M. *et al.* The RIG-I-like helicase receptor MDA5 (IFIH1) is involved in the host defense against Candida infections. *Eur J Clin Microbiol* 34, 963–974 (2015).

78. Qin, X. *et al.* Sphingosine and FTY720 are potent inhibitors of the transient receptor potential melastatin 7 (TRPM7) channels. *Brit J Pharmacol* 168, 1294–1312 (2013).

79. McCracken, A. N. *et al.* Phosphorylation of a constrained azacyclic FTY720 analog enhances anti-leukemic activity without inducing S1P receptor activation. *Leukemia* 31, 669–677 (2017).

80. Stone, M. L. *et al.* Sphingosine-1-phosphate receptor 1 agonism attenuates lung ischemia-reperfusion injury. *Am J Physiol-lung C* 308, L1245–L1252 (2015).

81. Goodridge, H. S., Simmons, R. M. & Underhill, D. M. Dectin-1 Stimulation by Candida albicans Yeast or Zymosan Triggers NFAT Activation in Macrophages and Dendritic Cells. *J Immunol* 178, 3107–3115 (2007).

82. Goodridge, H. S. *et al.* Activation of the innate immune receptor Dectin-1 upon formation of a ‘phagocytic synapse.’ *Nature* 472, 471–475 (2011).

83. Girotti, M., Evans, J. H., Burke, D. & Leslie, C. C. Cytosolic Phospholipase A2 Translocates to Forming Phagosomes during Phagocytosis of Zymosan in Macrophages* [boxs]. *J Biol Chem* 279, 19113–19121 (2004).

84. Kelly, E. K., Wang, L. & Ivashkiv, L. B. Calcium-Activated Pathways and Oxidative Burst Mediate Zymosan-Induced Signaling and IL-10 Production in Human Macrophages. *J Immunol* 184, 5545–5552 (2010).

85. Faouzi, M., Kilch, T., Horgen, F. D., Fleig, A. & Penner, R. The TRPM7 channel kinase regulates store-operated calcium entry. *J Physiology* 595, 3165–3180 (2017).

86. Bomfim, G. H. S., Costiniti, V., Li, Y., Idaghdour, Y. & Lacruz, R. S. TRPM7 activation potentiates SOCE in enamel cells but requires ORAI. *Cell Calcium* 87, 102187 (2020).

87. Courjaret, R., Dib, M. & Machaca, K. Spatially restricted subcellular Ca2+ signaling downstream of store-operated calcium entry encoded by a cortical tunneling mechanism. *Sci Rep-uk* 8, 11214 (2018).

88. Venkatachalam, G., Arumugam, S. & Doble, M. Synthesis, Characterization, and Biological Activity of Aminated Zymosan. *Acs Omega* 5, 15973–15982 (2020).

89. Vega-Garcia, D., Brito-Parada, P. R. & Cilliers, J. J. Optimising small hydrocyclone design using 3D printing and CFD simulations. *Chem Eng J* 350, 653–659 (2018).

90. Tam, J. M., Mansour, M. K., Khan, N. S., Yoder, N. C. & Vyas, J. M. Use of fungal derived polysaccharide -conjugated particles to probe Dectin-1 responses in innate immunity. *Integr Biol* 4, 220–227 (2011).

91. Vorselen, D. *et al.* Phagocytic “teeth” and myosin-II “jaw” power target constriction during phagocytosis. *Elife* 10, e68627 (2021).

92. Barger, S. R. *et al.* Membrane-cytoskeletal crosstalk mediated by myosin-I regulates adhesion turnover during phagocytosis. *Nat Commun* 10, 1249 (2019).

93. Ostrowski, P. P., Freeman, S. A., Fairn, G. & Grinstein, S. Dynamic Podosome-Like Structures in Nascent Phagosomes Are Coordinated by Phosphoinositides. *Dev Cell* 50, 397-410.e3 (2019).

94. Chubanov, V., Schäfer, S., Ferioli, S. & Gudermann, T. Natural and Synthetic Modulators of the TRPM7 Channel. *Cells* 3, 1089–1101 (2014).

95. Hofmann, T. *et al.* Activation of TRPM7 channels by small molecules under physiological conditions. *Pflügers Archiv - European J Physiology* 466, 2177–2189 (2014).

96. Stritt, S. *et al.* Defects in TRPM7 channel function deregulate thrombopoiesis through altered cellular Mg2+ homeostasis and cytoskeletal architecture. *Nat Commun* 7, 11097 (2016).

97. Arora, P. D., Glogauer, M., Kapus, A., Kwiatkowski, D. J. & McCulloch, C. A. Gelsolin Mediates Collagen Phagocytosis through a Rac-dependent Step. *Mol Biol Cell* 15, 588–599 (2004).

98. Rotty, J. D. *et al.* Arp2/3 Complex Is Required for Macrophage Integrin Functions but Is Dispensable for FcR Phagocytosis and In Vivo Motility. *Dev Cell* 42, 498-513.e6 (2017).

99. Siddiqui, T. A., Lively, S., Vincent, C. & Schlichter, L. C. Regulation of podosome formation, microglial migration and invasion by Ca2+-signaling molecules expressed in podosomes. *J Neuroinflamm* 9, 250 (2012).

100. Helden, S. F. G. van *et al.* A Critical Role for Prostaglandin E2 in Podosome Dissolution and Induction of High-Speed Migration during Dendritic Cell Maturation. *J Immunol* 177, 1567–1574 (2006).

101. Cai, N., Lou, L., Al-Saadi, N., Tetteh, S. & Runnels, L. W. The kinase activity of the channel-kinase protein TRPM7 regulates stability and localization of the TRPM7 channel in polarized epithelial cells. *J Biol Chem* 293, 11491–11504 (2018).

102. Crawley, S. W. & Côté, G. P. Identification of dimer interactions required for the catalytic activity of the TRPM7 alpha-kinase domain. *Biochem J* 420, 115–122 (2009).

103. Schmitz, C. *et al.* Regulation of Vertebrate Cellular Mg2+ Homeostasis by TRPM7. *Cell* 114, 191–200 (2003).

104. Ince, C. *et al.* Phagocytosis by human macrophages is accompanied by changes in ionic channel currents. *J Cell Biology* 106, 1873–1878 (1988).

105. Hackam, D. J. *et al.* v-SNARE-dependent secretion is required for phagocytosis. *Proc National Acad Sci* 95, 11691–11696 (1998).

106. Schindelin, J. *et al.* Fiji: an open-source platform for biological-image analysis. *Nat Methods* 9, 676–682 (2012).

107. Wong, H. S. & Germain, R. N. Robust control of the adaptive immune system. *Semin Immunol* 36, 17–27 (2017).

108. Wing, J. B., Tanaka, A. & Sakaguchi, S. Human FOXP3+ Regulatory T Cell Heterogeneity and Function in Autoimmunity and Cancer. *Immunity* 50, 302–316 (2019).

109. Hori, S., Nomura, T. & Sakaguchi, S. Control of Regulatory T Cell Development by the Transcription Factor Foxp3. *Science* 299, 1057–1061 (2003).

110. Fontenot, J. D., Gavin, M. A. & Rudensky, A. Y. Foxp3 programs the development and function of CD4+CD25+ regulatory T cells. *Nat Immunol* 4, 330–336 (2003).

111. Bennett, C. L. *et al.* The immune dysregulation, polyendocrinopathy, enteropathy, X-linked syndrome (IPEX) is caused by mutations of FOXP3. *Nat Genet* 27, 20–21 (2001).

112. Brunkow, M. E. *et al.* Disruption of a new forkhead/winged-helix protein, scurfin, results in the fatal lymphoproliferative disorder of the scurfy mouse. *Nat Genet* 27, 68–73 (2001).

113. Khattri, R., Cox, T., Yasayko, S.-A. & Ramsdell, F. An essential role for Scurfin in CD4+CD25+ T regulatory cells. *Nat Immunol* 4, 337–342 (2003).

114. Wildin, R. S. *et al.* X-linked neonatal diabetes mellitus, enteropathy and endocrinopathy syndrome is the human equivalent of mouse scurfy. *Nat Genet* 27, 18–20 (2001).

115. Malek, T. R. The main function of IL-2 is to promote the development of T regulatory cells. *J Leukocyte Biol* 74, 961–965 (2003).

116. Bayer, A. L., Pugliese, A. & Malek, T. R. The IL-2/IL-2R system: from basic science to therapeutic applications to enhance immune regulation. *Immunol Res* 57, 197–209 (2013).

117. Fontenot, J. D., Rasmussen, J. P., Gavin, M. A. & Rudensky, A. Y. A function for interleukin 2 in Foxp3-expressing regulatory T cells. *Nat Immunol* 6, 1142–1151 (2005).

118. Burchill, M. A. *et al.* Linked T Cell Receptor and Cytokine Signaling Govern the Development of the Regulatory T Cell Repertoire. *Immunity* 28, 112–121 (2008).

119. Owen, D. L. *et al.* Thymic regulatory T cells arise via two distinct developmental programs. *Nat Immunol* 20, 195–205 (2019).

120. Antov, A., Yang, L., Vig, M., Baltimore, D. & Parijs, L. V. Essential Role for STAT5 Signaling in CD25+CD4+ Regulatory T Cell Homeostasis and the Maintenance of Self-Tolerance. *J Immunol* 171, 3435–3441 (2003).

121. Burchill, M. A., Yang, J., Vogtenhuber, C., Blazar, B. R. & Farrar, M. A. IL-2 Receptor β-Dependent STAT5 Activation Is Required for the Development of Foxp3+ Regulatory T Cells. *J Immunol* 178, 280–290 (2007).

122. Lio, C.-W. J. & Hsieh, C.-S. A Two-Step Process for Thymic Regulatory T Cell Development. *Immunity* 28, 100–111 (2008).

123. Wagner, A. H. *et al.* DGIdb 2.0: mining clinically relevant drug–gene interactions. *Nucleic Acids Res* 44, D1036–D1044 (2016).

124. Griffith, M. *et al.* DGIdb: mining the druggable genome. *Nat Methods* 10, 1209–1210 (2013).

125. Lin, Y. *et al.* Drug target ontology to classify and integrate drug discovery data. *J Biomed Semant* 8, 50 (2017).

126. Nilius, B. & Szallasi, A. Transient Receptor Potential Channels as Drug Targets: From the Science of Basic Research to the Art of Medicine. *Pharmacol Rev* 66, 676–814 (2014).

127. Nadler, M. J. S. *et al.* LTRPC7 is a Mg·ATP-regulated divalent cation channel required for cell viability. *Nature* 411, 590–595 (2001).

128. Runnels, L. W., Yue, L. & Clapham, D. E. TRP-PLIK, a Bifunctional Protein with Kinase and Ion Channel Activities. *Science* 291, 1043–1047 (2001).

129. Monteilh-Zoller, M. K. *et al.* TRPM7 Provides an Ion Channel Mechanism for Cellular Entry of Trace Metal Ions. *J Gen Physiology* 121, 49–60 (2003).

130. Py, B. F. *et al.* Caspase-11 Controls Interleukin-1β Release through Degradation of TRPC1. *Cell Reports* 6, 1122–1128 (2014).

131. Bidère, N., Su, H. C. & Lenardo, M. J. GENETIC DISORDERS OF PROGRAMMED CELL DEATH IN THE IMMUNE SYSTEM*. *Annu Rev Immunol* 24, 321–352 (2006).

132. Manns, M. P., Lohse, A. W. & Vergani, D. Autoimmune hepatitis – Update 2015. *J Hepatol* 62, S100–S111 (2015).

133. Tiegs, G., Hentschel, J. & Wendel, A. A T cell-dependent experimental liver injury in mice inducible by concanavalin A. *J Clin Invest* 90, 196–203 (1992).

134. Sahni, J. & Scharenberg, A. M. TRPM7 Ion Channels Are Required for Sustained Phosphoinositide 3-Kinase Signaling in Lymphocytes. *Cell Metab* 8, 84–93 (2008).

135. Smith-Garvin, J. E., Koretzky, G. A. & Jordan, M. S. T Cell Activation. *Immunology* 27, 591–619 (2009).

136. Faouzi, M., Kilch, T., Horgen, F. D., Fleig, A. & Penner, R. The TRPM7 channel kinase regulates store-operated calcium entry. *J Physiology* 595, 3165–3180 (2017).

137. Heymann, F. & Tacke, F. Immunology in the liver — from homeostasis to disease. *Nat Rev Gastroentero* 13, 88–110 (2016).

138. Churlaud, G. *et al.* Human and Mouse CD8+CD25+FOXP3+ Regulatory T Cells at Steady State and during Interleukin-2 Therapy. *Front Immunol* 6, 171 (2015).

139. Vignali, D. A. A., Collison, L. W. & Workman, C. J. How regulatory T cells work. *Nat Rev Immunol* 8, 523–532 (2008).

140. Sakaguchi, S., Vignali, D. A. A., Rudensky, A. Y., Niec, R. E. & Waldmann, H. The plasticity and stability of regulatory T cells. *Nat Rev Immunol* 13, 461–467 (2013).

141. Sawant, D. V. & Vignali, D. A. A. Once a Treg, always a Treg? *Immunol Rev* 259, 173–191 (2014).

142. Weiss, J. M. *et al.* Neuropilin 1 is expressed on thymus-derived natural regulatory T cells, but not mucosa-generated induced Foxp3+ T reg cells. *J Exp Med* 209, 1723–1742 (2012).

143. Yadav, M. *et al.* Neuropilin-1 distinguishes natural and inducible regulatory T cells among regulatory T cell subsets in vivo. *J Exp Med* 209, 1713–1722 (2012).

144. Brinkmann, V. *et al.* Fingolimod (FTY720): discovery and development of an oral drug to treat multiple sclerosis. *Nat Rev Drug Discov* 9, 883–897 (2010).

145. Qin, X. *et al.* Sphingosine and FTY720 are potent inhibitors of the transient receptor potential melastatin 7 (TRPM7) channels. *Brit J Pharmacol* 168, 1294–1312 (2013).

146. Kanai, T. *et al.* Identification of STAT5A and STAT5B Target Genes in Human T Cells. *Plos One* 9, e86790 (2014).

147. Liu, Z. *et al.* Immune homeostasis enforced by co-localized effector and regulatory T cells. *Nature* 528, 225–230 (2015).

148. Oh-hora, M. *et al.* Dual functions for the endoplasmic reticulum calcium sensors STIM1 and STIM2 in T cell activation and tolerance. *Nat Immunol* 9, 432–443 (2008).

149. Germain, R. N. Maintaining system homeostasis: the third law of Newtonian immunology. *Nat Immunol* 13, 902–906 (2012).

150. Kozak, J. A. & Cahalan, M. D. MIC Channels Are Inhibited by Internal Divalent Cations but Not ATP. *Biophys J* 84, 922–927 (2003).

151. Runnels, L. W., Yue, L. & Clapham, D. E. The TRPM7 channel is inactivated by PIP(2) hydrolysis. *Nat Cell Biol* 4, 329–36 (2002).

152. Jiang, J., Li, M. & Yue, L. Potentiation of TRPM7 Inward Currents by Protons. *J Gen Physiology* 126, 137–150 (2005).

153. Krapivinsky, G., Krapivinsky, L., Manasian, Y. & Clapham, D. E. The TRPM7 Chanzyme Is Cleaved to Release a Chromatin-Modifying Kinase. *Cell* 157, 1061–1072 (2014).

154. Muls, N., Dang, H. A., Sindic, C. J. M. & Pesch, V. van. Fingolimod Increases CD39-Expressing Regulatory T Cells in Multiple Sclerosis Patients. *Plos One* 9, e113025 (2014).

155. Schmittgen, T. D. & Livak, K. J. Analyzing real-time PCR data by the comparative CT method. *Nat Protoc* 3, 1101–1108 (2008).

156. Zhou, Y. *et al.* Membrane potential modulates plasma membrane phospholipid dynamics and K-Ras signaling. *Science* 349, 873–876 (2015).

157. Garcia-Rubio, R., Oliveira, H. C. de, Rivera, J. & Trevijano-Contador, N. The Fungal Cell Wall: Candida, Cryptococcus, and Aspergillus Species. *Front Microbiol* 10, 2993 (2020).

158. Brown, G. D. Dectin-1: a signalling non-TLR pattern-recognition receptor. *Nat Rev Immunol* 6, 33–43 (2006).

159. Pappas, P. G., Lionakis, M. S., Arendrup, M. C., Ostrosky-Zeichner, L. & Kullberg, B. J. Invasive candidiasis. *Nat Rev Dis Primers* 4, 18026 (2018).

160. Huang, J.-H. *et al.* CR3 and Dectin-1 Collaborate in Macrophage Cytokine Response through Association on Lipid Rafts and Activation of Syk-JNK-AP-1 Pathway. *Plos Pathog* 11, e1004985 (2015).

161. Halder, L. D. *et al.* Immune modulation by complement receptor 3-dependent human monocyte TGF-β1-transporting vesicles. *Nat Commun* 11, 2331 (2020).

162. Stafford, S. L. *et al.* Metal ions in macrophage antimicrobial pathways: emerging roles for zinc and copper. *Bioscience Rep* 33, e00049 (2013).

163. Botella, H. *et al.* Mycobacterial P1-Type ATPases Mediate Resistance to Zinc Poisoning in Human Macrophages. *Cell Host Microbe* 10, 248–259 (2011).

164. Singh, K. P. *et al.* Effect of Zinc on Immune Functions and Host Resistance Against Infection and Tumor Challenge. *Immunopharm Immunot* 14, 813–840 (2008).

165. Abiria, S. A. *et al.* TRPM7 senses oxidative stress to release Zn2+ from unique intracellular vesicles. *Proc National Acad Sci* 114, E6079–E6088 (2017).

166. Jaumouillé, V. & Waterman, C. M. Physical Constraints and Forces Involved in Phagocytosis. *Front Immunol* 11, 1097 (2020).

167. Starostina, I. *et al.* Distinct calcium regulation of TRPM7 mechanosensitive channels at plasma membrane microdomains visualized by FRET-based single cell imaging. *Sci Rep-uk* 11, 17893 (2021).

168. Liu, Y.-S. *et al.* Mechanosensitive TRPM7 mediates shear stress and modulates osteogenic differentiation of mesenchymal stromal cells through Osterix pathway. *Sci Rep-uk* 5, 16522 (2015).

169. Yankaskas, C. L. *et al.* The fluid shear stress sensor TRPM7 regulates tumor cell intravasation. *Sci Adv* 7, eabh3457 (2021).

170. Freeman, S. A. *et al.* Integrins Form an Expanding Diffusional Barrier that Coordinates Phagocytosis. *Cell* 164, 128–140 (2016).

171. Jaumouillé, V., Cartagena-Rivera, A. X. & Waterman, C. M. Coupling of β2 integrins to actin by a mechanosensitive molecular clutch drives complement receptor-mediated phagocytosis. *Nat Cell Biol* 21, 1357–1369 (2019).

172. Ryazanova, L. V. *et al.* TRPM7 is essential for Mg2+ homeostasis in mammals. *Nat Commun* 1, 109 (2010).

173. Lee, W. & Lee, G. R. Transcriptional regulation and development of regulatory T cells. *Exp Mol Medicine* 50, e456 (2018).

174. Vaeth, M. *et al.* Store-Operated Ca2+ Entry in Follicular T Cells Controls Humoral Immune Responses and Autoimmunity. *Immunity* 44, 1350–1364 (2016).

175. Vaeth, M. *et al.* Store-Operated Ca2+ Entry Controls Clonal Expansion of T Cells through Metabolic Reprogramming. *Immunity* 47, 664-679.e6 (2017).

176. Kappos, L. *et al.* Oral Fingolimod (FTY720) for Relapsing Multiple Sclerosis. *New Engl J Medicine* 355, 1124–1140 (2006).

177. Kappos, L. *et al.* A Placebo-Controlled Trial of Oral Fingolimod in Relapsing Multiple Sclerosis. *New Engl J Medicine* 362, 387–401 (2010).

178. Cohen, J. A. *et al.* Oral Fingolimod or Intramuscular Interferon for Relapsing Multiple Sclerosis. *New Engl J Medicine* 362, 402–415 (2010).

179. Kartalou, G.-I. *et al.* Anti-Inflammatory Treatment with FTY720 Starting after Onset of Symptoms Reverses Synaptic Deficits in an AD Mouse Model. *Int J Mol Sci* 21, 8957 (2020).

180. Jęśko, H., Wencel, P. L., Lukiw, W. J. & Strosznajder, R. P. Modulatory Effects of Fingolimod (FTY720) on the Expression of Sphingolipid Metabolism-Related Genes in an Animal Model of Alzheimer's Disease. *Mol Neurobiol* 56, 174–185 (2019).

181. Brinkmann, V. *et al.* The Immune Modulator FTY720 Targets Sphingosine 1-Phosphate Receptors*. *J Biol Chem* 277, 21453–21457 (2002).

182. Pulli, I., Asghar, M. Y., Kemppainen, K. & Törnquist, K. Sphingolipid-mediated calcium signaling and its pathological effects. *Biochimica Et Biophysica Acta Bba - Mol Cell Res* 1865, 1668–1677 (2018).

183. Dupré, L., Boztug, K. & Pfajfer, L. Actin Dynamics at the T Cell Synapse as Revealed by Immune-Related Actinopathies. *Frontiers Cell Dev Biology* 9, 665519 (2021).

184. Poh, C. M. *et al.* Multiplex Screening Assay for Identifying Cytotoxic CD8+ T Cell Epitopes. *Front Immunol* 11, 400 (2020).

185. Kumar, M., Keller, B., Makalou, N. & Sutton, R. E. Systematic Determination of the Packaging Limit of Lentiviral Vectors. *Hum Gene Ther* 12, 1893–1905 (2001).